

C  
Internal Report  
DESY F35D-96-17  
November 1996



\*X1996-01796\*

# Measurement of the Proton Structure Function $F_2$ Using the Hadron Electron Separator of the ZEUS Detector at HERA

by

K. Ohrenberg

Eigentum der Property of	<b>DESY</b>	Bibliothek library
Zugang- Accession	18. DEZ. 1996	
Leih- Loan period:	7	days

**DESY behält sich alle Rechte für den Fall der Schutzrechtserteilung und für die wirtschaftliche Verwertung der in diesem Bericht enthaltenen Informationen vor.**

**DESY reserves all rights for commercial use of information included in this report, especially in case of filing application for or grant of patents.**

**"Die Verantwortung für den Inhalt dieses  
Internen Berichtes liegt ausschließlich beim Verfasser"**

Measurement of the Proton Structure Function  $F_2$   
using the Hadron Electron Separator  
of the ZEUS Detector at HERA

Dissertation

zur Erlangung des Doktorgrades  
des Fachbereichs Physik  
der Universität Hamburg

vorgelegt von

Kars $\overline{\text{O}}$ hrenberg  
aus Stade

Hamburg  
1996



Measurement of the Proton Structure Function  $F_2$   
using the Hadron Electron Separator  
of the ZEUS Detector at HERA

Dissertation

zur Erlangung des Doktorgrades  
des Fachbereichs Physik  
der Universität Hamburg

vorgelegt von

Kars Ohrenberg  
aus Stade

Hamburg  
1996

Gutachter der Dissertation: Prof. Dr. E. Lohrmann  
Prof. Dr. V. Blobel

Gutachter der Disputation: Prof. Dr. E. Lohrmann  
Prof. Dr. G. Heinzelmann

Datum der Disputation: 20. November 1996

Sprecher des  
Fachbereichs Physik  
und Vorsitzender des  
Promotionsausschusses: Prof. Dr. B. Kramer

# Contents

## Abstract

The proton structure function  $F_2$  has been extracted from data taken by the ZEUS experiment in the year 1994. The usable integrated luminosity for this analysis was  $1.54 \text{ pb}^{-1}$  and the analysis covered the kinematic range of  $4 \cdot 10^{-4} < x < 7 \cdot 10^{-2}$  and  $2.5 < Q^2 < 450 \text{ GeV}^2$ . The Hadron Electron Separator (HES) of the ZEUS experiment has been used to improve the identification of the scattered electrons at low energies. By combining the ZEUS neural network electron finder SINISTRA and the HES it was possible to extend the measurement of the structure function  $F_2$  down to electron scattering energies of 6 GeV. The results of this analysis are compared to the 1994 measurements of ZEUS and H1.

## Zusammenfassung

Die Proton-Strukturfunktion  $F_2$  wurde aus den mit dem ZEUS Experiment im Jahre 1994 aufgezeichneten Daten bestimmt. Die nutzbare integrierte Luminosität für diese Arbeit betrug  $1.54 \text{ pb}^{-1}$  und die Analyse überdeckte den kinematischen Bereich von  $4 \cdot 10^{-4} < x < 7 \cdot 10^{-2}$  und  $2.5 < Q^2 < 450 \text{ GeV}^2$ . Der Hadronen Elektronen Separator (HES) des ZEUS Experiments wurde verwendet, um die Identifikation gestreuter, niederenergetischer Elektronen zu verbessern. Durch eine Kombination des von der ZEUS Kollaboration verwendeten, auf einem neuronalen Netz basierenden Elektronenfinders SINISTRA und des HES war es möglich, die Messung der Strukturfunktion  $F_2$  bis herunter zu Elektronenenergien von 6 GeV zu erweitern. Die Resultate dieser Analyse werden mit den im Jahre 1994 durchgeführten Messungen von ZEUS und H1 verglichen.

<b>Introduction</b>	<b>1</b>
<b>1 Deep Inelastic Scattering</b>	<b>3</b>
1.1 Elastic Electron Nucleon Scattering, Form Factors	3
1.2 Inelastic Electron Proton Scattering, Structure Functions	6
1.3 Quark Parton Model	9
1.4 QCD Evolution Equations	13
1.5 Parton Distributions	20
1.5.1 Fixed Target DIS Experiments	20
1.5.2 Parameterizations of Parton Densities	21
<b>2 HERA</b>	<b>27</b>
2.1 The Electron-Proton Collider HERA	27
2.2 HERA Operation in the Year 1994	29
<b>3 The ZEUS Detector</b>	<b>33</b>
3.1 ZEUS Components	33
3.1.1 The Tracking System	34
3.1.2 The Uranium Calorimeter	36
3.1.3 The Hadron Electron Separator (HES)	38
3.1.4 The Luminosity Monitor (LUMI)	39
3.1.5 The Small Angle Rear Tracking Detector (SRTD)	39
3.2 Data Acquisition System Overview	39
3.2.1 The Trigger System	40
3.2.2 The ZEUS Expert System (ZEX)	43
<b>4 Electron Identification</b>	<b>49</b>
4.1 Electron Finder	49
4.2 Electron Reconstruction with the HES	52
4.2.1 Object Characteristics	52
4.2.2 Position Reconstruction	54
4.2.3 Electron Identification with the HES	58
4.3 Electron Finder Efficiencies	63
4.4 Combining SINISTRA and HES	71

<b>5 Determination of the Proton Structure Function <math>F_2</math></b>	<b>73</b>
5.1 MC Validation	73
5.2 Kinematic Reconstruction	77
5.2.1 Electron-Only Method	78
5.2.2 Hadron-Only Method	78
5.2.3 Double-Angle Method	79
5.2.4 $\Sigma$ -Method	79
5.2.5 $P_T$ -Method	82
5.3 Event Selection	82
5.3.1 Trigger Selection	82
5.3.2 Offline Selection Cuts	85
5.4 Unfolding	86
5.4.1 Migrations and Binning	86
5.4.2 Background Subtraction	89
5.4.3 Unfolding Procedure	92
5.5 Determination of the Structure Function $F_2$	93
5.6 Systematic Checks	96
5.7 Final Results	98
<b>Conclusion</b>	<b>103</b>
<b>Acknowledgment</b>	<b>104</b>
<b>A Tables</b>	<b>105</b>
<b>Bibliography</b>	<b>109</b>

## List of Figures

1.1 Lowest order elastic electron nucleon scattering	4
1.2 Evidence for a non-point-like proton	5
1.3 Magnetic and electric proton form factors	6
1.4 Diagram for lowest order deep inelastic $ep$ scattering	7
1.5 Invariant mass distribution	8
1.6 Evidence for point-like nucleon constituents	10
1.7 Observation of scaling	11
1.8 Callan-Gross relation	12
1.9 Lowest order gluon contributions to the $ep$ scattering process	14
1.10 Deviations from scaling	15
1.11 Production of a low- $x$ quark via a parton ladder	17
1.12 Ladder diagrams representing the LL and DLL approximation	18
1.13 Ladder diagram representing the BFKL resummation	19
1.14 Different QCD evolutions in the $x$ - $Q^2$ -plane	21
1.15 Parton distributions for the MRSA parameterization	22
1.16 Coverage of the kinematic range by fixed target and HERA experiments	24
2.1 Bird eye's view of the DESY area	27
2.2 The HERA injection scheme	28
2.3 Bunch distribution used by HERA in the year 1994	29
2.4 Integrated luminosity delivered by HERA in the year 1994	30
3.1 Cross section and longitudinal cut of the ZEUS detector	34
3.2 Cross section of a CTD octant	35
3.3 Calorimeter sections and their division into EMC and HAC cells	36
3.4 View of the largest FCAL module	37
3.5 Cross section of a FCAL tower	37
3.6 Coverage of the RCAL by the Hadron Electron Separator	38
3.7 ZEUS luminosity monitor	40
3.8 Layout of the ZEUS trigger and data acquisition system	42
3.9 Architecture of the ZEUS Expert System	44
3.10 Blackboard architecture scheme	45
4.1 Creation of calorimeter objects via different clustering algorithms	49
4.2 Efficiency and purity for different calorimeter based electron finders	50
4.3 $E - P_z$ distribution of events with an identified electron by different electron finders	51
4.4 Energy ratio of different HES cluster sizes	53
4.5 Energy deposit in the HES versus the energy measured by the calorimeter	54

4.6	Average number of diode hits as a function of the energy deposit in the RCAL and the energy deposit in the HES . . . . .	55
4.7	Distribution of the energy ratios $R_x$ and $R_y$ in the ZEUS experiment . . . . .	55
4.8	Fit to the distribution of the unfolded energy ratio $R$ . . . . .	56
4.9	Distribution of the difference in the reconstructed position between HES and CAL and HES and SRTD . . . . .	57
4.10	Comparison of the position of hadrons and electrons as measured by HES and CAL in MC and data . . . . .	59
4.11	Distribution of the ratio $\sum E_i r_i^2 / \langle r_i^2 \rangle$ for electron candidates in DIS and Photo-production Monte Carlo simulations . . . . .	60
4.12	Efficiency and purity for the electron finder based on the HES information . . . . .	61
4.13	Efficiencies derived from a DIS MC simulation . . . . .	62
4.14	Efficiencies derived from DIS MC and DIS data with the assumption of two independent finders . . . . .	63
4.15	Efficiencies derived from DIS MC and DIS data with different cuts on $\delta$ . . . . .	64
4.16	Efficiencies derived from a DIS MC with additional photoproduction events and DIS data . . . . .	65
4.17	Misidentification probability $\eta$ for different electron finders . . . . .	66
4.18	Number of hadrons in the DIS MC sample with additional photoproduction events . . . . .	67
4.19	Efficiencies derived from DIS MC with additional photoproduction events after the correction on the hadronic background . . . . .	68
4.20	Number of hadrons in the DIS data . . . . .	69
4.21	Efficiencies derived from DIS MC and DIS data after the correction on the hadronic background . . . . .	70
4.22	Efficiency and purity for SINISTRA, HES and a combined finder of SINISTRA and HES . . . . .	71
5.1	Vertex distribution in DIS data and the DIS MC simulation . . . . .	74
5.2	Distributions of the primary variables $E_e'$ , $\Theta_e$ , $F_h$ and $\gamma_h$ . . . . .	75
5.3	Corrected energy distribution of the scattered electron . . . . .	77
5.4	An event with a rapidity gap as seen in the ZEUS detector . . . . .	78
5.5	$\eta_{max}$ distribution of DIS events . . . . .	79
5.6	Isolines for the primary measured variables . . . . .	80
5.7	Reconstructed kinematic variables versus their generated value . . . . .	81
5.8	A DIS event as seen in the ZEUS detector . . . . .	83
5.9	Efficiency of the DIS trigger . . . . .	85
5.10	Distribution of the primary variables $E_e'$ , $\Theta_e$ and the kinematic variables $Q_{el}^2$ and $y_{el}$ in the final data sample . . . . .	87
5.11	Migration effects due to the detector resolution as seen in the MC . . . . .	88
5.12	Resolution of the reconstructed kinematic variables $Q_{el}^2$ and $y_{el}$ . . . . .	89
5.13	Binning used in this analysis . . . . .	90
5.14	Fits to the $\delta$ -distribution in a certain bin . . . . .	91
5.15	$\chi_{bin}^2$ for each bin in the $y$ and $Q^2$ range as a function of the number of iteration . . . . .	94
5.16	Systematic errors on the extraction of $F_2$ . . . . .	97
5.17	$F_2$ versus $x$ for fixed $Q^2$ as obtained by this analysis in the low $Q^2$ -bins . . . . .	99
5.18	$F_2$ versus $x$ for fixed $Q^2$ as obtained by this analysis in the medium $Q^2$ -bins . . . . .	100
5.19	$F_2$ versus $x$ for fixed $Q^2$ as obtained by this analysis in the high $Q^2$ -bins . . . . .	101

## List of Tables

1.1	Summary of fixed target experiments . . . . .	23
2.1	Design values of the HERA accelerator . . . . .	28
3.1	Selected parameters of some ZEUS components . . . . .	41
4.1	Functions used for the energy ratios $R_x$ and $R_y$ . . . . .	58
4.2	$\sigma$ of a Gaussian fit to the measured position difference between HES, CAL and SRTD . . . . .	58
4.3	Width ( $\sigma$ ) of the position resolution for HES, CAL and SRTD . . . . .	58
5.1	Number of events rejected and retained by the selection cuts . . . . .	86
5.2	Quantities used in the unfolding procedure . . . . .	92
A.1	$F_2$ in $(y, Q^2)$ bins unfolded by an iterative method (part 1) . . . . .	105
A.2	$F_2$ in $(y, Q^2)$ bins unfolded by an iterative method (part 2) . . . . .	106
A.3	$F_2$ in $(y, Q^2)$ bins unfolded by an iterative method (part 3) . . . . .	107
A.4	$F_2$ in $(y, Q^2)$ bins unfolded by an iterative method (part 4) . . . . .	108

# Introduction

The HERA accelerator taken into operation in the year 1992 at the Deutsches Elektronen-Synchrotron in Hamburg is a unique facility to explore the substructure of the proton. By colliding electrons of 27.5 GeV and protons of 820 GeV beam energy, a center of mass energy of about 300 GeV is reached and the spatial resolution which is given by the momentum transfer is by three orders of magnitude smaller than the proton radius. Thus the proton structure can be explored in a region which has not been covered by fixed target experiments and where the proton constituents only carry a very small amount ( $x \sim 10^{-4}$ ) of the proton's momentum. This kinematic region of low  $x$  is of great theoretical interest since the number of partons increases rapidly as  $x$  decreases and thus the partons can no longer be treated as non-interacting. New physical phenomena are expected to occur and recombination and shadowing effects may have to be taken into account.

In the interesting region of low  $x$  resp. high  $y$  which corresponds to low energies of the scattered electron, the contribution from photoproduction background events to the deep inelastic scattering events rises and thus it gets difficult to separate the scattered, low energetic electron from pions originating from photoproduction events. This can be improved by the Hadron Electron Separator (HES) of the ZEUS experiment which is an array of silicon diodes of  $3 \times 3.3 \text{ cm}^2$  located at a depth of 3.3 radiation units within the rear calorimeter. Since the shower profile differs significantly for electrons and hadrons, the amount of signal seen by the HES offers a possibility to separate between these particles and allows to extend the identification of the scattered electron towards lower electron energies.

This thesis presents a measurement of the proton structure function  $F_2$  obtained from the data taken by the HERA experiment ZEUS in the year 1994. The kinematic range covered by this analysis is  $4 \cdot 10^{-4} < x < 7 \cdot 10^{-2}$  and  $2.5 < Q^2 < 450 \text{ GeV}^2$ .

The thesis starts with a short review of the history of lepton nucleon scattering where an overview of early electron proton scattering experiments is found in [Tay91, Ken91, Fri91]. Chapter 1 finishes with an overview of the QCD improved parton model and recent parton parameterizations. The experimental facilities HERA and ZEUS are described in chapter 2 and chapter 3 where the description of the ZEUS detector components focuses on those used in this analysis. Chapter 4 presents results on the identification of electrons with the Hadron Electron Separator, electron finder efficiencies and an improvement on the electron identification at low scattering energies. Chapter 5 finally describes the structure function analysis and presents the final results on the proton structure function  $F_2$ .

## Chapter 1

# Deep Inelastic Scattering

Probing the structure of unknown objects with high energy particles has a very long tradition which started with the experiment of Geiger and Marsden [GM09] in 1909 who scattered  $\alpha$ -particles upon a metal plate. They observed that a small fraction of these particles was deflected by a large angle. This observation was interpreted in 1911 by Lord E. Rutherford as a substructure of the atom [Rut11]. With the advent of high energy particle accelerators that exercise has been repeated on the nucleons.

### 1.1 Elastic Electron Nucleon Scattering, Form Factors

To resolve the structure of an unknown probe particles are scattered on this object and the angular distribution of the deflected particles is measured and compared with the assumption of a point-like probe. The angular distribution for a non-relativistic, spin-less projectile of unit charge scattering elastically on a spin-less and point-like, fixed unit charge is given by the Rutherford formula

$$\frac{d\sigma}{d\Omega} = \frac{\alpha^2}{4(\beta p)^2} \frac{1}{\sin^4(\Theta/2)} \quad (1.1)$$

where  $p$  is the momentum of the incident particle and  $\Theta$  its scattering angle. If the charge distribution of the unknown object is not point-like, a form factor  $F(q)$  describing the unknown structure is introduced and equation 1.1 changes to

$$\frac{d\sigma}{d\Omega} = \frac{\alpha^2}{4(\beta p)^2} \frac{1}{\sin^4(\Theta/2)} |F(q)|^2 \quad (1.2)$$

where  $q$  is the momentum transfer between the incident particle and the target. For a static and spin-less charge distribution  $\rho(\vec{r})$  with the normalization  $\int_0^\infty \rho(\vec{r}) d^3r = 1$  the form factor  $F(q)$  is just the Fourier transform of the spatial charge distribution  $\rho(\vec{r})$

$$F(q) = \int_0^\infty \rho(\vec{r}) e^{i\vec{q}\vec{r}} d^3r \quad (1.3)$$

If  $|q|$  is not too large,  $F(q)$  can be expanded to

$$F(q) = 1 - \frac{1}{6} |q|^2 \langle r^2 \rangle + \dots \quad (1.4)$$

where  $\langle r^2 \rangle$  reflects the mean square radius of the charge cloud.

For electrons as projectile particles, their spin has to be taken into account and the first calculation of scattering a relativistic electron with spin  $\frac{1}{2}$  on a spin-less and point-like charge was done by Mott in 1929 and led to the following differential cross section [Mot29]:

$$\left(\frac{d\sigma}{d\Omega}\right)_{\text{Mott}} = \frac{\alpha^2}{4E^2} \frac{1}{\sin^4(\Theta/2)} \frac{\cos^2(\Theta/2)}{[1 + 2E/M \sin^2(\Theta/2)]} \quad (1.5)$$

where  $E$  is the electrons energy,  $M$  the targets mass and the different terms arise from Rutherford scattering, the electron spin and the target recoil. For non-point-like charge distributions equation 1.5 is again expanded by a form factor where in this relativistic case  $q^2$  is given as the square of the difference between the 4-momenta of the incident ( $k$ ) and emerging ( $k'$ ) electron  $q^2 = (k - k')^2$ .

Scattering electrons on nucleons is even more complicated, since not only the charge distribution of the nucleon but also its spin and magnetic moment have to be taken into account and a second form factor has to be introduced.

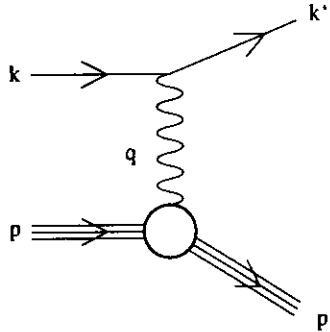


Figure 1.1: Lowest order elastic electron nucleon scattering by the exchange of a single virtual photon.

The lowest order scattering amplitude for elastic electron nucleon scattering as shown in figure 1.1 is given by

$$T_f = -i \int j_\mu \left(-\frac{1}{q^2}\right) J^\mu d^4x \quad (1.6)$$

where  $q = k - k' = p' - p$  and the electron and nucleon currents are expressed by

$$j^\mu = -e\bar{u}(k')\gamma^\mu u(k)e^{i(k'-k)x} \quad (1.7)$$

$$J^\mu = -e\bar{u}(p')[\ ]u(p)e^{i(p'-p)x}. \quad (1.8)$$

Since the nucleon is an extended structure, the square brackets in equation 1.8 can not just be replaced by  $\gamma^\mu$  as in equation 1.7 for a point-like spin  $\frac{1}{2}$  particle. The most general form allowed by the square brackets is

$$[\ ] = \left[ F_1(q^2)\gamma^\mu + \frac{\kappa}{2M}F_2(q^2)i\sigma^{\mu\nu}q_\nu \right] \quad (1.9)$$

where  $\kappa$  is the anomalous magnetic moment of the nucleon. The calculation of this cross section was in first Born approximation, that is to leading order in  $\alpha$ , done by Rosenbluth in 1950 [Ros50] and led to the so called Rosenbluth formula for elastic electron nucleon scattering in the fixed target frame

$$\frac{d\sigma}{d\Omega} = \left(\frac{d\sigma}{d\Omega}\right)_{\text{Mott}} \left[ \frac{G_E^2(q^2) + \tau G_M^2(q^2)}{1 + \tau} + 2\tau G_M^2(q^2) \tan^2(\Theta/2) \right] \quad (1.10)$$

with  $\tau = -q^2/(4M^2)$  and where for practical use the definitions  $G_E = F_1 + \frac{\kappa q^2}{4M^2}F_2$  and  $G_M = F_1 + \kappa F_2$  have been introduced. These factors can be regarded as generalizations of the non-relativistic form factors introduced in equation 1.3 and are called magnetic ( $G_M$ ) and electric form factors ( $G_E$ ) since they are closely related to the magnetic moment and charge distribution of the nucleon. The electric and magnetic form factors are normalized to the total charge and total magnetic moment of the nucleons ( $G_E^p(0) = 1$ ,  $G_E^n(0) = 0$ ,  $G_M^p(0) = 2.79$  and  $G_M^n(0) = -1.91$ ).

Elastic electron proton scattering experiments have been carried out by Hofstadter et al. in 1953 [HFM53] at the High Energy Physics Laboratory (HEPL) in Stanford and showed a first evidence for a non-point-like proton [HM55] (figure 1.2).

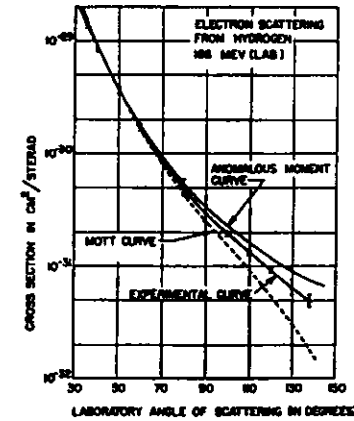


Figure 1.2: The figure shows the experimental curve, the Mott curve and the point-magnetic moment curve for an early electron proton scattering experiment. The data falls between the curves, showing that magnetic scattering occurs but also indicating that the scattering is less than expected from a point-like proton. (From [HM55])

The measurements have been continued with different incident electron energies [CH56] and in various laboratories and allowed a determination of the size and shape of the charge and magnetic moment distributions inside the proton. Result of these experiments for the magnetic and electric proton form factors are shown in figure 1.3.

For low momentum transfer  $|q|$  the form factors can be approximated by the simple scaling law

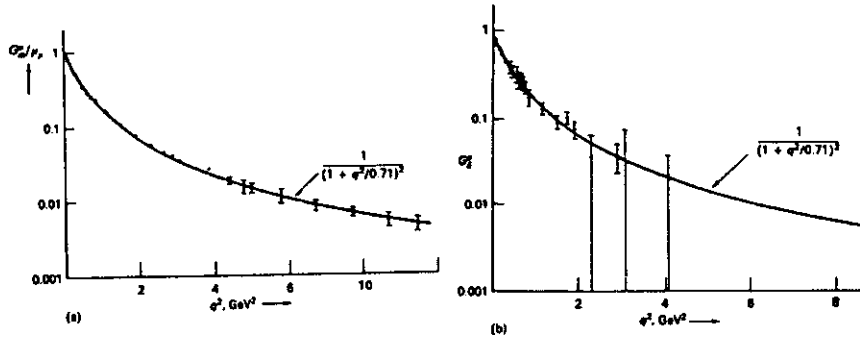


Figure 1.3: The magnetic (left) and electric (right) form factors of the proton<sup>2</sup>. The form factors are consistent with the scaling law 1.11 and follow the dipole formula 1.12. (From [Per87])

$$G_E^p(q^2) \cong \frac{G_M^p(q^2)}{|\mu_p|} \cong \frac{G_M^n(q^2)}{|\mu_n|} \cong G(q^2) \quad G_E^n(q^2) = 0 \quad (1.11)$$

and the empirical dipole formula

$$G(q^2) \approx G(0) \cdot \frac{1}{\left(1 + \frac{q^2}{0.71 \text{ GeV}^2}\right)^2}. \quad (1.12)$$

The mean square proton radius thus can be calculated according to equation 1.4 and leads to about 0.8 fm for the charge and magnetic moment distributions.

## 1.2 Inelastic Electron Proton Scattering, Structure Functions

Knowing about the extended structure of the proton, the momentum transfer  $|q|$  was increased in order to give a better spatial resolution and a more precise view of the proton structure. At high momentum transfers, the elastic form factors are very small and inelastic scattering is much more probable.

Two classes of electron proton deep inelastic scattering (DIS) events are distinguished depending on the exchanged particle. Neutral current (NC) DIS events are characterized by the exchange of a virtual photon or  $Z^0$ , whereas charged current (CC) DIS events are characterized by a neutrino in the final state and a charged boson  $W^\pm$  exchange.

The process of inelastic scattering as shown in figure 1.4 is described by the variables

$$s = (k + p)^2 \quad (1.13)$$

giving the square of the center of mass energy and

<sup>2</sup>In early publications the momentum transfer  $q$  was defined in a way that  $q^2 > 0$ . Thus the lowercase  $q^2$  seen in figure 1.3, 1.6 and 1.7 has to be regarded as the uppercase  $Q^2$  defined in equation 1.14.

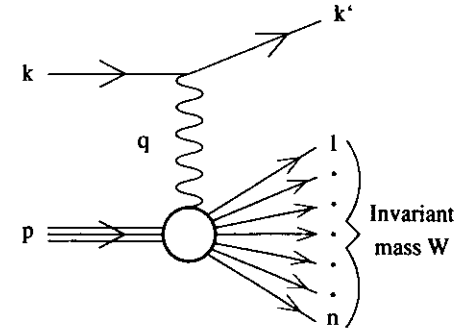


Figure 1.4: Diagram for the lowest order deep inelastic scattering process  $ep \rightarrow eX$ .

$$Q^2 = -q^2 = -(k - k')^2 \quad (1.14)$$

giving the negative four momentum transfer squared and

$$\nu = \frac{p \cdot q}{M} \quad (1.15)$$

giving the energy transfer to the hadronic system in the proton's rest frame and

$$x = \frac{Q^2}{2p \cdot q} = \frac{Q^2}{2M\nu} \quad (1.16)$$

giving the Bjorken- $x$  and

$$y = \frac{p \cdot q}{p \cdot k} \quad (1.17)$$

giving the fraction of the energy lost by the electron in the proton's rest frame. The relation between  $Q^2$ ,  $x$ ,  $y$  and  $s$  is expressed by

$$Q^2 = sxy. \quad (1.18)$$

In inelastic scattering processes, energy is transferred to the hadronic system and the invariant mass  $W$  of the hadronic final state is given by

$$W^2 = (p + q)^2 = M^2 + 2M\nu - Q^2. \quad (1.19)$$

Its distribution is shown in figure 1.5 for a historic measurement at DESY [B 68] and shows the elastic peak where the proton does not break up and broader peaks where the target is excited to resonant baryon states. Beyond the resonances the complicated multi-particle states with a large invariant mass result in a smooth distribution.

To describe inelastic scattering and obtain similar expressions for the cross section as in equation 1.10 the concept of single virtual photon exchange has to be extended to those processes [DW64]. The replacement of the square brackets in equation 1.8 by expression 1.9 is inadequate to describe inelastic events since the final proton state is not a single fermion. The cross section  $d\sigma \sim L_{\mu\nu}^e(L^p)^{\mu\nu}$  has to be generalized to  $d\sigma \sim L_{\mu\nu}^e W^{\mu\nu}$  where the lepton tensor remains unchanged since the upper part of figure 1.4 is not changed compared to figure 1.1. The tensor

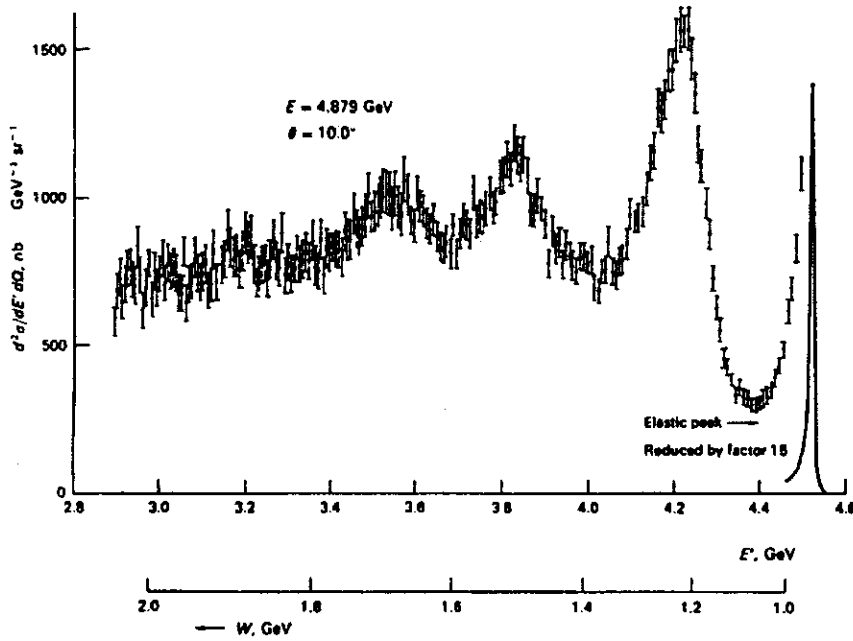


Figure 1.5: Invariant mass distribution as seen in an historic measurement at DESY [B 68]. Further explanations are given in the text.

$L_{\mu\nu}^e$  at the lepton vertex is described by quantum electrodynamics (QED) and after summing and averaging over the spins given by

$$L_{\mu\nu}^e = 2 \cdot [k'_\mu k'_\nu + k'_\nu k'_\mu - (k'k - m_e^2) \cdot g_{\mu\nu}] \quad (1.20)$$

The form for the hadronic tensor  $W^{\mu\nu}$  is (neglecting a parity violating term and imposing current conservation at the hadron vertex) given by

$$W^{\mu\nu} = W_1 \cdot \left( -g^{\mu\nu} + \frac{q^\mu q^\nu}{q^2} \right) + \frac{W_2}{M^2} \cdot \left( p^\mu - \frac{p \cdot q}{q^2} q^\mu \right) \left( p^\nu - \frac{p \cdot q}{q^2} q^\nu \right). \quad (1.21)$$

$W_1$  and  $W_2$  are functions of the Lorentz scalar variables that can be constructed from the four-momenta at the hadronic vertex. Unlike elastic scattering there are two independent variables which can be chosen as  $Q^2$  and  $\nu$ . The double differential cross section in the laboratory frame is then given by

$$\frac{d^2\sigma}{dE'd\Omega} = \frac{\alpha^2 \cos^2(\Theta/2)}{4E^2 \sin^4(\Theta/2)} [W_2(Q^2, \nu) + 2W_1(Q^2, \nu) \tan^2(\Theta/2)] \quad (1.22)$$

which is the analog of the Rosenbluth cross section in equation 1.10. The structure functions  $W_1$  and  $W_2$  contain all the information about the structure of the target obtained by scattering

unpolarized electrons off unpolarized protons.

Within the single-photon-exchange approximation one may view inelastic scattering as photoproduction by virtual photons. Here, as opposed to photoproduction by real photons, the photon mass  $q^2$  is variable and the exchanged photon can have a longitudinal as well as a transverse polarization. Thus the total cross section for absorption of transverse ( $\sigma_T$ ) and longitudinal polarized virtual photons ( $\sigma_L$ ) is related to the differential cross section for inelastic electron scattering (1.22) according to [Han63]

$$\frac{d^2\sigma}{dE'd\Omega} = \Gamma (\sigma_T(Q^2, \nu) + \epsilon \sigma_L(Q^2, \nu)) \quad (1.23)$$

where

$$\Gamma = \frac{\alpha}{2\pi^2} \frac{K E'}{Q^2 E} \left( \frac{1}{1-\epsilon} \right) \quad (1.24)$$

is the flux of the virtual photons,

$$\epsilon = \left[ 1 + 2 \left( \frac{Q^2 + \nu^2}{Q^2} \right) \tan^2(\Theta/2) \right]^{-1} \quad (1.25)$$

is the degree of longitudinal polarization and  $K = (W^2 - M^2)/(2M)$ . Thus the cross sections  $\sigma_L$  and  $\sigma_T$  are related to the structure functions  $W_1$  and  $W_2$  by

$$\sigma_T = \frac{4\pi\alpha^2}{K} W_1(Q^2, \nu) \quad (1.26)$$

$$\sigma_L = \frac{4\pi^2\alpha}{K} \left[ \left( 1 + \frac{\nu^2}{Q^2} \right) W_2(Q^2, \nu) - W_1(Q^2, \nu) \right] \quad (1.27)$$

In the limit  $Q^2 \rightarrow 0$  gauge invariance requires that  $\sigma_L \rightarrow 0$  and  $\sigma_T \rightarrow \sigma_{\text{tot}}^{\gamma p}$ , where  $\sigma_{\text{tot}}^{\gamma p}$  is the photoproduction cross section for real photons. The quantity  $R$  which is often referred to in literature is defined as

$$R(Q^2, \nu) = \frac{\sigma_L}{\sigma_T} \quad (1.28)$$

### 1.3 Quark Parton Model

First hints for a proton substructure came in the late 1960s where two surprising features appeared as the momentum transfer was increased and  $W$  was beyond the resonance region. The measured cross section in deep inelastic scattering [B 69a, B 69b] only showed a weak falloff with increasing  $Q^2$  where the cross section was about one to two orders of magnitude greater than expected (figure 1.6).

The second feature, scaling, was found by following a suggestion of Bjorken, his Scaling Hypothesis [Bjo69]. He assumed that in the limit of  $Q^2 \rightarrow \infty$  and  $\nu \rightarrow \infty$  the two quantities  $\nu W_2$  and  $W_1$  should become functions only of the ratio  $x = Q^2/2M\nu$ ; that is

$$MW_1(Q^2, \nu) \rightarrow F_1(x) \quad (1.29)$$

$$\nu W_2(Q^2, \nu) \rightarrow F_2(x) \quad (1.30)$$

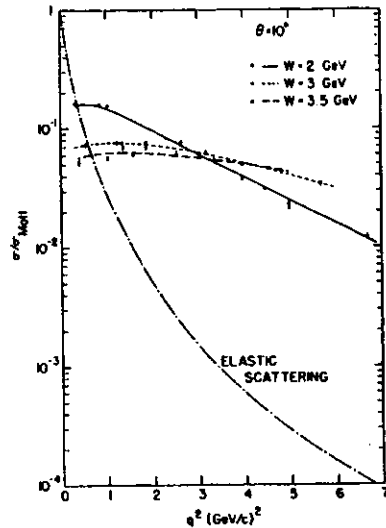


Figure 1.6: The ratio of the measured deep inelastic cross section and the Mott cross section versus  $q^2$ . This was one of the earliest examples of the relatively large cross section and weak  $q^2$  dependence which suggested point-like nucleon constituents. (From [B 69b])

and the cross section can be written as

$$\frac{d^2\sigma}{dx dQ^2} = \frac{4\pi\alpha^2}{xQ^4} \left[ (1-y)F_2(x) + xy^2F_1(x) \right]. \quad (1.31)$$

This scaling behavior was confirmed in experiments [FK72] (figure 1.7) and is characteristic for scattering of point-like objects.

This result led to attempts to interpret deep inelastic electron nucleon scattering by elastic scattering of electrons on point-like parton constituents where the physical interpretation to the observed scaling is given by the Quark Parton Model introduced by Feynman in 1969 [Fey69].

In this model, the proton is seen as a stream of parallel moving partons, each carrying a fraction  $xp$  of the proton's 4-momentum  $p$  in a frame with infinite momentum where transverse momenta are neglected. It is further assumed that the photon-parton interaction takes place at shorter time scales than the interaction between the partons. The electron is then elastically scattered on a quasi-free single parton. It can be shown that in this model the Bjorken- $x$  can be related to the fraction of the proton's momentum which is carried by the struck parton. Assuming a parton with spin  $\frac{1}{2}$ , a charge of  $e_i$  and  $q_i(x)dx$  specifying the probability for finding a parton of type  $i$  with a momentum fraction  $x$ , the cross section for deep inelastic electron nucleon scattering becomes

$$\frac{d^2\sigma}{dx dQ^2} = \frac{4\pi\alpha^2}{Q^4} \left( 1 - y + \frac{y^2}{2} \right) \sum_{i=1}^N e_i^2 q_i(x) \quad (1.32)$$

where the sum runs over all  $N$  partons in the proton. Comparing 1.32 with equation 1.31

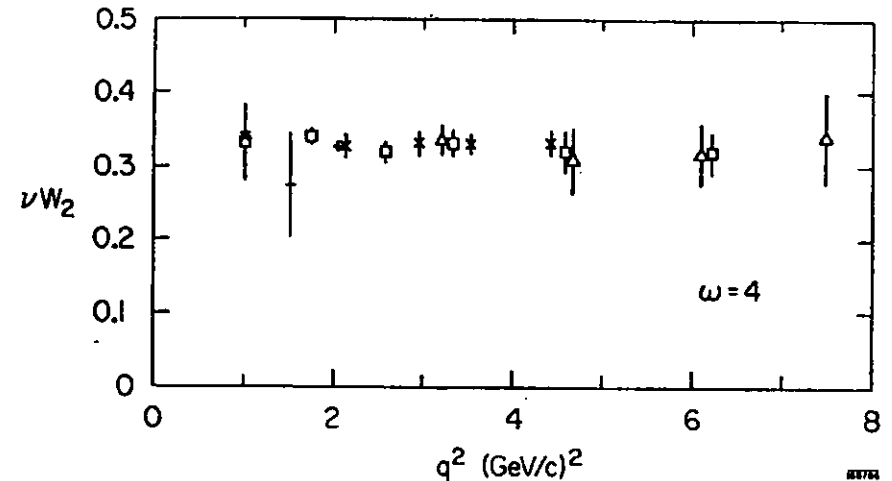


Figure 1.7: An early observation of scaling.  $\nu W_2$  for the proton as a function of  $q^2$  for  $W > 2$  GeV at  $\omega = 4 = 1/x$ . Results are from [B 69a, B 69b, M 72]. (Figure from [FK72])

leads to the following interpretation of the structure functions:

$$F_2(x) = x \sum_{i=1}^N e_i^2 q_i(x) \quad (1.33)$$

$$F_2(x) = 2xF_1(x). \quad (1.34)$$

Relation 1.34 is called the Callan-Gross relation [CG69] which is only true in this naive parton model and holds for partons with spin  $\frac{1}{2}$ . With deviations due to QCD contributions this relation has been experimentally proven [B 79] (figure 1.8) for large values of  $x$  and  $Q^2$ , showing that the partons have spin  $\frac{1}{2}$ .

Beside other hints this indicates that the partons can be identified with the quarks independently predicted by Gell-Mann [GM64] and Zweig [Zwe64] in 1964.

If all of the proton's momentum were carried by the  $N$  quarks inside the proton,  $N$  times the integral  $\int_0^1 xq(x)dx$  should be equal to one, otherwise  $N \int_0^1 xq(x)dx = 1 - \epsilon$ . From

$$\int_0^1 F_2(x)dx = \frac{1}{N} \sum_{i=1}^N e_i^2 (1 - \epsilon) \quad (1.35)$$

and the measured structure function  $F_2$  yields  $\int_0^1 F_2(x)dx = 0.18$  [M72] compared to  $\frac{1}{N} \sum e_i^2 = 1/3$ . This shows that about half of the nucleon momentum is carried by other proton constituents: the gluons whose influence on the structure function will be discussed in more detail in the next section.

In the QCD inspired quark parton model the proton is seen to consist of three valence quarks (uud), the mediating gluons and a distribution of quark-anti-quark pairs called sea quarks.

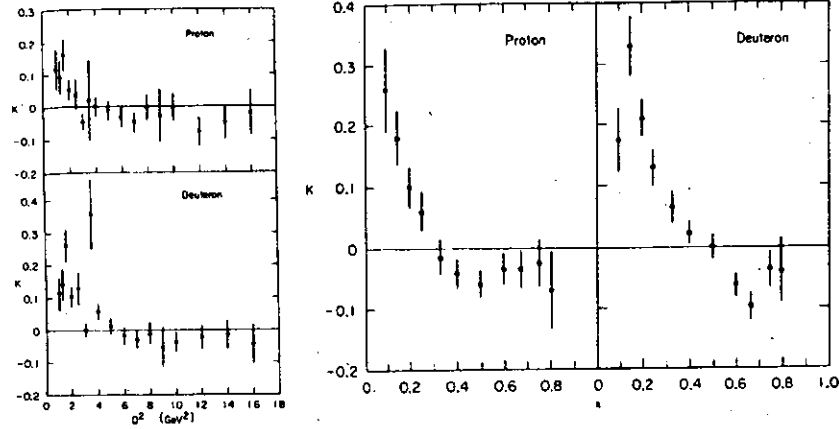


Figure 1.8: Values of  $K = \frac{F_2}{2xF_1} - 1$  averaged over  $x$  plotted against  $Q^2$  and averaged over  $Q^2$  plotted against  $x$  for the proton and deuteron. Significant differences from the Callan-Gross relation are seen at low values of  $x$  and  $Q^2$ . These deviations are due to gluon contributions. (From [B 79])

In this less naive approach the density of the anti-quarks  $\bar{q}_i$  has to be introduced and at high values of  $Q^2$  the exchange of the  $Z^0$  weak boson will start to contribute. Thus the double differential NC electron(positron)-proton cross section (equation 1.31) has to be written in the general form

$$\frac{d^2\sigma^{NC}(e^\pm p)}{dx dQ^2} = \frac{4\pi\alpha^2}{xQ^4} \left[ y^2 x F_1(x, Q^2) + (1-y) F_2(x, Q^2) \mp \left( y - \frac{y^2}{2} \right) x F_3(x, Q^2) \right] \quad (1.36)$$

where the structure functions now include both  $\gamma$  and  $Z^0$  exchange and  $F_3$  describes the electro-weak contributions. The nucleon structure functions are related to the quark density distributions by

$$F_1(x, Q^2) = \frac{1}{2x} F_2(x, Q^2) \quad (1.37)$$

$$F_2(x, Q^2) = \sum_f A_f(Q^2) [xq_f(x, Q^2) + x\bar{q}_f(x, Q^2)] \quad (1.38)$$

$$xF_3(x, Q^2) = \sum_f B_f(Q^2) [xq_f(x, Q^2) - x\bar{q}_f(x, Q^2)] \quad (1.39)$$

where  $q_f(x, Q^2)$  and  $\bar{q}_f(x, Q^2)$  represent the probability distribution for a quark or anti-quark of flavor  $f$  to be found in the proton. The coefficients  $A_f$  and  $B_f$  are given by

$$A_f(Q^2) = e_f^2 - 2e_f c_a^f c_v^f P_Z(Q^2) + [(c_v^f)^2 + (c_a^f)^2] [(c_v^f)^2 + (c_a^f)^2] P_Z^2(Q^2) \quad (1.40)$$

$$B_f(Q^2) = -2e_f c_a^f c_v^f P_Z(Q^2) + 4c_v^f c_a^f c_v^f P_Z^2(Q^2) \quad (1.41)$$

where the subscripts  $e$  and  $f$  refer to an electron or a quark respectively. The first term of the coefficient  $A_f$  arises from the exchange of the virtual photon and gives the  $F_2$  of equation 1.33. The last term is the result of the  $Z^0$  exchange whereas the middle term represents the interference term. The neutral current axial coupling constants  $c_a^f$  and  $c_v^f$

$$c_a^i = T_i^3 \quad (1.42)$$

and the vector coupling constants  $c_v^f$  and  $c_a^f$

$$c_v^i = T_i^3 - 2e_i \sin^2 \Theta_W \quad (1.43)$$

are expressed in terms of the third component of the weak isospin  $T_i^3$  and the Weinberg angle  $\Theta_W$ .  $P_Z(Q^2)$  is the ratio of the  $\gamma$  and  $Z^0$  propagators

$$P_Z(Q^2) = \frac{Q^2}{Q^2 + M_Z^2} \quad (1.44)$$

with  $M_Z$  being the mass of the  $Z^0$  boson. In QCD perturbation theory the Callan-Gross relation is no longer strictly fulfilled and thus is expressed by the longitudinal structure function  $F_L$ :

$$F_L(x, Q^2) = F_2(x, Q^2) - 2xF_1(x, Q^2). \quad (1.45)$$

In terms of this structure function the NC electron(positron)-proton cross section can be written in the form

$$\frac{d^2\sigma^{NC}(e^\pm p)}{dx dQ^2} = \frac{2\pi\alpha^2}{xQ^4} [Y_+ F_2(x, Q^2) - y^2 F_L(x, Q^2) \mp Y_- x F_3(x, Q^2)] \quad (1.46)$$

with  $Y_\pm = 1 \pm (1-y)^2$ .

## 1.4 QCD Evolution Equations

Quantum chromodynamics (QCD) predicts that the quarks inside the proton can not be regarded as completely free but couple to the mediating bosons of the strong force: the gluons. The proton therefore is not simply composed of three point-like valence quarks as in the naive quark parton model. As  $Q^2$  increases more and more substructure of the proton is resolved as the photon may scatter on a sea quark which originates from a gluon ( $g \rightarrow q\bar{q}$ ) itself radiated from one of the valence quarks. By increasing the resolution the apparent number of partons which share the proton's momentum increases and hence there is an increased chance of finding a quark at small  $x$  and a decreasing chance of finding one at high  $x$ .

The contributing diagrams of  $\mathcal{O}(\alpha_s)$  are shown in figure 1.9 and the inclusion of these diagrams into cross section calculations leads to scaling violations, meaning that the structure functions and hence the parton distributions at a given  $x$  are no longer independent but vary with  $Q^2$  (figure 1.10).

In the QCD improved parton model a cross section can be factorized (somewhat arbitrarily) into a process dependent, elementary photon parton level cross section calculable by QCD and the process independent parton distribution function (PDF) which has to be measured by

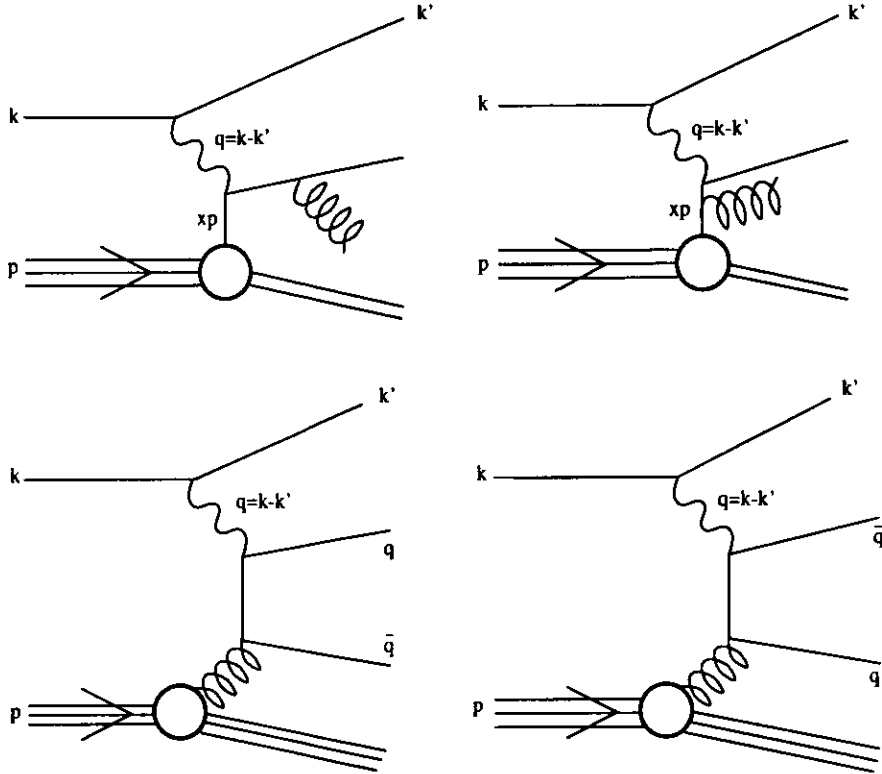


Figure 1.9: Lowest order gluon contributions to the  $ep$  scattering process.

experiment. The distribution obeys evolution equations which can be derived by perturbative QCD.

A physical quantity  $C_a$  when calculated perturbatively in QCD is expanded as a power series in the strong coupling constant  $\alpha_s$ ,

$$C_a = C_a^{(0)} + C_a^{(1)} \left( \frac{\alpha_s}{2\pi} \right) + C_a^{(2)} \left( \frac{\alpha_s}{2\pi} \right)^2 + \dots \quad (1.47)$$

where the coefficients  $C_a^n$  are usually evaluated using Feynman diagrams. The terms in equation 1.47 are called lowest or Born term, first order correction, second order correction and so on. The leading order (LO) calculation gives only the first non-zero term in the series whereas the next-to-leading order (NLO) calculations gives the next term and so on.

In case of deep inelastic scattering a structure function  $F(x, Q^2)$  factorizes as

$$F(x, Q^2) = \sum_a \int_x^1 \frac{dz}{z} C_a \left( \frac{x}{z}, \alpha_s(\mu^2), \frac{Q^2}{\mu^2} \right) f_a(z, \mu^2) + \mathcal{O} \left( \frac{\Lambda^2}{Q^2} \right) \quad (1.48)$$

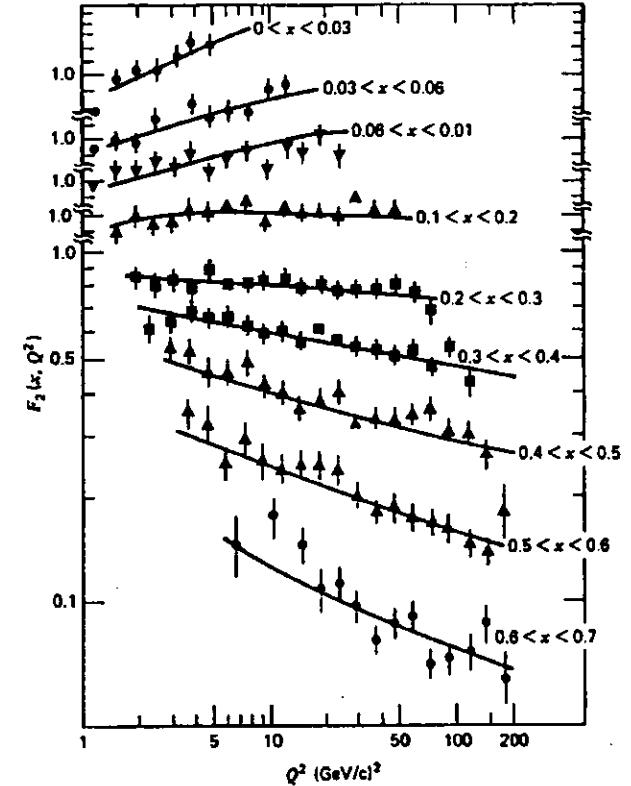


Figure 1.10: Deviations from scaling. The structure function  $F_2(x, Q^2)$  increases with  $Q^2$  at small  $x$  and decreases at large  $x$ . (From [HM84])

where the  $C_a$  are the process dependent coefficient functions containing all the  $Q^2$  dependence,  $f_a$  the universal, non-perturbative process independent parton distributions of the hadron under consideration and the sum is running over all quarks, anti-quarks and gluons.  $\Lambda$  is the QCD scale parameter which marks the boundary between the scenarios of asymptotic freedom where the partons are quasi-free and the range of large coupling where the quarks and gluons are strongly bound into hadrons. This parameter is found to be in the range of 200 - 300 MeV. The scale  $\mu^2$  is an arbitrary factorization scale ( $\mu^2 \gg \Lambda^2$ ) defining the separation between short distance and long distance effects. Hence any propagator being more than  $\mu^2$  off-shell will contribute to  $C_a$ , otherwise to  $f_a$ . The left part of this equation is an observable which cannot depend on the factorization scale, thus

$$\mu^2 \frac{dF(x, Q^2)}{d\mu^2} = 0 \quad (1.19)$$

leading to an evolution equation for the parton distributions

$$\frac{df_a(x, Q^2)}{d \ln Q^2} = \sum_b \int_x^1 \frac{dz}{z} P_{ab}(z, \alpha_s(\mu^2)) f_b\left(\frac{x}{z}, \mu^2\right) \quad (1.50)$$

known as the DGLAP evolution equation [Dok77, GL72, AP77]. The so called splitting functions  $P_{ab}$  and the coefficient functions  $C_a$  are calculable by perturbative QCD

$$P_{ab}(z, \alpha_s) = \sum_{n=1}^{\infty} \left(\frac{\alpha_s}{2\pi}\right)^n P_{ab}^{n-1}(z) \quad (1.51)$$

$$C_a(z, \alpha_s) = \alpha_s^p \left[ C_a^{(0)} + C_a^{(1)} \left(\frac{\alpha_s}{2\pi}\right) + C_a^{(2)} \left(\frac{\alpha_s}{2\pi}\right)^2 + \dots \right]. \quad (1.52)$$

For the structure function  $F_2$  the exponent  $p = 0$  and the coefficient  $C_a^0 = e_a^2 \delta(1-z)$  and the naive quark parton model equation 1.33 can be seen as the zeroth approximation in a perturbative expansion in  $\alpha_s$ .

In leading order QCD approximation the DGLAP evolution equations for the quark distributions take the form

$$\frac{dq(x, Q^2)}{d \ln Q^2} = \frac{\alpha_s}{2\pi} \int_x^1 \frac{dy}{y} \left[ q(y, Q^2) P_{qq}\left(\frac{x}{y}\right) + g(y, Q^2) P_{gq}\left(\frac{x}{y}\right) \right] \quad (1.53)$$

where to lowest order in  $\alpha_s$

$$P_{qq}(z) = \frac{4}{3} \left( \frac{1+z^2}{1-z} \right) \quad (1.54)$$

$$P_{gq}(z) = \frac{1}{2} [z^2 + (1-z)^2]. \quad (1.55)$$

There is an equivalent equation to 1.53 giving the evolution of the gluon distribution

$$\frac{dg(x, Q^2)}{d \ln Q^2} = \frac{\alpha_s}{2\pi} \int_x^1 \frac{dy}{y} \left[ g(y, Q^2) P_{gg}\left(\frac{x}{y}\right) + \sum_i q_i(y, Q^2) P_{gq}\left(\frac{x}{y}\right) \right] \quad (1.56)$$

where  $i$  runs over all flavors of quarks and anti-quarks and the splitting functions  $P_{qq}$  and  $P_{gq}$  are given by

$$P_{gg}(z) = \frac{4}{3} \left[ \frac{1+(1-z)^2}{y} \right] \quad (1.57)$$

$$P_{gq}(z) = 6 \left[ \frac{1-z}{z} + \frac{z}{1-z} + z(1-z) \right]. \quad (1.58)$$

The evolution equations 1.53 and 1.56 allow to compute the quark gluon densities and therefore the structure functions at any  $Q^2$  if the distributions  $q(x, Q^2)$  and  $g(x, Q^2)$  are given at some reference point  $Q_0^2$ . The functions  $P_{ij}$  are called splitting functions and can be interpreted as the probability for a parton  $i$  to split into partons  $j$  and  $k$  carrying fraction  $z$  and  $(1-z)$  of its momentum respectively. Figure 1.11 illustrates how a low- $x$  quark interacting with the photon is produced via a parton ladder by repeated gluon radiation and quark-anti-quark pair production.

It should be mentioned that the evolution equations 1.53 and 1.56 only fix the  $Q^2$ -dependence of the parton densities but neither their  $x$ -dependence nor their absolute scale.

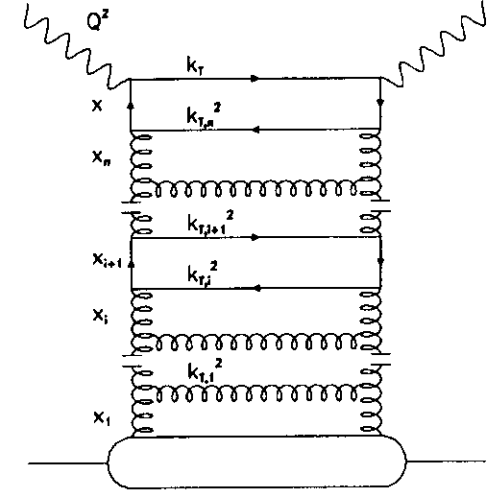


Figure 1.11: Production of a low- $x$  quark via a parton ladder by recursive emission of gluons and production of  $q\bar{q}$  pairs.

As the next-to-leading order splitting and coefficient functions are well known, the next to leading order DGLAP evolution is well justified in the region of moderate  $x$  where the only large scale is  $\ln(Q^2)$ .

In the leading order  $\ln(Q^2/\Lambda^2)$  approximation (LLA) (with only  $P_{ab}^0(z)$  included) which corresponds to keeping only those terms in the perturbation expansion which have the leading power of  $\ln(Q^2/\Lambda^2)$ , i.e.  $\alpha_s^n \ln^n(Q^2)$  the evolution equation describes a generalized parton evolution along a space-like cascade in which the successive transverse momenta  $k_T$  of the partons are strongly ordered. When an appropriate gauge is chosen the contributing diagrams in this approximation are ladder diagrams with gluon and quark exchange as shown in the left diagram of figure 1.12. In these diagrams the longitudinal momenta are ordered along the chain ( $x_i > x_{i+1}$ ) and the transverse momenta  $k_T$  are strongly ordered:

$$Q^2 \gg k_{T,n}^2 \gg \dots \gg k_{T,n-1}^2 \gg k_{T,1}^2 \quad (1.59)$$

$$1 > y > x_1 > \dots > x_{n-1} > x. \quad (1.60)$$

It should be noted that it is at present not clear whether the factorization theorem of equation 1.48 holds in the very low  $x$  region since it is based on two approximations.

First of all higher twist terms (i.e. contributions from interactions of many partons in the hard scattering) are neglected. Furthermore the coefficients  $C_a$  and splitting functions  $P_{ab}$  are only evaluated to a fixed order in  $\alpha_s$  and the series is truncated at that point. The fixed order truncation combined with the resummation of only the  $\alpha_s^n \ln^n(Q^2)$  terms neglects terms of  $\ln(1/x)$  in the low  $x$  region where these terms become important since the splitting functions in the gluon sector are singular in  $x$ .

To extend the evolution of the parton distributions into the low  $x$  region different approaches are made.

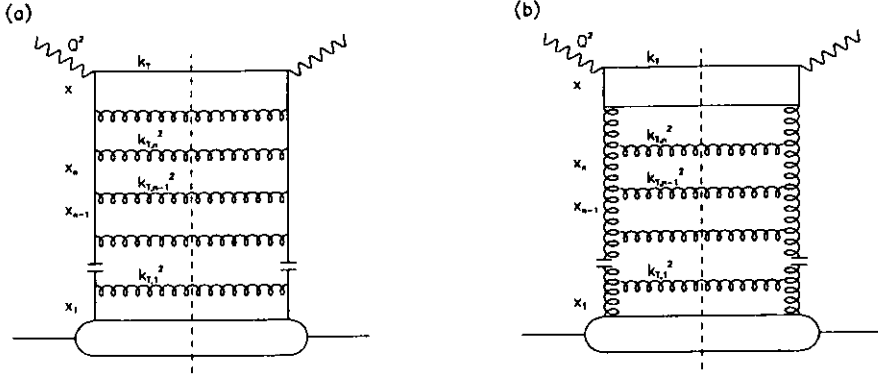


Figure 1.12: Diagrams representing the  $F_2$  contributions by the leading-log approximation (a) and double leading log approximation (b).

### The DGLAP Equation at Low Values of $x$

In the region of low  $x$  and low  $Q^2$  where the terms  $\ln(1/x)$  and  $\ln(Q^2/\Lambda^2)$  are comparable, both large logarithms are kept leading to the so called double leading logarithmic approximation (DLA). Assuming that at small values of  $x$  the gluons dominate and give the only contribution to the evolution, the quark distributions  $q(x, Q^2)$  are dropped and the DGLAP equation for the gluons  $g(x, Q^2)$  decouples from the quark distribution and becomes

$$\frac{dg(x, Q^2)}{d \ln Q^2} = \frac{\alpha_s}{2\pi} \int_x^1 \frac{dy}{y} P_{gg} \left( \frac{x}{y} \right) g(y, Q^2). \quad (1.61)$$

At small values of  $x$  the splitting function  $P_{gg}$  can be approximated by the term

$$P_{gg}^{(0)} \simeq 6/z \quad (1.62)$$

and the DGLAP equation 1.61 can be solved explicitly, resulting in

$$xg(x, Q^2) \sim \exp \left[ \sqrt{\frac{144}{33 - 2N_f} \ln \left( \frac{\ln(Q^2/\Lambda^2)}{\ln(Q_0^2/\Lambda^2)} \right) \ln \left( \frac{1}{x} \right)} \right] \quad (1.63)$$

for the gluon distribution with  $N_f$  giving the number of active quark flavors. Thus as  $x \rightarrow 0$  it is seen that the DLL summation implies that  $xg$  grows faster than any power of  $\ln(1/x)$ . The DLL behavior can be identified with the sum of ladder diagrams shown in the right diagram of figure 1.12 where the longitudinal and transverse momenta are strongly ordered:

$$Q^2 \gg k_{T,n}^2 \gg \dots \gg k_{T,n-1}^2 \gg k_{T,1}^2 \quad (1.64)$$

$$y \gg x_1 \gg \dots \gg x_{n-1} \gg x. \quad (1.65)$$

### BFKL at Low Values of $x$

The double leading logarithmic approximation only includes the leading  $\ln(1/x)$  terms which are accompanied by leading  $\ln(Q^2)$  terms whereas for the low  $x$  region the leading  $\ln(1/x)$  term must be summed by keeping the full  $Q^2$  dependence not just leading  $\ln(Q^2)$  terms. The BFKL summation can be pictured as a sum of gluon ladder diagrams seen in figure 1.13 where the strong ordering in transverse momenta is dropped and the integration has to be carried out on the entire phase space.

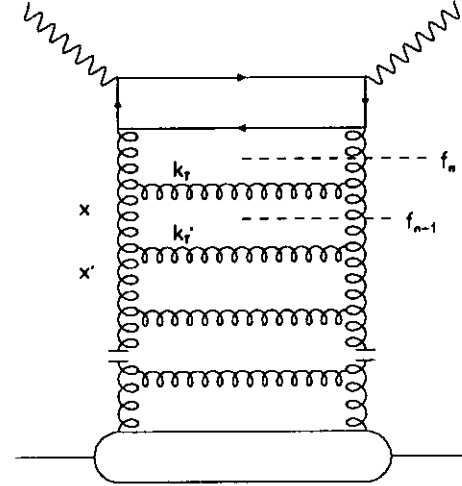


Figure 1.13: Representation of the BFKL recursion relation 1.66 via a ladder diagram.

The resummation of the terms involving  $\alpha_s^n \ln^n(1/x)$  was done by Balitskii, Fadin, Kuraev and Lipatov [BL78, KLF77] and leads to the BFKL equation.

$$f_n(x, k_T^2) = \int_x^1 \frac{dx'}{x'} \int dk_T'^2 K(k_T, k_T') f_{n-1}(x', k_T'^2) = K \oplus f_{n-1} \quad (1.66)$$

where  $f_g$  is related to the integrated gluon distribution  $xg(x, Q^2)$  through

$$xg(x, Q^2) = \int_0^{Q^2} \frac{dk_T^2}{k_T^2} f_g(x, k_T^2) \quad (1.67)$$

and

$$f_g(x, k_T^2) = \sum_{n=0}^{\infty} f_n(x, k_T^2). \quad (1.68)$$

This equation can be solved for fixed  $\alpha_s$  leading to

$$xg(x, Q^2) \sim x^{-\lambda} \quad (1.69)$$

with

$$\lambda = \frac{12 \ln 2}{\pi} \alpha_s = \frac{\alpha_s}{0.378} \quad (1.70)$$

and the usual value quoted for  $\lambda$  is 0.5.

### GLR

In the very low  $x$  region one expects an increase of the parton densities as predicted by the BFKL evolution and therefore an indefinitely rising of  $F_2$ . This rise of  $F_2$  is the consequence of the increasing quark density due to pair production from gluon emission. The resulting increase in the growth of the total cross section is however limited by the Froissart bound [Fro61] which requires that the total photon-proton cross section  $\sigma_{\text{tot}}^{\gamma p}$  does not rise above the proton radius  $R$

$$\sigma_{\text{tot}}^{\gamma p} \ll \pi R^2 (\ln s)^2. \quad (1.71)$$

Together with equation 1.26 and the result of the BFKL approximation  $F_2 \sim x^{-\lambda_0 \alpha}$ , equation 1.71 becomes

$$\frac{4\pi^2 \alpha}{Q^2} x^{-\lambda_0 \alpha} \ll \pi R^2 (\ln s)^2. \quad (1.72)$$

Therefore the Froissart bound would be violated if  $x$  goes below certain values of  $x_{\text{crit}}$  where the cross section reaches the Froissart bound. Thus shadowing and recombination effects of quarks and anti-quarks are expected to limit the rise of  $F_2$ . This recombination effects could be represented by additional non-linear terms to the BFKL equations and give the Gribov-Livin-Ryskin (GLR) evolution [GLR81]:

$$\frac{\delta f(x, k_T^2)}{\delta \log 1/x} = K \otimes f - \frac{81 \alpha_s^2 (k_T^2)}{16 R^2 k_T^2} [xg(x, k_T^2)]^2. \quad (1.73)$$

The validity regions of the different evolutions in the  $x$ - $Q^2$ -plane are shown in figure 1.14.

## 1.5 Parton Distributions

In the naive QPM the fraction of the nucleon momentum which is carried by the single quarks is described by parton distribution functions (PDFs). In the QCD-improved theory the PDFs have a less straight forward interpretation. An example of parton distribution functions for the valence quarks, sea quarks and gluons for different values of  $Q^2$  is shown in figure 1.15. The  $Q^2$  dependence of the parton parameterizations can be described by QCD evolution equations but the absolute value and  $x$ -dependence has to be measured by experiment.

### 1.5.1 Fixed Target DIS Experiments

A summary of fixed target experiments is given in table 1.1 and some of these experiments will be briefly mentioned here. Common to all these experiments is a stationary target and a lepton beam (e or  $\mu$  and  $\nu$ ).

The SLAC data [B92] was obtained from electron scattering on a hydrogen and deuterium target with  $Q^2$  in the range of 0.6 GeV<sup>2</sup> up to 30.0 GeV<sup>2</sup>.

The Bologna, CERN, Dubna, Munich Saclay (BCDMS) experiment [BCD89] involved the scattering of muons from a hydrogen target where incident beam energies of 100, 120, 200 and

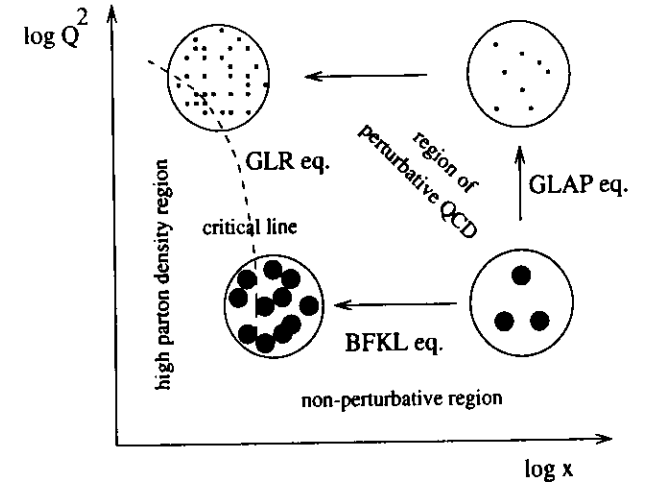


Figure 1.14: Validity of the various evolution equations in the  $x$ - $Q^2$  region. The proton content is schematically represented indicating how the spatial resolution increases with  $Q^2$  where the number of partons stays approximately the same (DGLAP evolution) and the number of partons increases with decreasing  $x$  (BFKL evolution). At very low values of  $Q^2$  perturbative QCD is no longer applicable. The region left to the critical line compares to the region where the rise in  $F_2$  is suppressed by shadowing and recombination effects of the partons. (From [Mar93])

280 GeV were used. This corresponds to a coverage of  $x$  between 0.06 and 0.8 and  $Q^2$  between 7 GeV<sup>2</sup> and 260 GeV<sup>2</sup>.

The New Muon Collaboration (NMC) data [NMC92] was obtained by scattering muons of initial energy between 90 and 280 GeV on a liquid hydrogen target. The kinematic range covered is  $0.006 < x < 0.6$  and  $0.5 < Q^2 < 55 \text{ GeV}^2$ .

The European Muon Collaboration (EMC) [EMC87] measured the nucleon structure function by scattering muons on a deuterium target and covered the range of  $7 < Q^2 < 170 \text{ GeV}^2$  and  $0.03 < x < 0.75$ .

The HERA accelerator (refer chapter 2) with the experiments ZEUS and H1 allows to explore a new kinematic region of deep inelastic electron proton scattering and figure 1.16 shows a comparison of the kinematic regions covered by the fixed target and HERA experiments.

### 1.5.2 Parameterizations of Parton Densities

The QCD improved quark parton model gives an interpretation of the measured cross section in terms of quark densities but does not provide a prediction of the parton distributions. Starting with a parameterization at a given  $x$  at a reference point  $Q_0^2$  the quark distribution can be evolved using the QCD evolution equations mentioned in section 1.4.

Several different approaches for the parameterizations of the parton densities have been made by three groups: Martin, Roberts, Stirling (MRS), the CTEQ collaboration and Glück, Reya, Vogt (GRV). In general there are two different approaches to obtain PDFs: global fits

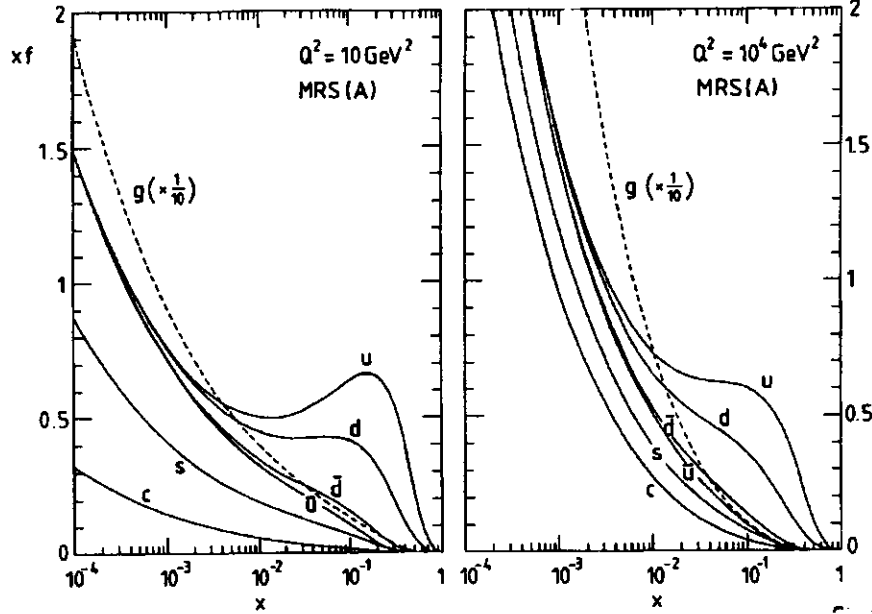


Figure 1.15: Parton distributions as a function of  $x$  at  $Q^2 = 10 \text{ GeV}^2$  and  $Q^2 = 10^4 \text{ GeV}^2$  for the MRS(A) parameterization. (From [MRS94])

to the data (MRS and CTEQ) and radiative generation of the partons (GRV). In the global fit approach a functional form of the parton distribution at some given point  $Q_0^2$  is used and fitted to the data after the appropriate evolution.

## MRS

The earliest Martin-Roberts-Stirling (MRS) parameterizations [MRS93] were obtained by a global next-to-leading order (NLO) QCD fit including DIS data from BCDMS, EMC, NMC and CCFR. The MRSA analysis [MRS94] is based on data from BCDMS, NMC, CCFR, EMC, H1, ZEUS, WA70, E605, NA51, UA2, CDF and D0 and uses the following functional forms for the valence quark ( $u_v = u - \bar{u}$ ,  $d_v = d - \bar{d}$ ), sea quark ( $S = 2(\bar{u} + \bar{d} + \bar{s} + \bar{c})$ ) and gluon ( $g$ ) distributions

$$x u_v = A_u x^{\alpha_u} (1-x)^{\beta_u} (1 + \epsilon_u \sqrt{x} + \gamma_u x) \quad (1.74)$$

$$x d_v = A_d x^{\alpha_d} (1-x)^{\beta_d} (1 + \epsilon_d \sqrt{x} + \gamma_d x) \quad (1.75)$$

$$x S = A_s x^{-\lambda_s} (1-x)^{\beta_s} (1 + \epsilon_s \sqrt{x} + \gamma_s x) \quad (1.76)$$

$$x g = A_g x^{-\lambda_g} (1-x)^{\beta_g} (1 + \epsilon_g \sqrt{x} + \gamma_g x) \quad (1.77)$$

where a starting value  $Q_0^2 = 4 \text{ GeV}^2$  was used. A fit to the 1992 HERA data with  $\epsilon_g = 0$

Experiment	beam	target	measurements	$x$	$Q^2 [\text{GeV}^2]$	
BCDMS	NA4	$\mu$	C	$F_2$	0.25...0.75	25...260
			H <sub>2</sub> , D <sub>2</sub>	$F_2, R$	0.07...0.75	7...260
BEBC	WA25	$\nu$	D <sub>2</sub>	$F_2, xF_3$	0.028...0.7	0...64
	WA21	$\nu$	H <sub>2</sub>	$q^v, \bar{q}^v, \bar{q}^v$	0.1...0.7	8.6...14.2
CCFR		$\nu$	Fe	$F_2, xF_3$	0.015...0.7	1.3...200
CHARM	WA18	$\nu$	CaCO <sub>3</sub>	$F_2, xF_3, F_L$	0.02...0.4	0.8...18.9
CHIO		$\nu$	H <sub>2</sub> , D <sub>2</sub>	$F_2, R$	0.0005...0.7	0.2...80
CDHS	WA1	$\nu$	Fe	$F_2, xF_3, R$	0.015...0.65	0.5...200
CDHSW	WA1/2	$\nu$	Fe	$F_2, xF_3, F_L, \bar{q}^v$	0.015...0.65	0.19...200
BFP		$\mu$	Fe	$F_2$	0.08...0.65	5.5...220
E665		$\mu$	H <sub>2</sub> , D <sub>2</sub> , A	$F_2$	0.0009...0.37	0.2...65
EMC	NA2	$\mu$	Fe	$F_2$	0.03...0.8	2...250
			H <sub>2</sub> , D <sub>2</sub>	$F_2$	0.03...0.75	7...170
EMC	NA28	$\mu$	D <sub>2</sub>	$F_2$	0.002...0.17	0.2...8
NMC	NA37	$\mu$	H <sub>2</sub> , D <sub>2</sub> , A	$F_2$	0.006...0.6	0.8...75
			H <sub>2</sub> , D <sub>2</sub> , A	$F_2^n/F_2^p, F_2^A/F_2^A'$	0.003...0.7	0.17...100
SLAC		$e$	H <sub>2</sub> , D <sub>2</sub>	$F_2, R$	0.07...0.85	0.5...20

Table 1.1: Summary of fixed target experiments. [Hag95]

and  $\lambda_s = \lambda_g = \lambda$  gave a value of  $\lambda = 0.3 \pm 0.1$ . The 1993 HERA data however was lying below MRS(A) (and CTEQ) at low  $x$  and MRS tried two things: A refit (MRSA') with  $\epsilon_g \neq 0$  on the new data and a new fit (MRSg) with  $\lambda_g \neq \lambda_s$ . The MRSA' fit led to  $\lambda = 0.17$ , substantially smaller than 0.3. The MRSg fit gave  $\lambda_g = 0.301$  and  $\lambda_s = 0.067$ , indicating that the sea distribution might be flat and the gluon distribution steep. MRS suggests that the difference might be due to the inappropriate use of the DGLAP evolution in the region of low  $Q^2$ .

## CTEQ

The CTEQ<sup>3</sup> group also performs a NLO global QCD fit allowing a flavor asymmetric sea and a singular gluon behavior at low  $x$ . The initial parameterization CTEQ1 [B93b] was based on BCDMS, NMC and CCFR data with a reference value of  $Q_0^2 = 4 \text{ GeV}^2$  and  $\lambda = 0.5$ . The CTEQ3 analysis [L95] is based on the measurements of various DIS measurements (BCDMS, NMC, ZEUS, H1, CCFR and NMC), Drell-Yan (E605, CDF, NA-51) and direct photoproduction (WA70, E706, UA6). Their input parameterizations are fixed at  $Q_0^2 = 2.6 \text{ GeV}^2$  and the functional forms used for the valence ( $u_v, d_v$ ), sea ( $\bar{d}, \bar{u}$ ) and strange quarks ( $s$ ) as well as for the gluons ( $g$ ) are given by

$$x u_v = a_0^u x^{\alpha_u} (1-x)^{\beta_u} (1 + a_3^u x^{\alpha_3^u}) \quad (1.78)$$

$$x d_v = a_0^d x^{\alpha_d} (1-x)^{\beta_d} (1 + a_3^d x^{\alpha_3^d}) \quad (1.79)$$

$$x g = a_0^g x^{\alpha_g} (1-x)^{\beta_g} (1 + a_3^g x) \quad (1.80)$$

<sup>3</sup>Coordinated Theoretical/Experimental Project on QCD

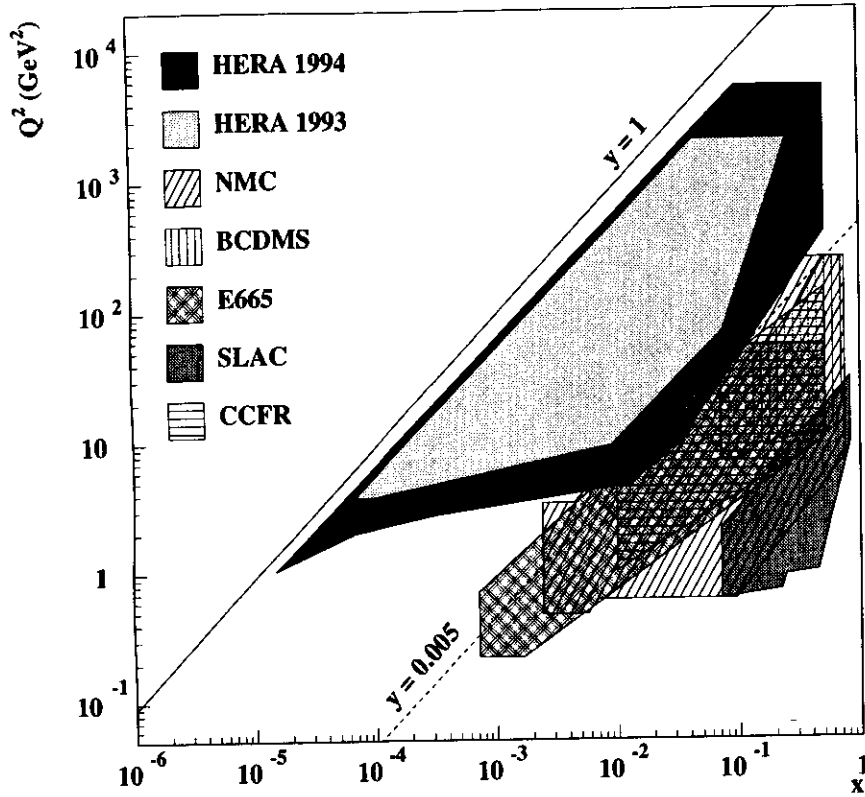


Figure 1.16: The kinematic coverage of various fixed target experiments compared to the range accessible by the HERA experiments in the years 1993 and 1994.

$$x(\bar{d} + \bar{u})/2 = a_0^+ x^{a_1^+} (1-x)^{a_2^+} (1 + a_3^+ x) \quad (1.81)$$

$$x(\bar{d} - \bar{u}) = a_0^- x^{a_1^-} (1-x)^{a_2^-} (1 + a_3^- x) \quad (1.82)$$

$$xs = \kappa \cdot x(\bar{d} + \bar{u})/2. \quad (1.83)$$

### GRV

A different approach is taken by Glück, Reya and Vogt (GRV) [GRV90]. They treat the proton as consisting mainly of valence partons at very low  $Q_0^2 \sim 0.2 \text{ GeV}^2$  and they evolve the distribution up to the measured region of  $Q^2$ . Initial attempts which had no gluons and sea quarks at the starting value  $Q_0^2$  produced too soft gluon and sea distribution which did not fit the data [GR77]. By allowing 'valence-like' starting distributions for the gluons and sea quarks and taking into account charm quark mass effects more successful predictions were obtained. Their most recent parameterization is GRV94 [GRV95].

By additional constraints like  $a_2^g = a_1^+$  assuming an equal behavior of the sea and gluon distributions at low values of  $x$  or  $a_1^u = a_1^d = a_1^-$ , the number of free parameters is reduced to 15. Their fit results in a value of  $\lambda = 0.286$ .

## Chapter 2

### HERA

The world's first electron proton collider, the Hadronen Elektronen Ring Anlage (HERA) at the Deutsches Elektronen-Synchrotron in Hamburg (figure 2.1) allows to explore a new kinematic region of inelastic electron proton scattering by colliding electrons of 27.5 GeV energy and protons with 820 GeV which corresponds to  $\sqrt{s} \approx 300$  GeV center of mass energy.



Figure 2.1: Bird eye's view of the DESY area in the north-western part of Hamburg. The dashed lines show the location of the PETRA and HERA collider. The ZEUS experiment is located in the South Hall (S).

#### 2.1 The Electron-Proton Collider HERA

The machine is accommodated in a tunnel 10 - 30 m below the ground and has a circumference of 6336 m. The accelerator is accessible by four experimental halls where two are occupied by the first HERA experiments ZEUS [ZEU93d] and H1 [H1 93a]. The remaining halls are used by

the spin-physics fixed target experiment HERMES [HER93] which started to use the polarized electron beam in 1995 and the B-physics experiment HERA-B [HER94] which is currently under installation and will start its physics program in 1997. The layout of the HERA accelerator is shown in the right part of figure 2.2 where its design values are listed in table 2.1.

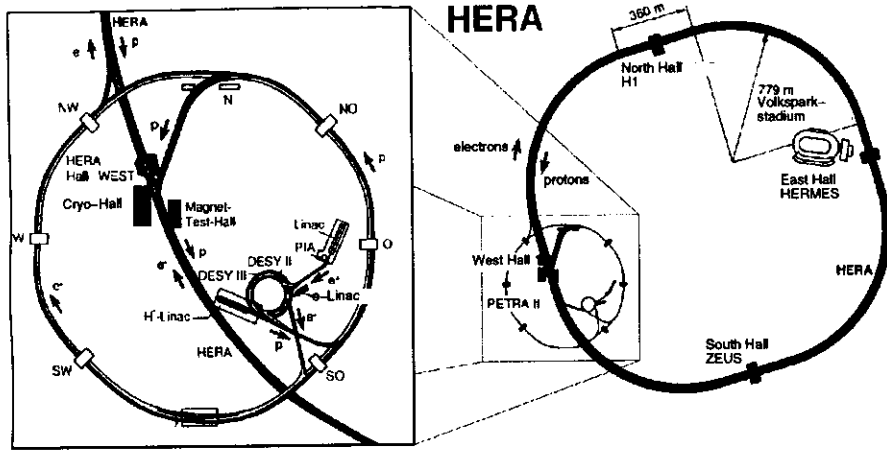


Figure 2.2: The HERA injection scheme.

HERA parameter	Design Value		Unit
	e-beam	p-beam	
Nominal energy	30	820	[GeV]
Injection energy	14	40	[GeV]
Luminosity	$1.5 \cdot 10^{31}$		$[\text{cm}^{-2}\text{s}^{-1}]$
Magnetic field	0.165	4.68	[T]
Circulating current	58	163	[mA]
Number of bunches	210		
Bunch crossing time	96		[ns]
Horizontal beam size $\sigma_x$	0.26	0.29	[mm]
Vertical beam size $\sigma_y$	0.02	0.07	[mm]
Longitudinal beam size	8.0	110	[mm]
Energy loss per turn	127	$1.4 \cdot 10^{-10}$	[MeV]

Table 2.1: Design values of the HERA accelerator as given in [Wii91].

The HERA injection scheme is shown in the left part of figure 2.2. Electrons (resp. positrons) start their way up through the machines in the electron linear accelerator (positrons are further accumulated in the Positron Intensity Accumulator PIA) from where they are injected into DESY II with an energy of 450 MeV. Here the electrons/positrons are accelerated up to 7 GeV

and transferred to PETRA which accelerates them up to 12 GeV, the HERA injection energy. Protons take a similar way, starting at the proton linear accelerator with 50 MeV, going through DESY III; leaving it with 7.5 GeV and being injected from PETRA into HERA with an energy of 40 GeV.

In the HERA design the proton beam currents reach up to 163 mA and the electron beam achieves currents of 58 mA. Both beams are split up into 210 bunches with a spacing of 28.8 m, leading to a bunch crossing time distance of 96 ns and an interaction rate of about 10 MHz.

## 2.2 HERA Operation in the Year 1994

The first electron-proton collisions at nominal beam energies were observed in 1992 where 9 colliding bunches were used and an integrated luminosity of  $33.5 \text{ nb}^{-1}$  was accumulated. During the following data taking periods these numbers have been subsequently increased and in the 1994 running period 168 electron and 170 proton bunches were filled. Out of these bunches 15 electron and 17 proton bunches remained unpaired. These so called pilot bunches were used to perform beam related background studies. Consequently 153 bunches remained for electron-proton collisions and their distribution is shown in figure 2.3.

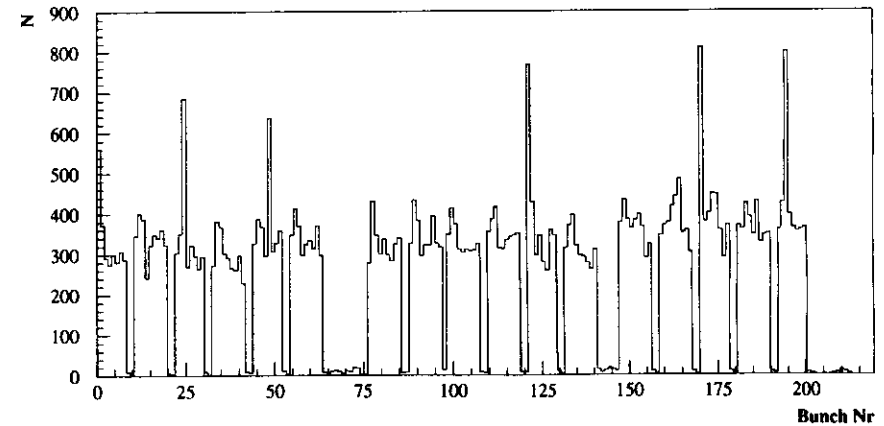


Figure 2.3: Distribution of the colliding electron and proton bunches as used by HERA in the 1994 running period.

The root mean square of the proton bunch length was about 20 cm compared to which the electron bunch length was negligible. The interaction region therefore was about 12 cm wide, centered at  $z = -6 \text{ cm}^1$ . About 5% of the proton current occurred in so called satellite bunches

<sup>1</sup>In the ZEUS coordinate system (see chapter 3) the positive z-axis points in the direction of the proton beam.

which result from the 208 MHz r.f. system used within the HERA machine to reduce the proton bunch length. These particles are about 4.8 ns off the main bunch crossing leading to a second interaction point at  $z = +78$  cm.

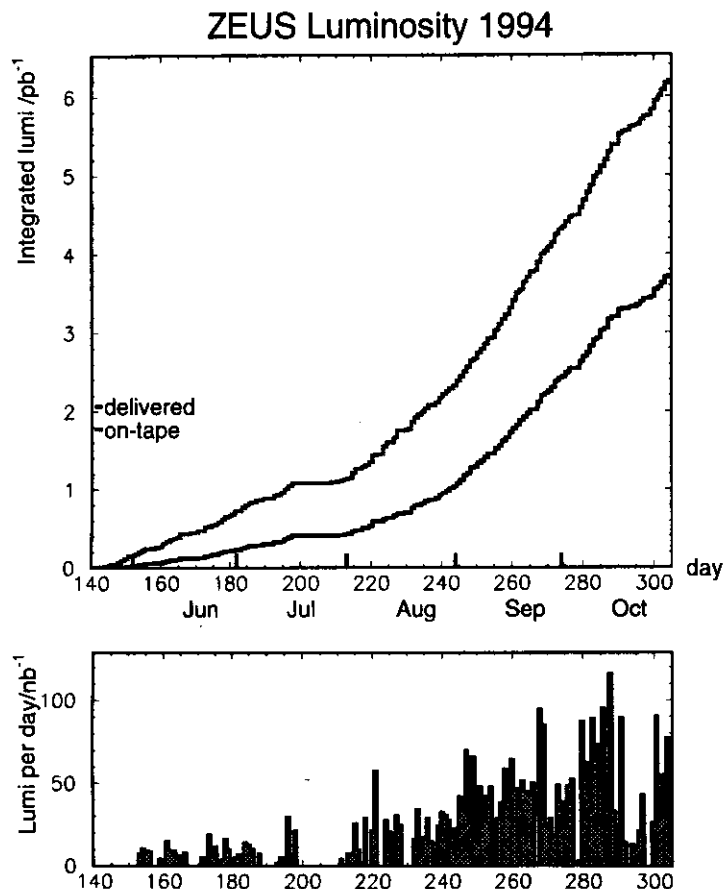


Figure 2.4: Luminosity per day (lower plot) and integrated luminosity delivered by HERA and written on tape by the ZEUS experiment (upper plot) in the year 1994. The plateau originating from the unavailability of the HERA machine during the transition from electron to positron operation is well seen. The slope is much steeper after switching to positrons due to their larger beam lifetime compared to the electron beams. (From [PZ95])

HERA started the 1994 luminosity operation at May 23<sup>rd</sup>, 1994, reaching proton beam currents up to 56 mA with an average of 38 mA. Lifetime limitations of the electron beam due to problems most likely originating from the ion pumps of the HERA vacuum system

led the HERA crew to operate with positrons instead of electrons, giving a much larger beam lifetime. The analysis described in this thesis is entirely based on the ZEUS data acquired during the positron running period. This implies that whenever electrons are referred to further on, positrons are meant. At August 8<sup>th</sup>, 1994, luminosity operation with positrons started and beam currents with an average of 24.6 mA were reached. Positron operation lasted for the remaining running period until October 31<sup>st</sup>, 1994, and mean luminosities of  $1.4 \cdot 10^{30} \text{ cm}^{-2} \text{ sec}^{-1}$  were achieved, giving a total integrated luminosity of  $6.2 \text{ pb}^{-1}$  ( $5.1 \text{ pb}^{-1}$  for positrons) (figure 2.4). From this delivered luminosity the ZEUS experiment gated about  $3.7 \text{ pb}^{-1}$  ( $3.3 \text{ pb}^{-1}$ ) of events which were written to tape. This number was further reduced by offline detector quality cuts so that  $3.3 \text{ pb}^{-1}$  ( $3.0 \text{ pb}^{-1}$ ) remained for physics analysis.

## Chapter 3

# The ZEUS Detector

ZEUS (figure 3.1) is a multipurpose detector taken into operation early 1992 by a collaboration of about 450 physicists from 50 institutes of 12 countries. ZEUS is asymmetric in the proton direction because of the movement of the electron-proton center of mass system.

The ZEUS coordinate system is defined such that the positive  $z$ -axis lies in the direction of the proton beam whereas the positive  $x$ -axis points horizontally towards the center of the HERA ring and  $y$  points upward. The polar angle  $\Theta$  is measured with respect to the positive  $z$ -axis and the azimuthal angle  $\phi$  is measured relative to the positive  $x$ -axis.

A brief description of some detector components is given below, more details are found in [ZEU93d].

### 3.1 ZEUS Components

The central ZEUS detector has a size of  $11.6 \times 10.8 \times 20.0 \text{ m}^3$ , a total weight of 3600 tons and consists of several different components which are optimized for the measurement of specific event quantities. The components as they appear from the inner to the outer are the

- Inner Tracking System (VXD, CTD, TRD, RTD)
- Small Angle Rear Tracking Detector (SRTD)
- Uranium Calorimeter (RCAL, FCAL, BCAL)
- Hadron Electron Separator (HES)
- Beam Pipe Calorimeter (BPC)
- Backing Calorimeter (BAC)
- Forward, Barrel and Rear Muon Detectors (FMUON, BMUON, RMUON)

and some systems not seen in figure 3.1 due to their location far from the nominal interaction region. These components are the

- Luminosity Monitor (LUMI)
- Leading Proton Spectrometer (LPS)

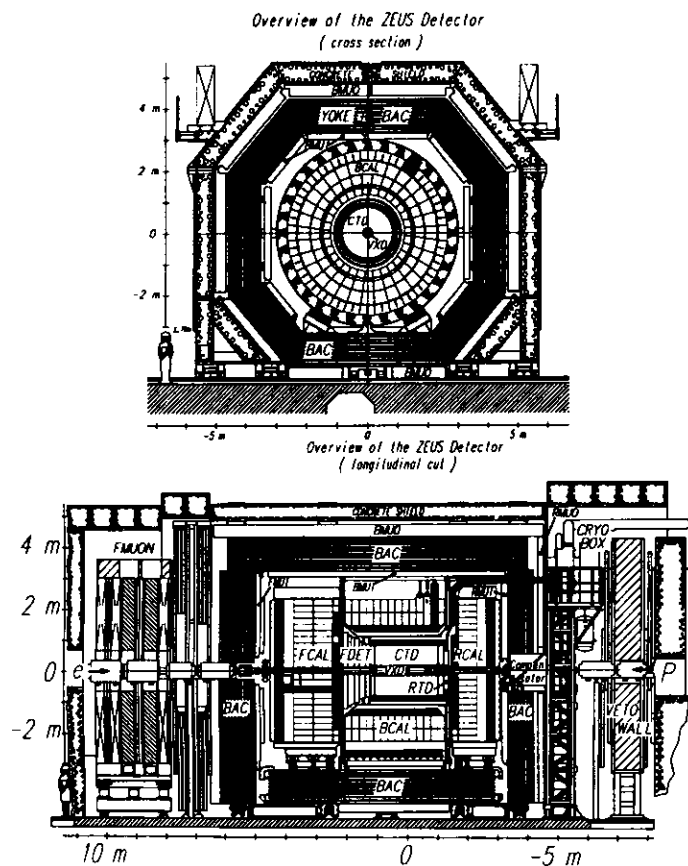


Figure 3.1: Cross section (top) and longitudinal cut (bottom) of the ZEUS detector. A brief description of the components used in this analysis is given in the text.

- Forward Neutron Detector (FNC)
- 44m Tagger

The components used in this analysis are described in more details below and a summary of these detector components and their parameters is given in table 3.1.

### 3.1.1 The Tracking System

The ZEUS tracking system is built out of two cylindrical drift chambers in the central region, the Vertex Detector (VXD) and the Central Tracking Detector (CTD). Three additional plane drift chambers building the Forward Tracking Detector (FTD) extend the tracking region in the forward direction ( $6^\circ < \theta < 28^\circ$ ). The three FTD chambers are separated by 21 cm leaving

space for the Transition Radiation Detector (TRD). The ZEUS tracking system is completed by plane drift chambers in the rear region building the Rear Tracking Detector (RTD). The whole tracking system is enclosed by a superconducting solenoid giving a magnetic field of 1.43 T. During the 1994 data taking the VXD, CTD and RTD were operational whereas the FDET was under construction.

The main task of the VXD [A91a] is the detection of short-lived particles and an improvement of the momentum and angular resolution of charged tracks. The VXD sitting close to the beam pipe is built as a cylindrical drift chamber with an inner radius of 9.9 cm, an outer radius of 15.9 cm and a length of 159 cm. The chamber is filled with Dimethylethan (DME) and contains 6000 wires running parallel to the beam axis. 1440 of these wires are sense wires, organized in 120 cells containing 12 wires each. This chamber yields a position resolution of  $30 \mu\text{m}$ .

The CTD [F94] is another cylindrical drift chamber surrounding the VXD and covering the polar angle region from  $15^\circ < \theta < 164^\circ$  surrounding the interaction region. The chamber is filled with a gas mixture of  $\text{Ar} : \text{CO}_2 : \text{C}_2\text{H}_6$  (90:8:2) and has a length of 240 cm, an inner diameter of 324 mm and an outer diameter of 1648 mm. The CTD is equipped with 24192 wires of which the 4608 sense wires are organized in 576 cells.

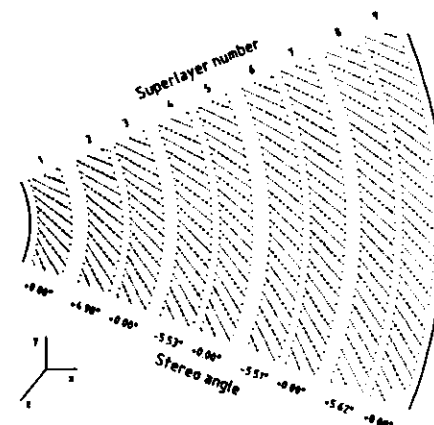


Figure 3.2: Cross section of an octant of the CTD. Further explanations are found in the text.

The organization of the wires is shown in figure 3.2. Nine cylindrical layers called superlayers are built out of cells with eight sense wires each. The wires of the odd numbered superlayers are parallel to the beam, whereas the even numbered ones are tilted by stereo angles up to  $\pm 6^\circ$ . The CTD achieves a spatial resolution of  $100 - 120 \mu\text{m}$  and a momentum resolution of  $\frac{\sigma(p)}{p} = 0.0021 \cdot p \oplus 0.0029$  ( $p$  in  $\text{GeV}/c$ ) at a polar angle of  $90^\circ$ . The resolution in the  $z$ -direction is  $1.0 - 1.4 \text{ mm}$  by stereo angles and less than  $3 \text{ cm}$  by timing.

The RTD is a single planar chamber covering the range of  $160^\circ < \theta < 170^\circ$  in the backward direction. The chamber consists of three layers of drift cells perpendicular to the beam axis and their orientations differing by 60 degree to each other. The single wire resolution is in the range of  $120 - 130 \mu\text{m}$ .

### 3.1.2 The Uranium Calorimeter

The ZEUS calorimeter [A 91b, D91, B93a] is a high resolution uranium scintillator compensating calorimeter. It consists of alternating layers of depleted uranium with a thickness of 3.3 mm and scintillator layers with a thickness of 2.6 mm. The ratio of uranium to scintillator thickness has been chosen in such a way that the calorimeter has an equal response to electrons and hadrons. The calorimeter surrounds the inner tracking system and is mechanically divided into three sections: the forward calorimeter (FCAL) in proton direction, the rear calorimeter (RCAL) in electron direction and the barrel calorimeter (BCAL) surrounding the central region with the solenoid (figure 3.3).

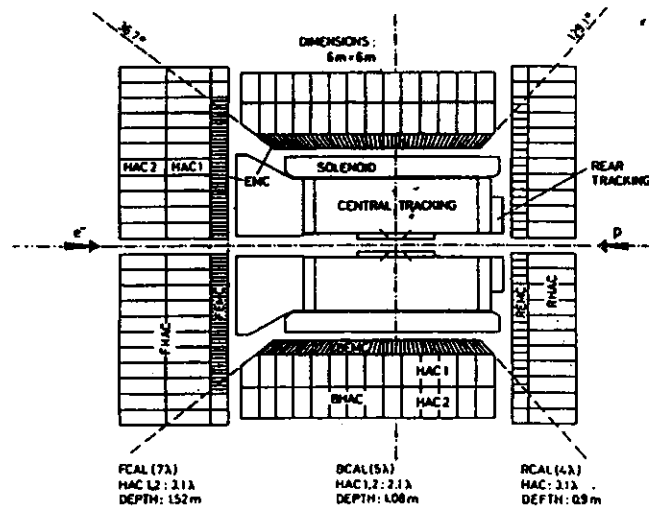


Figure 3.3: Shown are the different calorimeter sections and their division into EMC and HAC cells. Further explanations are given in the text.

Each calorimeter section is built out of modules of which a FCAL module is shown in figure 3.4. These modules are internally subdivided into towers (figure 3.5) with transverse dimensions of  $20 \times 20 \text{ cm}^2$ .

The calorimeter coverage of the total solid angle is 99.7% where the FCAL covers the range of  $2.2^\circ < \theta < 39.9^\circ$ , the BCAL the range of  $36.7^\circ < \theta < 129.1^\circ$  and the RCAL the range of  $128.1^\circ < \theta < 176.5^\circ$ . In the center of the FCAL and RCAL sections an area of  $20 \times 20 \text{ cm}^2$  is left out for the beampipe. The calorimeter is longitudinally segmented into one electromagnetic section (EMC) and one (RCAL) or two (FCAL and BCAL) hadronic sections (HAC). The EMC sections are further subdivided into cells of  $5 \times 20 \text{ cm}^2$  in FCAL and BCAL and cells of  $10 \times 20 \text{ cm}^2$  in the RCAL. The HAC sections are built out of  $20 \times 20 \text{ cm}^2$  cells in all calorimeter regions. Each HAC resp. EMC cell is read out by plastic wavelength shifter plates attached on opposite sides of the cell, lightguides and attached photomultiplier tubes (PMTs).

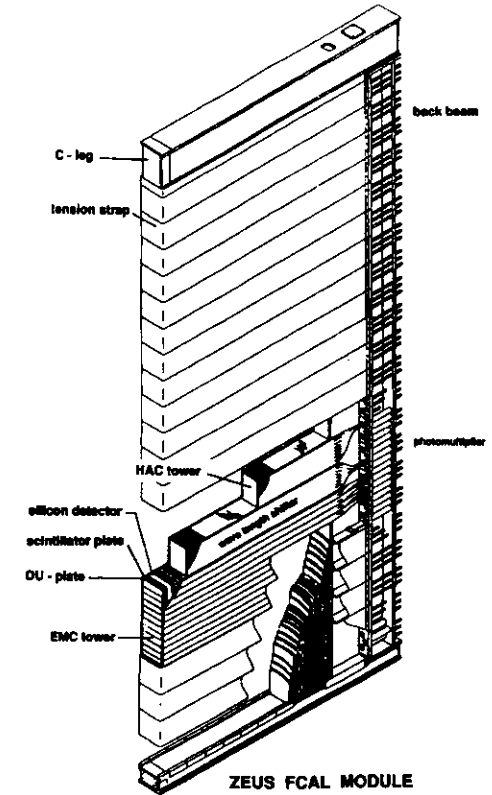


Figure 3.4: View of the largest FCAL module.

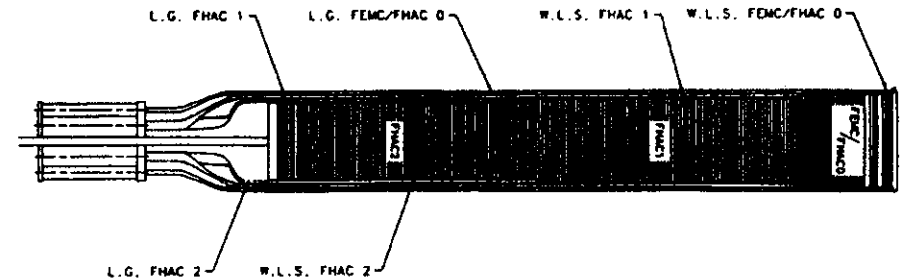


Figure 3.5: Cross section of a FCAL tower. The division into EMC and HAC sections is visible.

Under test beam conditions without dead material in front, the calorimeter has an energy resolution of  $\sigma(E)/E = 18\%/\sqrt{E[\text{GeV}]}$  for electrons and  $\sigma(E)/E = 35\%/\sqrt{E[\text{GeV}]}$  for hadrons.

The timing resolution of a calorimeter cell is less than 1 ns for energy deposits greater than 4.5 GeV.

In order to minimize the effects of noise due to the uranium radio activity on the measurements all EMC (HAC) cells with an energy deposit of less than 60 (110) MeV are discarded from the analysis. For cells with isolated energy deposits this cut was increased to 100 (150) MeV.

### 3.1.3 The Hadron Electron Separator (HES)

In order to improve the discrimination between electrons and hadrons within the calorimeter, gaps have been foreseen in the EMC section of the RCAL at a depth of 3.3 radiation units and in the FCAL EMC section in a depth of 3 and 6 radiation units. These gaps will be equipped with arrays of silicon diodes. During the 1994 data taking period only the RCAL gap was equipped with 10.412 silicon diodes of  $3 \times 3.3 \text{ cm}^2$  transverse size (figure 3.6).

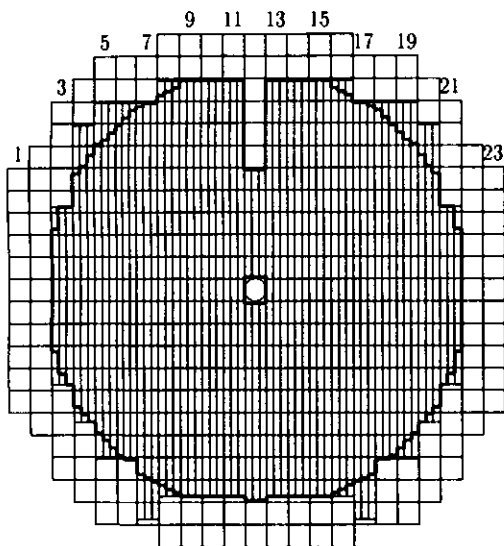


Figure 3.6: This figure shows a view of the RCAL surface as seen from the interaction point. The numbers name the RCAL modules. The squares are the  $20 \times 20 \text{ cm}^2$  RCAL HAC cells. The circular shaped area is equipped with HES diodes in 1994. The thin lines within the modules show the mechanical dimensions of the HES skis.

The diodes are mounted on skis which are up to 4 m long. Three skis are inserted from the top into one RCAL module. Each ski carries 2 columns of up to 113 rows of diodes. The diodes are mounted alternating on the front and rear side of the ski, giving space for parts of

the readout electronics. The rest of the readout electronics is placed outside the calorimeter. The diodes are placed projectively, meaning that the diodes on the rear side of the ski cover the space left out by the front diodes as seen from the interaction point. This results in a wider spacing of the diodes on the rear than on the front side. The gaps in  $x$ -direction between the diodes on one ski are less than 1 mm. Neighboring diodes on different skis are about 3 mm apart, such between different modules about 16 mm. The coverage in  $y$ -direction is complete. The total coverage of the HES plane compared to the RCAL surface is about 84%.

Particles traversing a fully depleted diode produce electron-hole pairs which result in a certain amount of charge seen in the readout electronics. The energy deposited by a minimum ionizing particle is further on referred to as 1 mip.

The separation between hadrons and electrons is based on their different shower behavior in the calorimeter. Electron shower start early in the calorimeter and are narrow, where hadrons tend to interact later and produce wider showers. Thus electron and hadrons can be discriminated by their different amount of signal seen in the HES diodes.

### 3.1.4 The Luminosity Monitor (LUMI)

The luminosity is measured by the luminosity monitor (LUMI) [A 92] detecting Bremsstrahlung photons from the process  $ep \rightarrow e\gamma p$ . This process is used because of its large and precisely known cross section and its well defined experimental signature.

The radiated photon is detected by a lead scintillator calorimeter positioned in electron beam direction at a distance of 107 m from the interaction point. The calorimeter detects photons scattered at angles less than 0.5 mrad and has a resolution of  $\sigma(E)/E = 18.0\%/\sqrt{E[\text{GeV}]}$  under test beam conditions. Under experimental conditions where it is shielded against synchrotron radiation by a carbon-lead filter the energy resolution is  $\sigma(E)/E = 26.5\%/\sqrt{E[\text{GeV}]}$  from Bremsstrahlung data. The position resolution is 0.2 cm in  $x$  and  $y$ .

An additional calorimeter at a position of 35 m detects the electron which is scattered at small angles. The setup of the luminosity monitor is shown in figure 3.7.

### 3.1.5 The Small Angle Rear Tracking Detector (SRTD)

The SRTD consists of two planes of 1 cm wide and 0.5 cm thick scintillator strips which are attached to the front of the RCAL. These planes are arranged in orthogonal directions and cover a region of  $68 \times 68 \text{ cm}^2$  around the beam pipe where a central region of  $20 \times 20 \text{ cm}^2$  is left out for the beam pipe. There is an overlap of the outer SRTD region and the inner RTD region. The SRTD serves as a presampler for the scattered electron in order to correct for energy losses.

The SRTD is able to improve significantly the position reconstruction of the scattered electron and yields a position resolution of 0.3 cm.

The time resolution is better than 2 ns for a minimum ionizing particle.

## 3.2 Data Acquisition System Overview

The HERA bunch crossing interval of 96 ns corresponds to a bunch crossing rate of 10 MHz and the total number of 250.000 ZEUS readout channels with a raw data information of 500 kBytes per event lead to hard requirements on the ZEUS trigger and readout system. The ZEUS data acquisition and trigger system has to fulfill the task of reducing the raw input data stream of

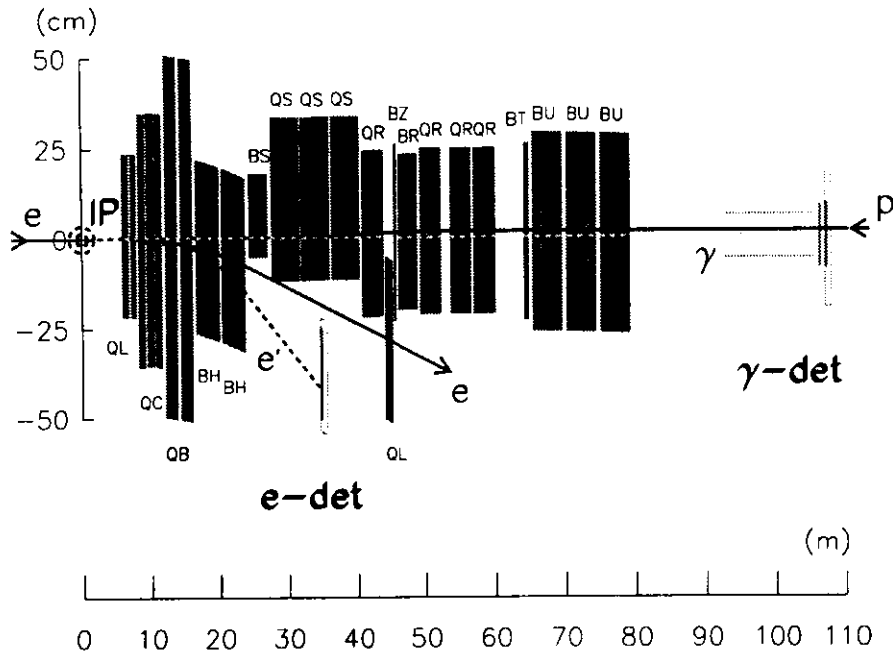


Figure 3.7: The ZEUS luminosity monitor. The  $\gamma$ -calorimeter ( $\gamma$ -det) tags Bremsstrahlung photons  $\gamma$  from the process  $ep \rightarrow e\gamma$ , the electron calorimeter (e-det) tags photoproduced electrons  $e'$ . B and Q label quadrupole and bending magnets of HERA. The solid lines show the nominal  $e$  and  $p$  orbits.

5 TBytes/s to about 1 MBytes/s without rejecting too many important physics events. The layout of this distributed and highly parallel real time system is shown in figure 3.8. It consists of several independent component readout systems and a three level trigger system. The DAQ systems operation is briefly described below.

### 3.2.1 The Trigger System

For data recording the trigger system has to reduce the raw data rate by a factor of  $10^6$  which is done in three steps.

#### First Level Trigger (FLT)

The FLT has to reduce the data rate to less than 1 kHz by eliminating beam gas background. Dedicated logic in combination with many programmable parameters is used for this purpose.

At each bunch crossing the HERA clock triggers the ZEUS readout system and during a time gate of a few nanoseconds the independently operating detector components are read out. The readout is performed by a so called component subsystem unique to each component which contains the frontend electronics required for control and readout.

<b>Vertex Detector (VXD)</b>			
radius	99	159	mm
length		1590	mm
polar angle coverage		$8.6^\circ - 165^\circ$	
position resolution		30	$\mu\text{m}$
<b>Central Tracking Detector (CTD)</b>			
radius	324	1648	mm
length		2400	mm
polar angle coverage		$15^\circ - 164^\circ$	
position resolution		100	120 $\mu\text{m}$
$z$ resolution (stereo)		1.0	1.4 mm
$z$ resolution (timing)		< 3	cm
$\sigma(p)/p$ at $90^\circ$		$0.0021p [\text{GeV}/c^{-1}] \oplus 0.0029$	
<b>Forward/Rear Tracking Detectors (FTD1-3,RTD)</b>			
active radius	(FTD)	180-1085	mm
	(RTD)	220-495	mm
polar angle coverage	(FTD)	$6^\circ - 28^\circ$	
	(RTD)	$160^\circ - 170^\circ$	
position resolution		120	130 $\mu\text{m}$
<b>Superconducting Solenoid (COIL)</b>			
$B$ field		1.43	T
<b>High-Resolution Calorimeter (CAL)</b>			
maximum depth	(FCAL)	1525 (7.1)	mm ( $\lambda_0$ )
	(BCAL)	1059 (4.9)	mm ( $\lambda_0$ )
	(RCAL)	870 (4.0)	mm ( $\lambda_0$ )
polar angle coverage	(FCAL)	$2.2^\circ - 39.9^\circ$	
	(BCAL)	$36.7^\circ - 129.1^\circ$	
	(RCAL)	$128.1^\circ - 176.5^\circ$	
relative energy resolution (hadrons)		$35/\sqrt{E [\text{GeV}]} \oplus 2$	%
relative energy resolution (electrons)		$18/\sqrt{E [\text{GeV}]} \oplus 1$	%
time resolution		$1.5/\sqrt{E [\text{GeV}]} \oplus 0.5$	ns
$x$ -position resolution (hadrons)		$6.5/\sqrt{E [\text{GeV}]}$	cm
$y$ -position resolution (hadrons)		$6.7/\sqrt{E [\text{GeV}]}$	cm
$x$ -position resolution (electrons)		$5.4/\sqrt{E [\text{GeV}]}$	cm
$y$ -position resolution (electrons)		$1.4/\sqrt{E [\text{GeV}]}$	cm
<b>Small Angle Rear Tracking Detector (SRTD)</b>			
position resolution		0.3	cm
timing resolution		< 2	ns

Table 3.1: Selected parameters of ZEUS components used in this analysis.

The data read out by a component subsystem is stored in a  $5\mu\text{s}$  deep 10.4 MHz pipeline and analyzed by a local first level trigger within the next 26 clock cycles. As the internal FLT trigger calculations are completed the information for a particular bunch crossing is passed to the global first level trigger (GFLT) which performs a first overall evaluation. The GFLT

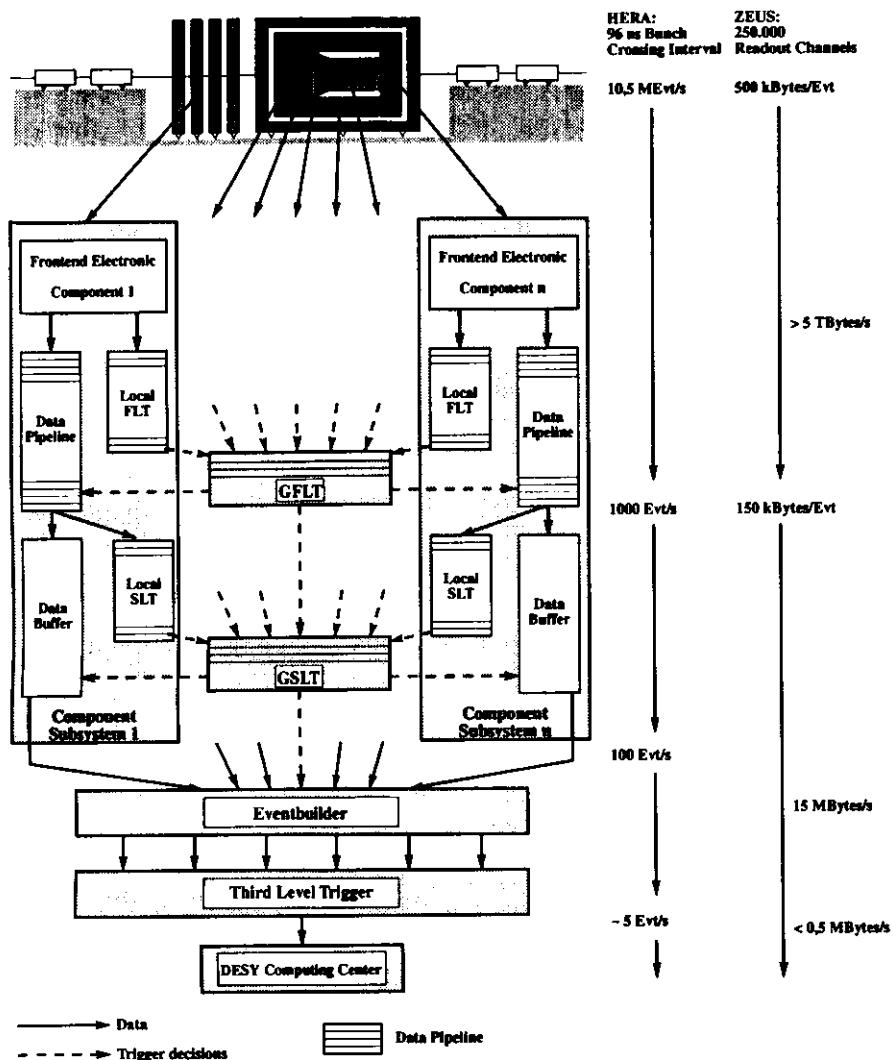


Figure 3.8: Layout of the ZEUS trigger and data acquisition system. Its operation is briefly described in the text.

calculations take additional 20 bunch crossing ( $1.9 \mu\text{s}$ ) and the overall decision is issued exactly 16 crossings ( $4.1 \mu\text{s}$ ) after the bunch interaction that produced it.

The design rate of accepted events is up to 1 kHz. The decision of the GFLT is sent back to the component subsystems and on rejection the event is cleaned from the pipeline. Otherwise

the data is handed over to the second level trigger (SLT). Up to this stage the readout system is dead time free.

### Second Level Trigger (SLT)

Data accepted for further analysis from the GFLT is transferred to a second level trigger pipeline which is still local to the single component subsystem. A GFLT accept rate of 1 kHz and a 'copy time' of  $30 \mu\text{s}$  from the FLT to the SLT pipeline results in 3% deadtime if no further blocking of the system occurs. A local second level trigger operates on the obtained data and forwards his decision to a global second level trigger which computes an overall GSLT decision.

The GSLT is based on transputer hardware in a VME environment and the GFLT output rate is reduced to 100 Hz.

### Eventbuilder (EVB)

The component data accepted by the GSLT is given a 'GSLT decision number' and transferred to the Eventbuilder. The Eventbuilder is implemented as an asynchronous real-time parallel packet-switching transputer network [BHV93].

The Eventbuilder merges the data obtained from the single detector components into a single data structure, the so called event. Since the EVB is connected to all detector components, it is an excellent monitoring device for the data acquisition system [Sch92]. Based on this information an expert system which will be explained in more details in section 3.2.2 has been proposed [BFH92] and implemented [Ohr93, BFHO94].

### Third Level Trigger (TLT)

The data structure from the EVB is handed over to the third level trigger (TLT), a farm of 36 workstations where a single event is analyzed by an individual workstation. At this stage the full event information is available for the first time and a version of the offline event reconstruction code is running. Based on these results a final filtering is done and the TLT output rate of about 5 events/s is written to magnetic tape for offline analysis.

### Reconstruction and Offline Analysis

Once the event is stored on tape, the complete reconstruction of the event is done later on offline. Here the full reconstruction code and calibration of each component is available and the raw data output as written to tape is reduced to a subset of physical values which are then stored in a reduced data structure, the so called MiniDST. During the offline reconstruction each event is assigned with DST bits which are set as special selection cuts of the various physics groups are fulfilled.

## 3.2.2 The ZEUS Expert System (ZEX)

Based on the monitoring information of the Eventbuilder which has been shown to be helpful during the installation of the ZEUS DAQ system, an expert system for automatic evaluation of the monitoring data has been proposed [BFH92] and a first prototype was implemented and installed in 1993 [Ohr93, BFHO94]. After the successful installation, the scope of the system has been extended to other aspects [BFH96]. A brief review of the existing system and its implementation is given in the following paragraphs.

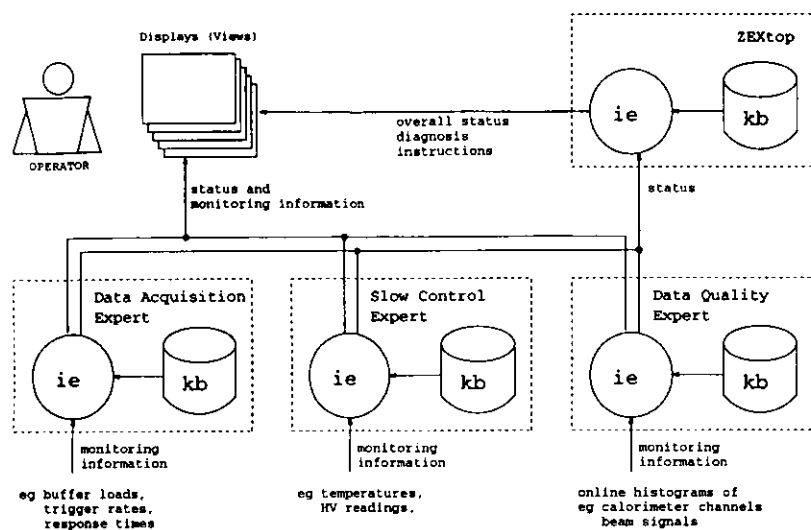


Figure 3.9: Architecture of the ZEUS Expert System, ZEX (ie: inference engine, kb: knowledge base).

The nature of the ZEUS collaboration required components of the online system to be constructed independently at different places. Thus, expert knowledge about the system is split among several institutes. While during the first years of operation experts from most institutes have been on location, the successfully operating experiment saw already many experts returning to their home institutes, thus being no longer available at short notice.

Due to the complexity of the online system, training of new experts is a long and tedious procedure. On the other hand, many of the tasks which are performed by the shift crew can be handled automatically, like equipment monitoring, or surveillance of data rates. The ZEUS collaboration has therefore decided to launch an expert system project to support operation of the experiment.

The aim of ZEX is to store the knowledge of the different experts in the experiment control system and make it available to anybody, whenever and wherever it is needed. This way, it is hoped to increase both efficiency and reliability of experiment operation, while at the same time the required efforts and expertise (and thus the required manpower) of the shift crew are reduced.

ZEX is designed to automatically detect anomalous behavior in various parts of the experiment, to trace errors back to their origin, and to help to recover the system as quickly as possible by providing adequate instructions for the operators.

### ZEX-P, a Prototype Expert System

In a first step, an expert system prototype (ZEX-P) was created which processed monitoring information from a subsystem of the online data-acquisition system, the Eventbuilder. The

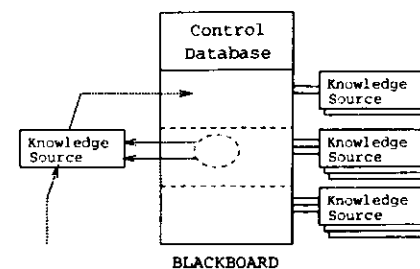


Figure 3.10: Blackboard architecture scheme (explanation in the text).

prototype was designed using SA/SD-methods, and was implemented in the programming language C.

ZEX-P was based on standard syntactic pattern-recognition algorithms (nearest cluster center method, Finite State Machines (FSMs), etc.). Experience regarding feasibility and performance was encouraging, however expanding the scope of ZEX-P rapidly led to state explosion in the FSMs, and it became clear that keeping the expert system maintainable would require dedicated programming languages and development tools. Therefore it was decided to re-engineer and implement ZEX-P in a rule-based approach, based on the commercial expert-system shell RTworks.

### ZEX Architecture and Implementation

Figure 3.9 shows the architecture of ZEX. The structure of ZEX was chosen to reflect the structure of the online system. Three dedicated sub-expert systems will evaluate and thus encapsulate knowledge of distinct domains, while a top-level module analyzes the output of the sub-expert systems to derive the overall system characteristics.

The slow control sub-expert system monitors and displays the basic hardware of the experiment. It surveys the states of power supplies, racks, crates, photomultipliers, temperature and radiation sensors, cooling, etc. Based on this information, it decides whether efficient data taking is possible, and proposes what to do to regain an acceptable state.

The task of the data quality sub-expert system will be to ensure high quality of the data written on tape. It has to monitor the quality of the colliding electron and proton beams, observes background rates, and checks the data from the major components for miscalibration or dead channels. This has to be done by comparing specific online monitoring histograms against given reference histograms.

The data acquisition expert system has to survey the data taking. It will monitor the central components of the data acquisition system (i.e. front-end systems, trigger stages, data storage systems) for data rates, deadtime or response times.

At the top level, ZEX will combine the information about the subsystems to an overall system understanding and select the most important information to present it to the shift crew.

The design of the internal ZEX architecture is based on the Blackboard approach. Within this approach several modules communicate through a global multi-dimensional data structure

called blackboard (figure 3.10). The blackboard is hierarchically organized into information levels, corresponding to different levels of data processing, which range from raw monitoring information to derived system status information.

The problem-solving knowledge is modularized and encapsulated in independent, hierarchical organized and so-called Knowledge Sources<sup>1</sup> (KS) which contain problem solving knowledge and are running under a controller. This is a special KS containing control knowledge, i. e. knowledge allowing the system to determine the focus of attention while reasoning, schedule the access of the KSs to the Blackboard, etc.

The Knowledge Sources are activated through the blackboard or by external inputs. Currently, the Knowledge Sources are implemented as rules, however the Blackboard architecture allows to incorporate other paradigms of knowledge processing, for example some of the pattern recognizers which have been developed for ZEX-P.

The status of the experiment is displayed in a set of hierarchically organized displays. At the top level, the different characteristics of the experiment are represented by "traffic-lights". The lights are flashing whenever a change of state has occurred in the corresponding item. ZEX selects the most relevant items and describes them in a text window. The mouse-and-click interface allows the operators to select individual status displays for the various characteristics of the experiment to obtain more detailed status information.

### Status and Experience

ZEX-P was operating reliably during the 1993 data taking period. The real-time requirements were met but because of the limited scope of the system ZEX-P was not a real breakthrough in supporting the online operator.

The implementation via finite state machines in a real time expert system turned out to be reliable and fast, but as the addition of knowledge usually results in a multiplication of system states, the FSMs are difficult to expand and can be modified by trained experts only. As the knowledge about a high energy physics detector and its behavior is permanently growing and changing, this requires to give highest priority to maintainability of the knowledge base. The knowledge has to be decoded in an easily readable and expandable way. Unfortunately, finite state machine systems do not fulfill this requirement. Therefore it was decided to switch to a rule based system for further development of ZEX. The commercial expert system shell RTworks was seen as a tool to fulfill these requirements to a high degree.

In a first installation most of the ZEX-P functionality and thus a first part of the data acquisition expert system has been reimplemented.

The slow-control expert system was the first complete sub-expert system to be put into operation during the 1994 data taking period. More than 1300 rules were needed to cover the knowledge about the basic hardware of the experiment. The expert system informs the operator about the overall status, it provides an explanation of the most severe problems and their impact and proposes actions for the operator to take. For detailed diagnosis the operator is guided through hierarchically layered, point-and-click color graphics views. For the 1995 data taking period, ZEX was tuned to speed up the procedure of expanding and modifying the knowledge of the system, thus enabling fast reactions to changes in the run conditions.

Currently the monitoring of the FLT trigger rates as an extension to the data acquisition expert system and first parts of the data quality sub-expert system for online histogram checking

<sup>1</sup>The Knowledge Sources have to be differentiated from the knowledge bases shown in figure 3.9 as the knowledge base for a sub-expert system is build out of several, hierarchically ordered Knowledge Sources.

are under development. In its current version, ZEX incorporates about 100 Knowledge Sources, a total of about 2000 rules and more than 270 various displays organized in a tree-like structure.

Development of ZEX started after the experiment was put into operation, hence ZEX had to be put on top of existing systems. The major constraint for the development of ZEX was to not interfere with the operation of the online system. This turned out to introduce lots of difficulties since very often information which is essential for an accurate reasoning has not been accessible to ZEX.

As ZEX is an add-on to the online system, most of its input consists of monitoring data and messages which are acquired and pre-processed outside the expert system. Thus it has become a major task to ensure that this pre-processed information is reliably representing the data ZEX is expecting, preventing ZEX from inheriting any unwanted features from those external systems.

## Chapter 4

### Electron Identification

An important part in the DIS event reconstruction is the identification of the scattered electron. For this purpose several different algorithms have been developed within the ZEUS collaboration.

#### 4.1 Electron Finder

Most of the electron finding algorithms are based entirely on the calorimeter information. The first step consists in combining calorimeter cells (for the definition of a cell refer to section 3.1.2) with an energy above a certain threshold to more complex objects. This clustering can be done in several different ways. The most commonly used algorithms are based on condensates, cones and islands.

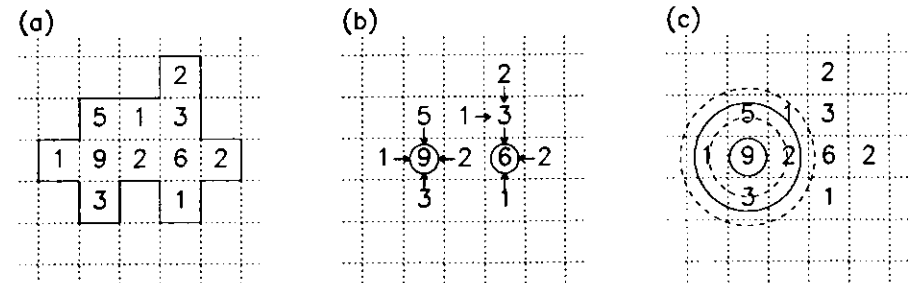


Figure 4.1: Creation of calorimeter objects via different algorithms: condensates (a), islands (b) and cones (c). The boxes schematically represent calorimeter cells, while the numbers represent energy deposits. The darker line shows the contour of the cells assigned to the object for the different algorithms available. Note that the island algorithm has found two objects.

Condensates are built out of adjacent cells with energy above a given energy threshold where cells are called adjacent if they share one side (figure 4.1a). The electron candidate is then selected out of these objects by computing the number and types of cells contributing to the condensate and from the fraction of electromagnetic and total energy. If more than one condensate is found to potentially originate from an electron, physics arguments are used to pick up the most probable electron candidate.

The cone algorithm maps the calorimeter cells onto a sphere and initiates its search by considering all cells with an EMC energy deposition exceeding a given limit. These cells are then defined as seed cells. If there is more than one of these cells within a certain opening angle ( $12^\circ$ ) only the highest energetic is considered as a seed cell. In the next step the electromagnetic and hadronic energy ratios are calculated for all cells within certain opening angles (cones) surrounding the seed (figure 4.1c) and a probability for the seed being due to an electron is calculated. The electron finders ELEC5 [Rep92] which uses cones of  $5^\circ$  and  $17.2^\circ$  for EMC and  $12.5^\circ$  and  $22.9^\circ$  for HAC cells and a modified version with an improved quality of the selected electron EEXOTIC [CR92] are based on this clustering algorithm.

The ISLAND algorithm [Wai93] assigns a vector to each cell pointing to its highest-energetic neighbor with more energy than the cell itself (figure 4.1b). If there is no adjacent cell with more energy deposition, the initial cell becomes a seed for an island, meaning that the vector points to itself. All vectors leading to the same seed are then merged into one object called island.

The electron finder SINISTRA [ACS95] is a neural net based algorithm which operates on the objects obtained by an island algorithm. An updated SINISTRA version (SINISTRA95) [ASV96] which will be used in this analysis became available in spring 1996 and uses a different representation of the calorimeter cells within the neural net, making the finder more efficient at low electron energies and independent of the calorimeter geometry<sup>1</sup>.

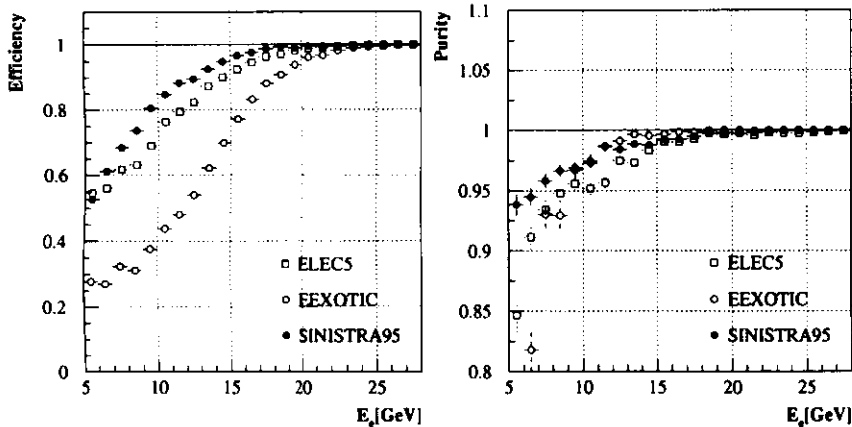


Figure 1.2: Efficiency (left) and purity (right) for different calorimeter based electron finders as a function of the electron energy  $E_e$  in DIS Monte Carlo events. For SINISTRA95 a probability cut of  $P_{Si} > 0.9$  was used.

<sup>1</sup> This became necessary for the 1995 data taking due to the shift of the middle ZEUS RCAL modules. These modules have been moved by 4 cm towards the beampipe, reducing the beampipe hole in  $y$  direction to 12cm and thus increasing the acceptance for low  $Q^2$  events.

The different finders are evaluated by MC methods, giving their efficiency  $\epsilon$  defined as the number of real electrons (found and correctly identified) divided by the number of electrons generated

$$\epsilon = \frac{\text{number of real electrons found}}{\text{number of electrons generated}} \quad (4.1)$$

and the purity  $\pi$  which is given as the ratio of the number of real electrons and the number of particles identified as electrons

$$\pi = \frac{\text{number of real electrons found}}{\text{number of particles identified as electrons}} \quad (4.2)$$

Currently the most widely used finder in the ZEUS collaboration is SINISTRA since it gives the best efficiency/purity ratio (figure 4.2). The performance of SINISTRA is influenced by a probability cut on the electron candidate found by the neural net. A cut of  $P_{Si} > 0.9$  is usually used for DIS analysis.

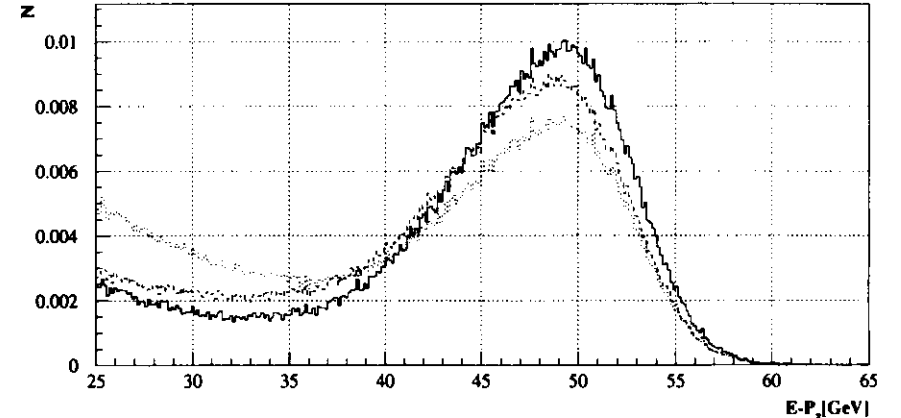


Figure 4.3:  $E - P_z$  distribution of data events with DST bit 11 (see section 5.3.1) and an identified electron by different electron finders. SINISTRA (solid line) shows the lowest photoproduction background at  $E - P_z < 35$  GeV whereas EEXOTIC (dashed line) picks up more background but even less than ELEC5 (dotted line). The distributions are normalized to one. Further explanations are given in the text.

The excellent performance of the neural net is seen in the  $E - P_z$  distribution (figure 4.3) of events with an identified electron. The value  $\delta = E - P_z$  of an event is derived from energy and longitudinal momentum conservation and yields

$$\delta = \sum_i E_i - P_{z,i} \cong 2 \cdot E_{beam,e} \quad (4.3)$$

where the sum runs over all final state particles  $i$  including the scattered electron.

This relation is obtained from the 4-momenta of the initial electron and the final state hadrons

$$k_e = (E_{beam,e}, 0, 0, E_{beam,e}), \quad k'_e = (E_e, P_{x,e}, P_{y,e}, P_{z,e}), \quad (4.4)$$

$$p_h = (E_{beam,p}, 0, 0, E_{beam,p}), \quad p'_h = (E_h, P_{x,h}, P_{y,h}, P_{z,h}). \quad (4.5)$$

Neglecting initial state radiation this leads to

$$E_{beam,p} + E_{beam,e} = E_e + \sum_h E_h \quad (4.6)$$

for the energy conservation equation and

$$E_{beam,p} - E_{beam,e} = P_{z,e} + \sum_h P_{z,h} \quad (4.7)$$

for the longitudinal momentum conservation equation where the sums run over all final state hadrons. Combining equations 4.6 and 4.7 finally leads to the expression given in equation 4.3. Compared to the other electron finders the tail in the  $\delta$ -distribution at  $\delta < 35$  GeV is smallest for the SINISTRA finder. Since DIS events are showing up close to twice the electron beam energy and photoproduction events at  $E - P_z \approx 0$  GeV, the reduced tail shows that SINISTRA with a probability cut  $P_{Si} > 0.9$  selects very clean DIS electrons and rejects most of the events originating from photoproduction.

## 4.2 Electron Reconstruction with the HES

A calorimeter independent electron identification algorithm based on the information of the Hadron Electron Separator (HES) was first introduced by I. Fleck and is described in detail in his PhD thesis [Fle94] and a ZEUS note [FO95]. The most important aspects are repeated here.

### 4.2.1 Object Characteristics

The characteristics of HES signals originating from electrons are analyzed on a sample of nearly pure electrons. This sample was selected from the data taken in 1994 by requiring DST Bit 11<sup>2</sup> and an electron which is identified by three calorimeter based algorithms (EEXOTIC, ELECS and SINISTRA with  $P_{Si} > 0.9$ ). The HES electron candidates which are considered further on are selected by the algorithm described in section 4.2.3.

The measurement of the energy deposit by electrons in the HES requires the summation over a certain number of HES diodes. Figure 4.4 shows the ratios of the energy deposit for sums over 1, 3×3, and 5×5 diodes where the diode with the highest energy deposit is located in the center of the diode cluster. Only those diodes are included in the sum that have a minimum energy deposit of 0.6 mip which gets rid of most of the noise signals.

The righthand plot in figure 4.4 shows that on average about half of the total energy is deposited in the central diode; in the most probable case about 80% of the shower energy is contained in the central diode. The Molière radius is approximately 2 cm and therefore

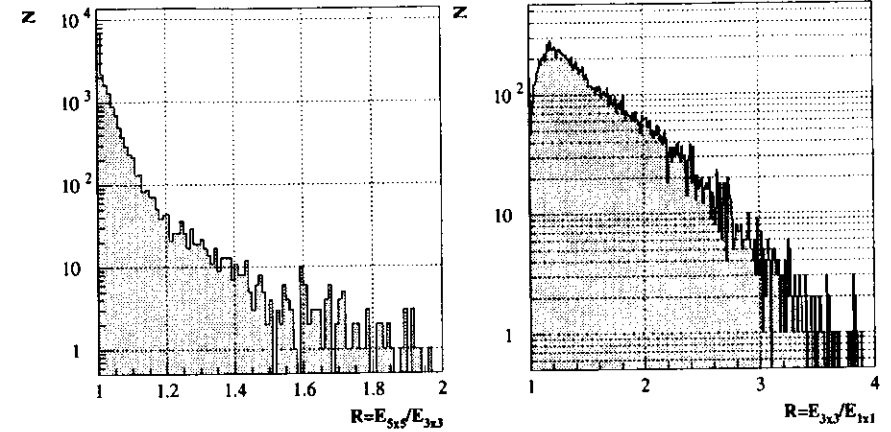


Figure 4.4: The lefthand plot shows the energy ratio  $R = E_{5 \times 5} / E_{3 \times 3}$  for identified electrons where  $E_{5 \times 5}$  and  $E_{3 \times 3}$  are the energy sums of a 5×5 and a 3×3 diode field respectively. The righthand plot shows the energy ratio of a 3×3 diode field to the energy deposit in the central diode. The array of 5×5 diodes contains on average 4% more energy than the array of 3×3 diodes. The array of 3×3 diodes contains on average 43% more energy than the central diode.

smaller than the dimension of a HES diode with  $3.0 \times 3.3$  cm<sup>2</sup> and most of the shower should be contained in a single diode. Since the shower could hit the diode at the edge or even corner and share the energy on neighboring diodes, using only the central diode to determine the energy deposit will not be satisfactory. Using 3×3 diodes is sufficient as can be seen in the lefthand plot of figure 4.4. On average 96% of the total energy deposit is contained in the 3×3 diode field. Using 5×5 diodes performs slightly better for isolated electrons but for two particles close together the larger field might pick up entries from different particles and therefore gives a worse estimate than using only 3×3 diodes. As a result a field of 3×3 diodes will be used to measure the energy deposit  $E_{HES}$  of an electron in the HES.

Figure 4.5 shows the correlation between the deposited energy in the HES and the energy of the corresponding calorimeter island  $E_{RCAL}$ . The island energy is obtained by building all island objects in the calorimeter and then choosing the island which is closest to the HES object within a radius of 20 cm. In the energy range from 5 to 24 GeV there is a linear correlation but for electron energies above 24 GeV the energy deposit in the HES decreases again which is a subtle consequence of the inactive material in front of the calorimeter.

Due to the inactive material the kinematic peak in the electron spectrum is shifted from 27.5 GeV to 24 GeV (see section 5.1). All electrons inside the shifted kinematic peak have already started to shower before they reach the calorimeter. Electrons which have not yet started to shower in the inactive material deposit a higher energy in the calorimeter. These high energetic electrons are probed by the HES at an early stage of the shower and deposit

<sup>2</sup>A detailed description of DST selection bit 11 is given in section 5.3.1.

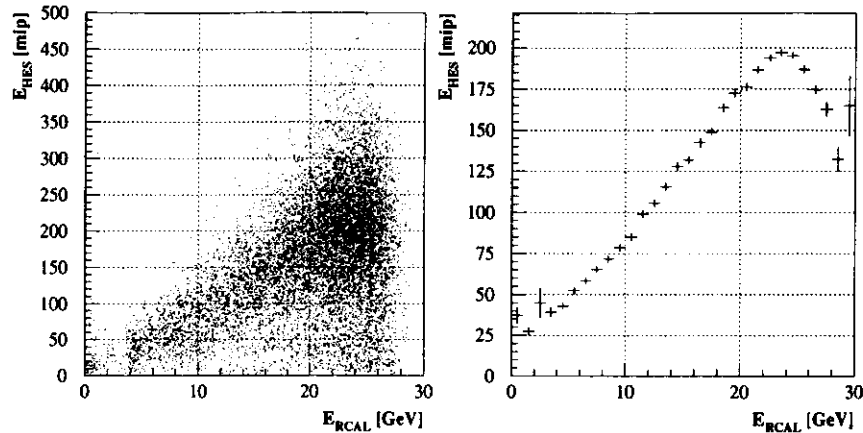


Figure 4.5: Energy deposit in the HES versus the energy measured by the calorimeter. The lefthand plot shows a scatter plot, while the righthand one shows the average energy deposit in the HES versus the energy deposit in the RCAL. The dip at  $E_{RCAL} > 24$  GeV can be explained by the dead material in front of the calorimeter modules (see text).

therefore less energy in the HES than the electrons from the kinematic peak, which are probed closer to the shower maximum.

The size of a shower at the depth of the HES can be determined by counting the number of diodes with an energy deposit greater than 0.6 mip within the  $3 \times 3$  diode field. Figure 4.6 shows this number of diodes versus the energy measured in the calorimeter and the energy measured with HES. In the lefthand plot of figure 4.6 a rise can be seen for the energy range from 5 to 24 GeV and the same decrease for higher energies as in figure 4.5. The righthand plot in figure 4.6 shows a continuous rise of the number of diodes as the total energy in HES increases which shows that the transverse size of the shower grows as the deposited energy increases.

## 4.2.2 Position Reconstruction

The HES can be used to reconstruct the position of a particle hitting the RCAL. Due to the small mechanical dimension of a diode this can be done with relatively high precision. But there is a significant difference for hadrons and electrons.

Hadrons usually show an energy deposit in one diode only. As there is no way to tell from the energy deposit in the diode where the particle has hit the diode, the position resolution for hadrons is therefore given by the mechanical dimensions. Due to the gaps in the coverage of the calorimeter modules and additional small gaps between the diodes in one module, 16% of the total RCAL area is not covered by the active area of the diodes. Hadrons going through these gaps do not show any signal in the HES.

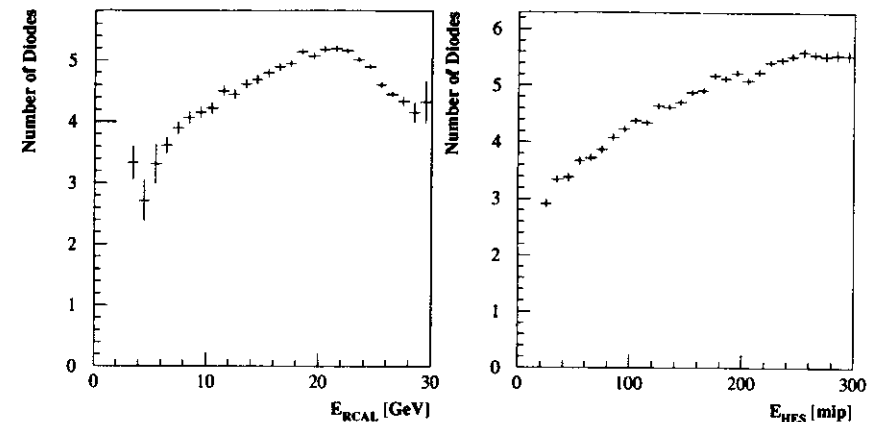


Figure 4.6: Average number of diode hits in a  $3 \times 3$  diode array as a function of the energy deposit in the rear calorimeter  $E_{RCAL}$  (left) and the energy deposit in HES  $E_{HES}$  (right). The dip at high energies in the lefthand plot can be explained by the dead material in front of the calorimeter modules (compare figure 4.5).

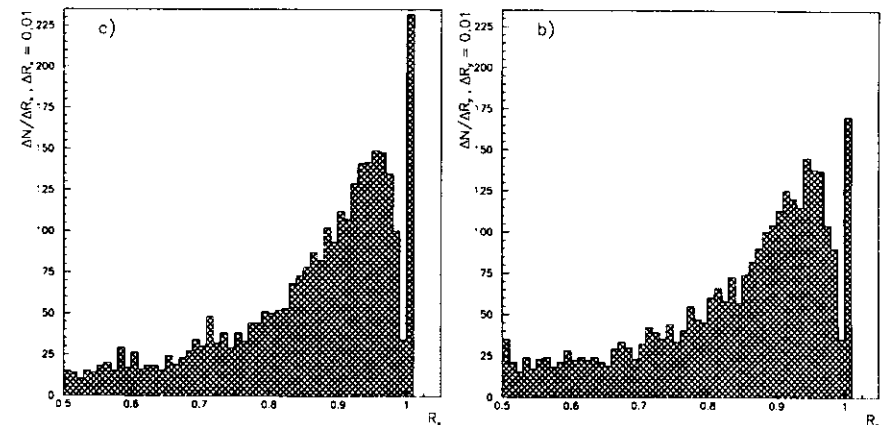


Figure 4.7: Distribution of the a) horizontal ( $x$ ) and b) vertical ( $y$ ) energy ratios  $R_x$  and  $R_y$  in the ZEUS experiment,  $R = E_1/(E_1 + E_2)$ .  $E_1$  is the energy of the diode with the highest energy deposit and  $E_2$  the energy of that horizontal (vertical) neighbor, which shows the next higher energy deposit. (from [FO95])

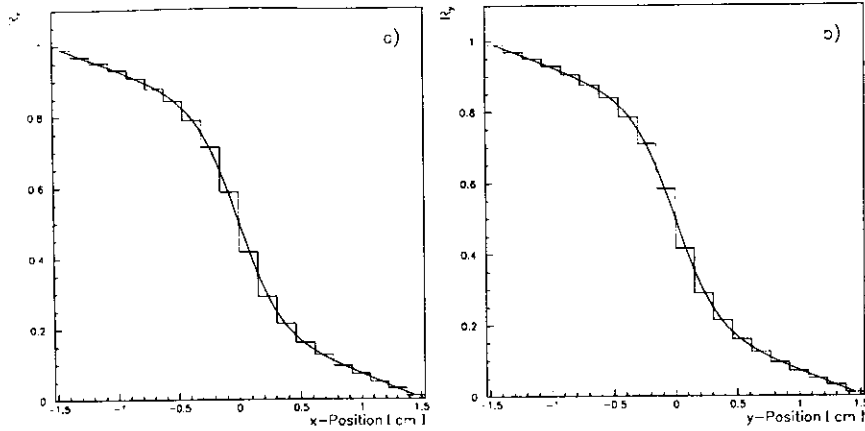


Figure 4.8: Fit to the distribution of the energy ratio  $R$  as a function of the position in  $x$  or  $y$  relative to the middle between two neighboring diodes. The area  $|x| < 0.69$  cm ( $|y| < 0.69$  cm) was fitted by a form  $\tanh(x)$  or  $\tanh(y)$  while for the outer area ( $|x| > 0.69$  cm,  $|y| > 0.69$  cm) a linear fit was used. The gap between the two diodes is positioned at  $x = 0$  or  $y = 0$ . (from [FO95])

For electrons a much better position resolution can be achieved, as the HES is situated near the shower maximum. Therefore, in most cases more than one diode shows a signal.

Figure 4.7 shows the distribution of the energy ratio  $R$

$$R = \frac{E_1}{E_1 + E_2} \quad (4.8)$$

as seen in the ZEUS experiment.  $E_1$  is the energy of the diode with the highest energy deposit and  $E_2$  the energy of that one of the two neighbors in horizontal ( $x$ ) or vertical direction ( $y$ ) which has the next higher energy fraction. Therefore  $R$  will be always between 0.5 and 1.0. The slight difference between the distributions in  $x$  and  $y$  can be explained by the bigger gaps in  $x$ -direction. This results in energy losses and, consequently, in less energy in the neighboring diodes.

As a relation between  $R$  and the horizontal position  $x$  (resp.  $y$ ) an Ansatz

$$R_x = 0.5 - \tanh\left(\frac{x}{x_0}\right) \quad (4.9)$$

is taken. Assuming that the electrons in ZEUS are equally distributed over the distance of two diodes equation 4.9 is used on the distribution shown in figure 4.7 and results in figure 4.8. Equation 4.9 itself already gives a good parameterization. Using the combination of the  $\tanh$  and a linear fit, an improved result can be achieved. The used functions are listed in table 4.1.

To check the reconstructed position a comparison with the position measurement in the calorimeter and the SRTD was made. For the calorimeter the routine ELECPO [Doe95] whereas for the SRTD the routine SRTDELEC from the SRTD reconstruction code [NV95] was used. The difference in the reconstructed electron position between CAL and HES is shown in the upper plots of figure 4.9 and between SRTD and HES in the lower plots of figure 4.9. The

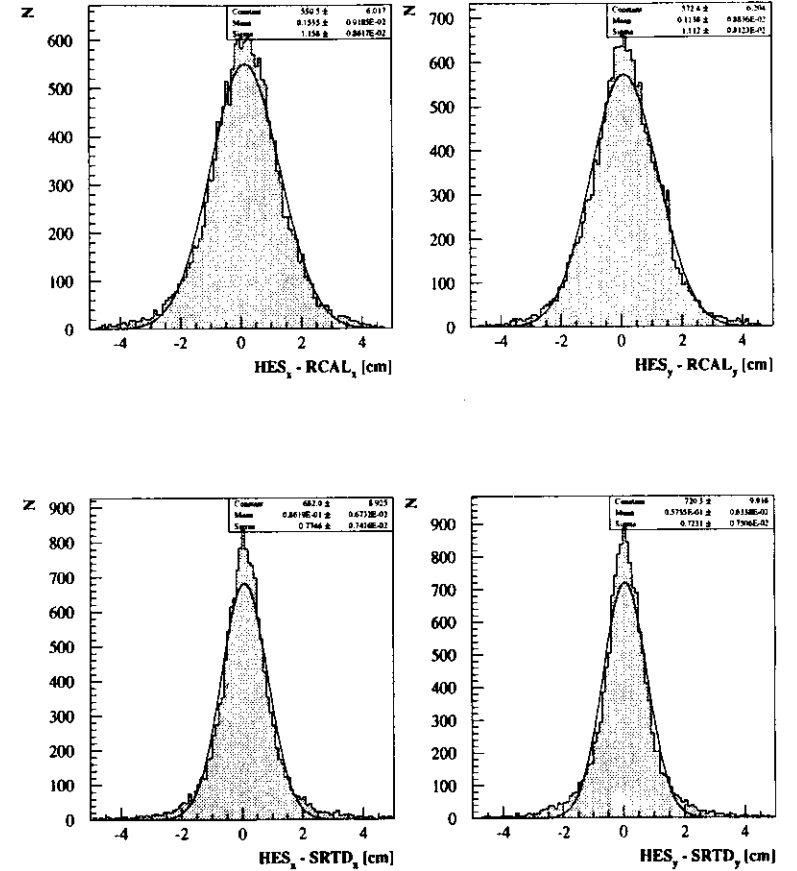


Figure 4.9: Distribution of the difference in the reconstructed electron position between HES and CAL (upper plots) and between HES and SRTD (lower plots). The left plots show the difference in  $x$ ; the right diagrams show the difference in  $y$ . All distributions have been fitted with a Gaussian. The mean value of the Gaussian fit to the HES-CAL difference is 1.6 mm for  $x$  and 1.1 mm for  $y$ . The RMS of the fits in  $x$  and  $y$  is 11.2 mm and 10.9 mm respectively. The mean value of the Gaussian fit to the HES-SRTD difference is 0.9 mm for  $x$  and 0.6 mm for  $y$ . The RMS of the fits in  $x$  and  $y$  is 7.6 mm and 7.2 mm respectively.

	function	range
$R_x$	$-0.39 \cdot \tanh(2.49 \cdot x) + 0.50$	$ x  < 0.69$
	$-0.15 \cdot x + 0.77$	$ x  > 0.69$
$R_y$	$-0.43 \cdot \tanh(1.34 \cdot y) + 0.50$	$ y  < 0.69$
	$-0.16 \cdot y + 0.75$	$ y  > 0.69$

Table 4.1: Functions used for the energy ratios  $R_x$  and  $R_y$  as a function of  $x$  and  $y$  respectively. The valid range is measured from the gap between the two diodes and is inside the diode with the next higher energy deposit. Numbers are in cm.

	$\sigma_x$ [mm]	$\sigma_y$ [mm]	$mean_x$ [mm]	$mean_y$ [mm]
HES - CAL	$11.21 \pm 0.08$	$10.87 \pm 0.07$	$1.59 \pm 0.09$	$1.15 \pm 0.09$
HES - SRTD	$7.63 \pm 0.07$	$7.16 \pm 0.08$	$0.87 \pm 0.06$	$0.58 \pm 0.06$
CAL - SRTD	$10.19 \pm 0.08$	$9.67 \pm 0.08$	$-0.90 \pm 0.09$	$-0.75 \pm 0.08$

Table 4.2:  $\sigma$  of a Gaussian fit to the measured position difference in  $x$  and  $y$  for electrons with more than 5 GeV.

	$\sigma_x$ [mm]	$\sigma_y$ [mm]
HES	$6.33 \pm 0.10$	$6.16 \pm 0.09$
CAL	$9.25 \pm 0.17$	$8.96 \pm 0.15$
SRTD	$4.27 \pm 0.06$	$3.65 \pm 0.09$

Table 4.3: Width ( $\sigma$ ) of the position resolution in  $x$  and  $y$  for electrons with more than 5 GeV for HES, CAL and SRTD.

results of a Gaussian fit to the obtained distributions are shown in table 4.2. As three independent components have been used to determine the position, the resolution of each individual component can be calculated. The results of this calculation are listed in table 4.3.

The HES resolution in  $x$  and  $y$  is about 30% better than that of the calorimeter. Compared with the SRTD the HES has a worse resolution by about 30% in  $x$  and 40% in  $y$  but covers a much wider area.

### 4.2.3 Electron Identification with the HES

Starting with the diode with the highest energy deposit, a HES cluster of  $3 \times 3$  diodes is formed with the starting diode in its center. The energy deposit of all single diodes  $E_i$  in that  $3 \times 3$  cluster with energy greater than 0.6 mip is summed up and is called the total energy of the cluster  $E_{HES}$

$$E_{HES} = \sum_{i=1}^9 E_i \quad E_i > 0.6 \text{ mip} \quad (4.10)$$

Using the position reconstruction described in the previous chapter each cluster is assigned

a position. All diodes that have been assigned to the first cluster are removed from the entity of the diodes with energy hits and the procedure is repeated until no diode is left over. The correlation between the energy of a HES cluster and the calorimeter energy is good on average but as the width of the energy distribution is very big the energy of the particle cannot be taken from the HES itself. Therefore the calorimeter is used to determine the energy of the particle. The energy of the closest island object in the RCAL within a radius of 20 cm from the HES position is taken and treated as the energy  $E_{RCAL}$  of the HES object.

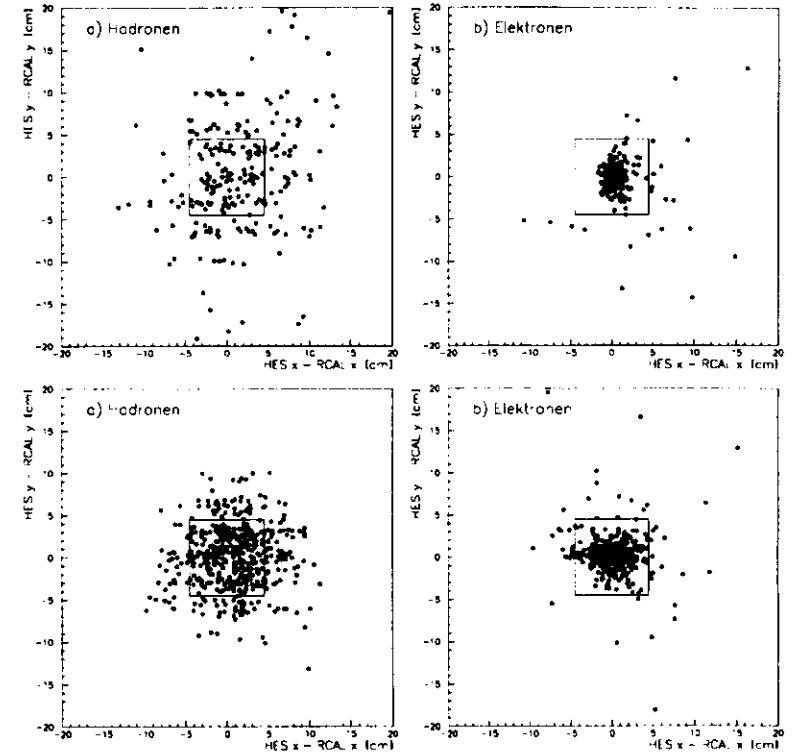


Figure 4.10: Comparison of the position of a) hadrons and b) electrons as measured by HES and CAL in a MC simulation (upper diagrams) and in data (lower diagrams). The square in the middle of the figures has a side length of 9 cm. The separation between hadrons and electrons is less clean for data than for MC. The reason is that the data has a contamination with other particle species. (from [FO95])

The position of the particle inside the calorimeter is determined using the routine ELECP0 and the calorimeter position is corrected according to the different  $z$ -position of the HES<sup>3</sup>. The correction is done assuming a straight trajectory of the electron and no correction for the

<sup>3</sup>The HES is positioned at  $z = -154$  cm.

magnetic field is done. In figure 4.10 the difference in the position between HES and CAL is shown for electrons and hadrons in data and MC.

The area contained by the square in the middle has a size of  $9 \times 9 \text{ cm}^2$ . As can be clearly seen the spread in the distribution is much larger for hadrons than for electrons. Therefore a cut on the difference of the RCAL and HES positions is made. The cut on the difference in the position between HES and CAL has been chosen to be less than 4.5 cm in  $x$  and  $y$ .

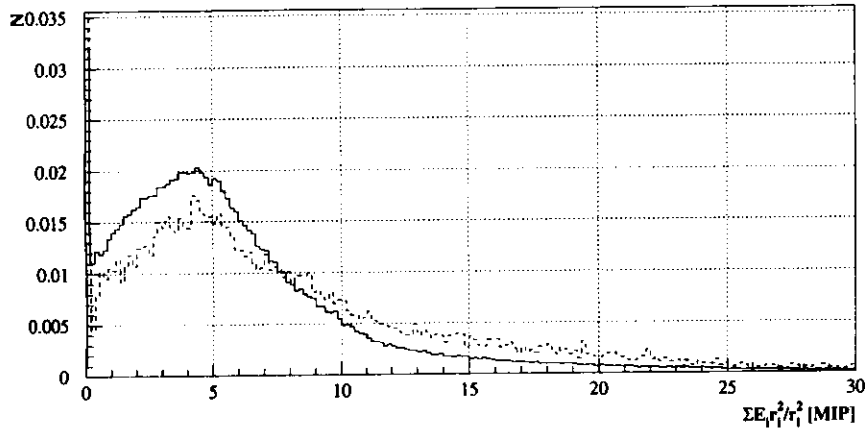


Figure 4.11: Distribution of the ratio  $\sum E_i r_i^2 / \langle r_i^2 \rangle$  for electron candidates in DIS (solid line) and Photoproduction Monte Carlo (dashed line).  $\sum E_i r_i^2 / \langle r_i^2 \rangle$  is the radius weighted energy distribution inside a  $5 \times 5$  cluster where  $r_i$  is the distance between the central and the surrounding diode  $i$  and  $E_i$  the energy of that diode.

Another possibility for the rejection of hadronic objects lies in their different energy distribution in the diode array of the HES object. From Monte Carlo studies on DIS and Photoproduction events it was seen that the best discriminating variable is the energy distribution inside a  $5 \times 5$  diode cluster described by the ratio  $\sum E_i r_i^2 / \langle r_i^2 \rangle$  where  $r_i$  is the distance between the central and the surrounding diode  $i$  and  $E_i$  is the energy of that diode. The distribution of this ratio for DIS and Photoproduction Monte Carlo data is shown in figure 4.11. A cut on  $\sum E_i r_i^2 / \langle r_i^2 \rangle < 12 \text{ mip}$  gets rid of about 21% of the photoproduction events and rejects about 10% of the DIS events.

For the selection of the HES electron if there are more than one candidate or candidates outside the HES area, MC studies have been done and led to the following results:

If there is a DIS electron outside the HES area<sup>4</sup> whose energy is called  $E_{\text{outside}}$ , a loose cut has been chosen. Only if this electron outside the HES has deposited at least 4 GeV more energy than the electron candidate found by HES, the event is rejected. Otherwise the HES

<sup>4</sup>This electron is identified by EEXOTIC.

candidate is taken.

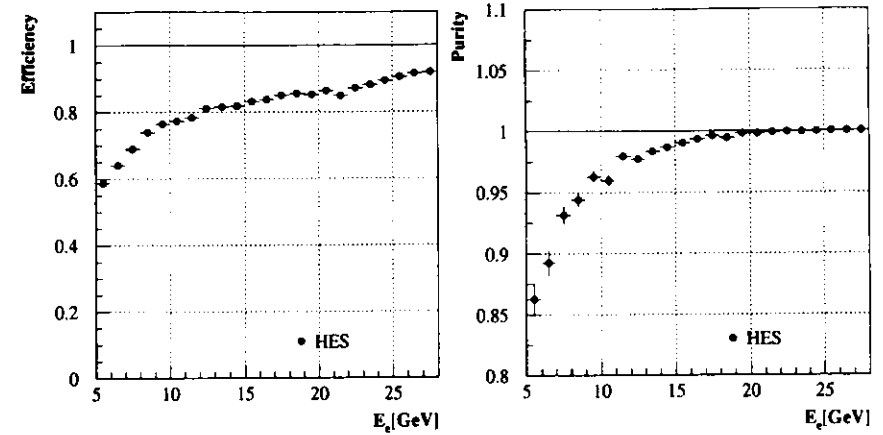


Figure 4.12: Efficiency (left) and purity (right) for the electron finder based on the information of the Hadron Electron Separator. The low efficiency at electron energies above 15 GeV is a result of the limited RCAL coverage of the HES.

Should there be more than one cluster fulfilling all cuts the one with the highest energy deposit in the HES ( $E_{\text{HES}}$ ) is assigned to the DIS electron. Combining everything mentioned above the following variables are calculated within the HES algorithm

$E_{\text{HES}}$	(mip)
$E_{\text{RCAL}}$	(GeV)
HES $x$	(cm)
HES $y$	(cm)
RCAL $x$	(cm)
RCAL $y$	(cm)
$E_{\text{outside}}$	(GeV)
$\sum_{5 \times 5} \frac{E_i r_i^2}{\langle r_i^2 \rangle}$	(mip)

and the following cuts are used for electron identification:

$E_{\text{HES}}$	$> 20 \text{ mip}$
$ \text{HES}_x - \text{RCAL}_x $	$< 4.5 \text{ cm}$
$ \text{HES}_y - \text{RCAL}_y $	$< 4.5 \text{ cm}$
$E_{\text{outside}} - E_{\text{RCAL}}$	$< 4 \text{ GeV}$
$E_{\text{RCAL}}$	$> 4 \text{ GeV}$
$\sum E_i r_i^2 / \langle r_i^2 \rangle$	$< 12 \text{ mip}$

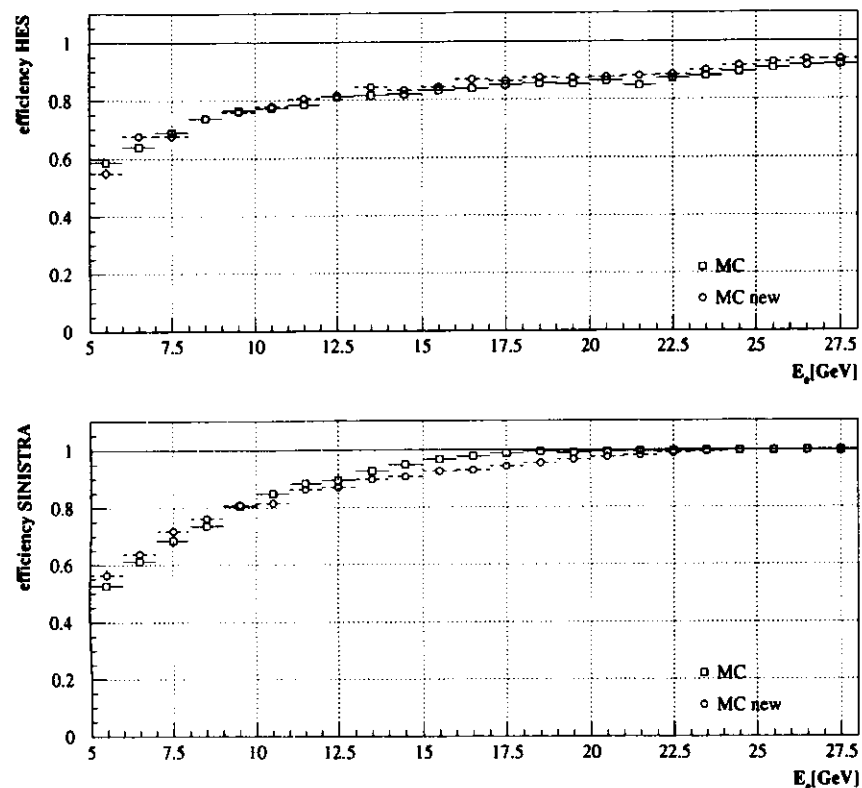


Figure 4.13: Efficiencies derived from DIS MC simulation. The open squares are obtained by the standard method (equation 4.1). The efficiency shown by the open circles is obtained by the assumption of two independent finders and equation 4.13.

Any HES cluster fulfilling all these cuts is called an electron.

A further improvement in rejecting hadrons can be achieved by looking at the ratio of energy in the electromagnetic and the hadronic part of the calorimeter. To keep the HES-based electron finding independent from the CAL-based, this option has not been used. With these cuts the efficiency and purity curves shown in figure 4.12 are achieved with the HES electron finder. The relatively low efficiency compared to the calorimeter electron finders at high energies ( $E > 15$  GeV) is due to the limited coverage of the HES (refer section 3.1.3). As the HES only covers about 84% of the RCAL area the efficiency cannot rise above this value. Actually it gets higher by a small amount because very energetic electrons produce a large shower and

their tails still hit the HES with a reasonable amount of energy.

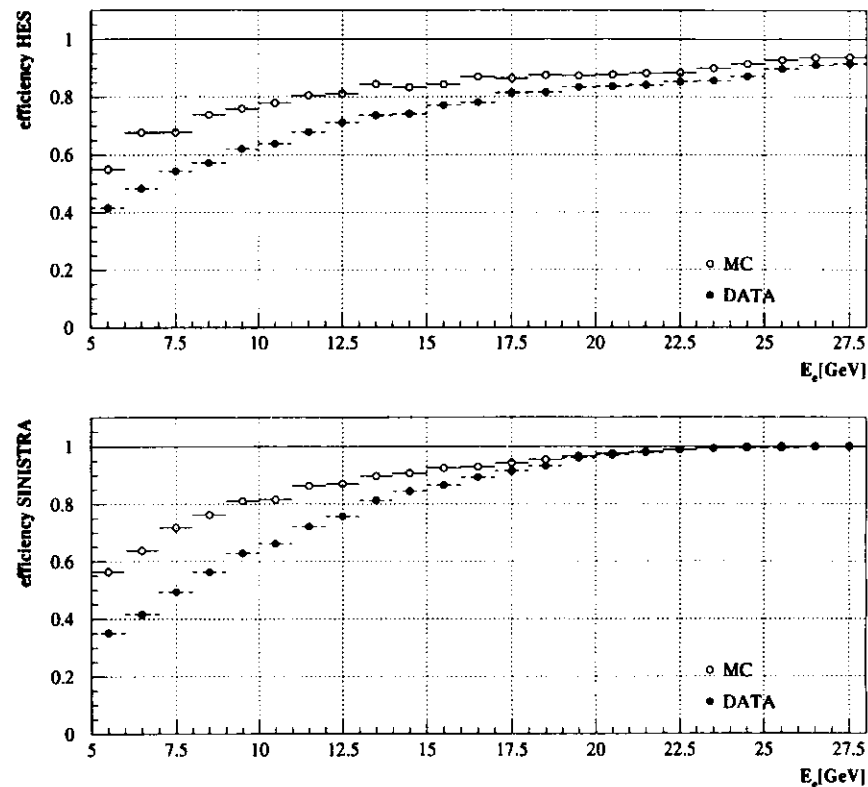


Figure 4.14: Efficiencies derived from DIS MC and DIS data with the assumption of two independent finders and equation 4.13.

### 4.3 Electron Finder Efficiencies

The efficiency of an electron finder is defined as the probability to correctly identify an electron. It is energy and event type dependent. One way to determine the efficiency of an electron finder is done on a sample of DIS Monte Carlo data. Here the number of generated (true) electrons is known and the efficiency is then calculated by equation 4.1 and the results for the different finders have been shown in figure 4.2 and 4.12.

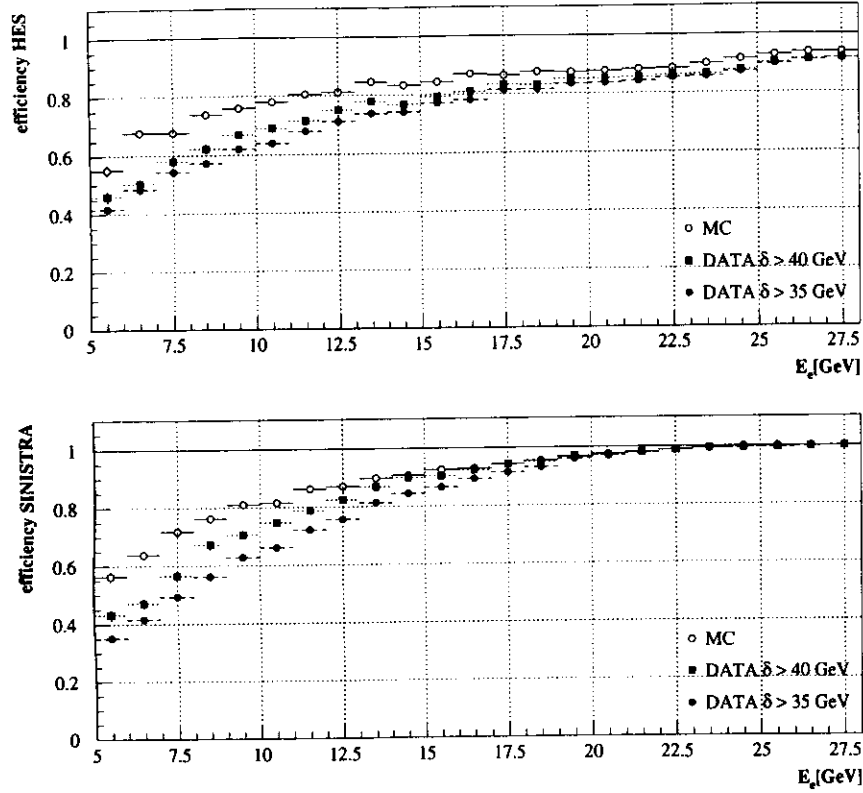


Figure 4.15: Efficiencies derived from DIS MC and DIS data with the assumption of two independent finders and equation 4.13. Different cuts on  $\delta$  have been applied to reduce the photoproduction background.

This method clearly depends on the detector simulation. A simulation independent efficiency computed from real data can be achieved by a combination of two independent electron finders which are compared to each other. The number of particles called electrons by finder 1 is given by

$$N(1) = N_e \cdot \epsilon(1) + N_h \cdot \eta(1) \quad (4.11)$$

with

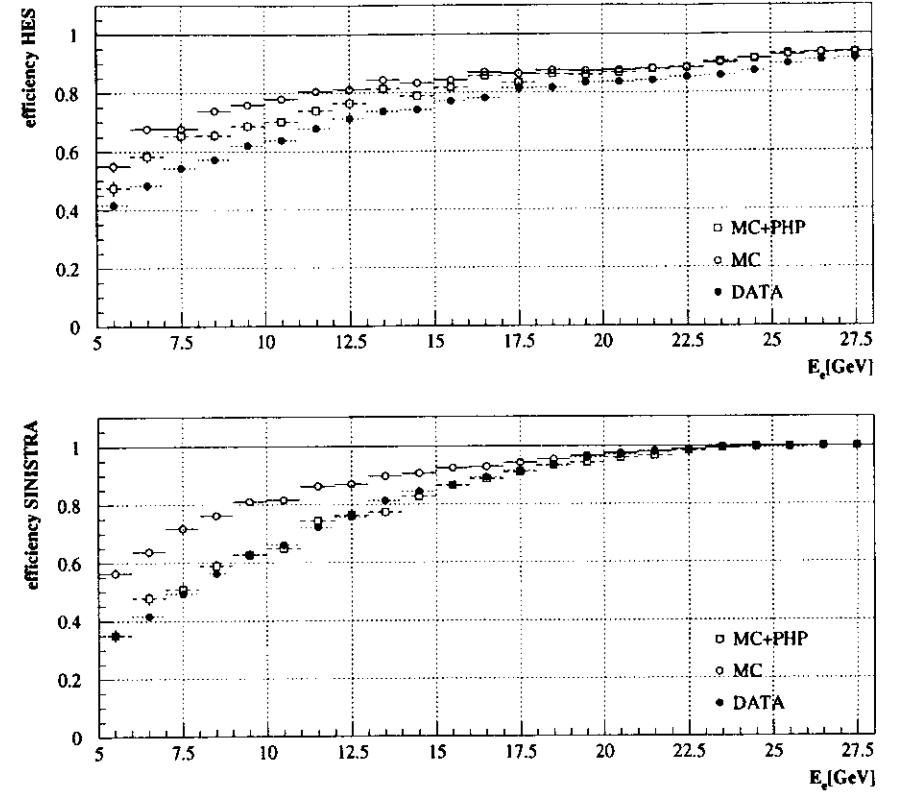


Figure 4.16: Efficiencies derived from a DIS MC with additional photoproduction events and DIS data with the assumption of two independent finders and the equation 4.13.

- $N_e$  true number of DIS electrons in the sample
- $\epsilon(1)$  efficiency of finder 1 for DIS electrons
- $N_h$  number of hadrons in the sample
- $\eta(1)$  probability to wrongly identify a hadron as an electron

where the misidentification probability  $\eta$  has been introduced.

The number of particles identified by a combination of two independent finders is given by

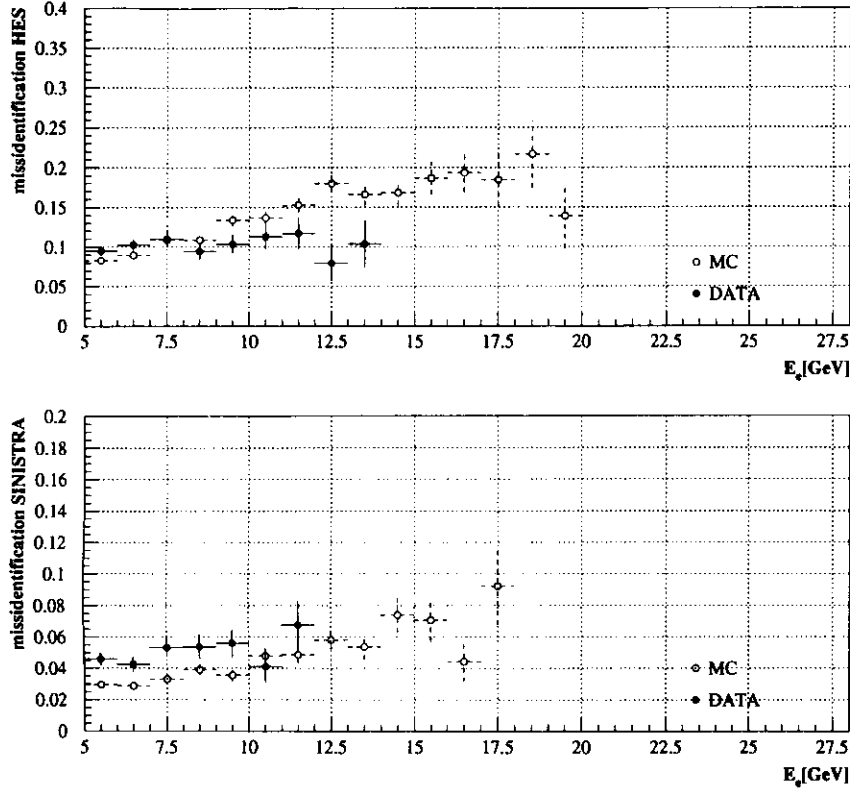


Figure 4.17: The misidentification probability  $\eta$  for different electron finders. The misidentification is derived from photoproduction Monte Carlo and photoproduction data where the misidentification is given by the ratio of electrons found ( $N$ ) and the total number of islands ( $N_{tot}$ ) in the rear calorimeter  $\eta = N/N_{tot}$  since in this event sample  $N_{tot} = N_h$ .

$$N(1 \oplus 2) = N_e \cdot \epsilon(1) \cdot \epsilon(2) + N_h \cdot \eta(1) \cdot \eta(2). \quad (4.12)$$

This equation is correct only if the two finders are independent.

Assuming the HES finder to be independent from the calorimeter finders, the HES and SINISTRA as the most commonly used finder are chosen as a set of independent finders. As a first check on their independence the efficiency is calculated from a DIS MC sample ( $N_h \approx 0$ ) using the ratio of electrons identified by both finders  $N(1 \oplus 2)$  and the number of electrons

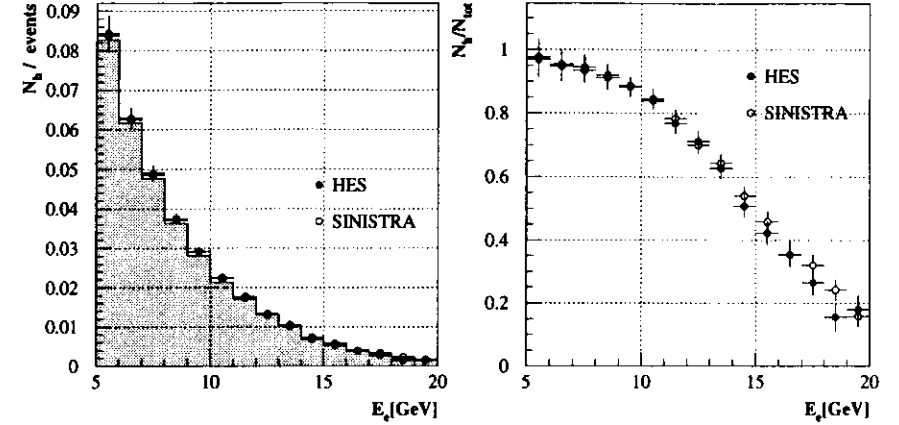


Figure 4.18: The lefthand plot shows the number of hadrons  $N_h$  per event in the DIS MC sample with additional photoproduction events. The number of hadrons has been calculated by equation 4.15 for the HES and SINISTRA electron finders. The shaded histogram in the lefthand plot shows the true number of hadrons as generated by the Monte Carlo. The righthand plot gives the ratio of the number of hadrons to the total number of islands in the rear calorimeter for the same data as the lefthand plot.

found by one finder  $N(1)$

$$\frac{N(1 \oplus 2)}{N(1)} = \frac{N_e \cdot \epsilon(1) \cdot \epsilon(2)}{N_e \cdot \epsilon(1)} = \epsilon(2) \quad (4.13)$$

where the hadronic contamination is neglected. The HES electron is identified by the cuts shown on page 61 and the SINISTRA electron is selected by  $P_{Si} > 0.9$ . In both cases it was further required that  $35 < \delta < 60$  GeV and the electron position has to be at least 3 cm from the calorimeter beampipe edge. The obtained result is shown as the open circles in figure 4.13 and as no significant difference to the standard MC method (open squares) is seen, the correlation between the two algorithms for electron identification is seen to be small for the present application. However there are deviations is the order of 5% and this uncertainty has to be taken as a systematic error on this method. If the two finders are positively correlated the efficiency will be overestimated by this method.

Based on the independence of the two finders the efficiency can now be calculated from DIS data since  $N(1 \oplus 2)$  and  $N(1)$  are known values. The result is shown as the closed circles in figure 4.14 where this efficiency is compared to the efficiency determined from the MC in the same way.

The observed discrepancy between data and Monte Carlo results from the hadronic contamination in the data sample originating from photoproduction events, which leads to a large

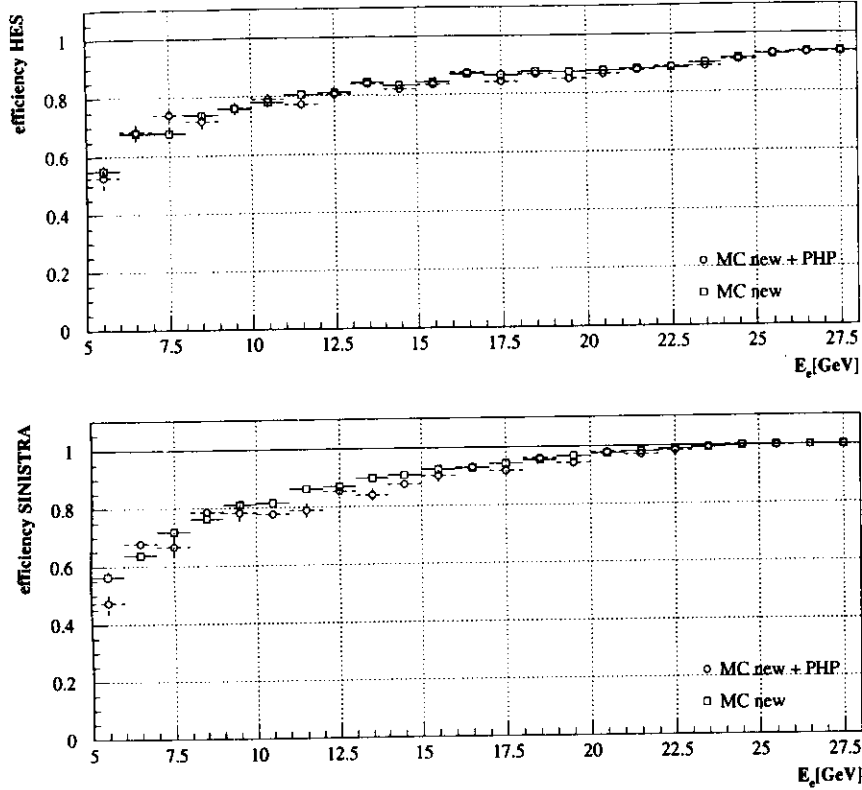


Figure 4.19: Efficiencies derived from DIS MC with additional photoproduction events after the correction on the hadronic background. The open squares are obtained by the standard method (equation 4.1). The efficiency shown by the open circles is obtained by the assumption of two independent finders and the equation 4.14.

number of  $N_h$  which therefore cannot be neglected. As the discrepancy seems to originate from photoproduction, it should diminish by increasing the  $\delta$ -cut (figure 4.15) or adding photoproduction MC events to the DIS MC sample (figure 4.16). In both cases the data and MC efficiencies for the finders tend to agree better, showing the contribution of the photoproduction events. Thus the comparison between HES and SINISTRA is influenced by the misidentification which has to be taken into account.

To determine the efficiency in the case of hadronic contamination, equations 4.11 and 4.12 have to be used and be solved for  $\epsilon$

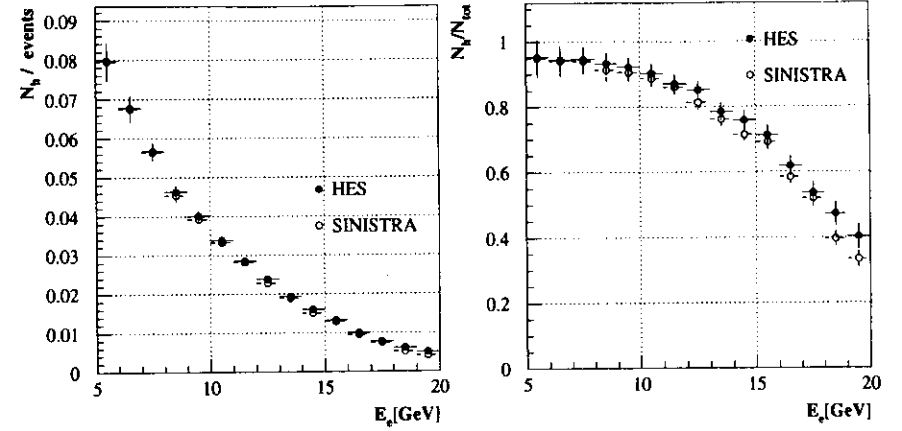


Figure 4.20: The lefthand plot shows the number of hadrons  $N_h$  per event in the DIS data. The number of hadrons has been calculated by equation 4.15 for the two different electron finders. The righthand plot gives the ratio of the number of hadrons to the number of islands in the rear calorimeter for real data.

$$\epsilon(2) = \frac{N(1 \oplus 2) - N_h \eta(1) \eta(2)}{N(1) - N_h \eta(1)} \quad (4.14)$$

where in this case  $N_h$ ,  $\eta(1)$  and  $\eta(2)$  have to be known.

The misidentification rate  $\eta$  can be determined by using photoproduction events which per definition do not contain DIS electrons. Photoproduction events can be obtained by a MC simulation or a selection of events with a signal in the electron calorimeter of the ZEUS luminosity monitor. All selected particles in the photoproduction data sample are therefore considered background, even photons and electrons and  $\eta$  is calculated as the number of electrons found ( $N$ ) divided by the total number of islands in the RCAL ( $N_{tot}$ ) which is  $\eta = N/N_{tot}$  since no electrons occur and  $N_{tot} = N_h$ . The probability  $\eta$  of calling a particle from a photoproduction event a DIS electron is shown for SINISTRA and HES in figure 4.17 for photoproduction MC and data.

The number of hadrons  $N_h$  can now be calculated using the total number of particles given by  $N_{tot} = N_h + N_e$  and inserting this relation into equation 4.11

$$N_h = \frac{N_{tot} \cdot \epsilon(1) - N(1)}{\epsilon(1) - \eta(1)} \quad (4.15)$$

$N_h$  depends on  $\epsilon$ , which is still unknown. The dependence is very small however. The best way to determine  $N_h$  is to use an estimate of  $\epsilon$  from MC and once  $N_h$  is known the efficiency can be calculated using equation 4.14.

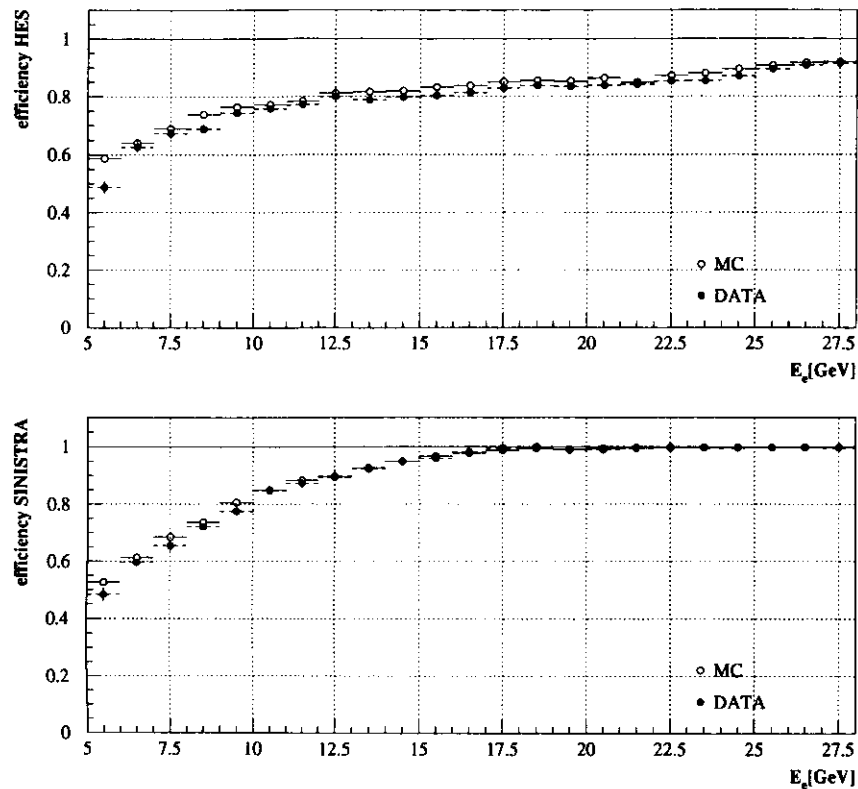


Figure 4.21: Efficiencies derived from DIS MC and DIS data after the correction on the hadronic background.

As a test for the method described so far, the efficiency is calculated from the DIS MC where photoproduction MC events have been added. As a first result the number of hadrons  $N_h$  is calculated with two different finders and compared to each other and the known number of hadrons (figure 4.18). For both finders the result agrees well with the true distribution. Knowing the hadronic contamination, the efficiency for both finders is calculated according to equation 4.14 and leads to the result shown in figure 4.19. As a comparison the MC efficiency obtained without hadronic contamination is shown as the open squares. For both finder consistent results are obtained, whereas deviations in the order of few percent occur and have to be seen as an additional systematic uncertainty.

Using this method of two finders as an estimate of the finder efficiencies on DIS data leads

to the hadronic distribution shown in figure 4.20 where again a good agreement between the two finders is achieved. Combining all this the resulting efficiency from DIS data is shown in figure 4.21.

First of all it is seen that the efficiency determined from MC alone, which is the method used by ZEUS so far, agrees with the independent determination. This shows, that the assumption of independence of the HES and CAL electron finders, which was used in this analysis, is justified within the domain of this analysis, since it yields consistent results. Only small deviations in the order of a few percent are seen between the data and the MC where the data efficiency is slightly lower than the MC efficiency and this cannot be caused by the correlation between the two finders. Furthermore a systematic deviation is seen for the HES finder as the data curve is lying systematically about 2.5 % below the MC curve. This indicates an uncertainty in the HES MC simulation. For both finders the MC and data curves disagree more in the low energetic region. This is due to the wrongly simulated inactive material in the MC and an uncertainty in the electron finding efficiency has to be taken into account in cross section determinations.

#### 4.4 Combining SINISTRA and HES

As seen before, SINISTRA and HES seem to be mostly independent. Therefore it should be possible to combine these two electron finders to get a better finder in particular for low energy electrons ( $E_e < 10$  GeV).

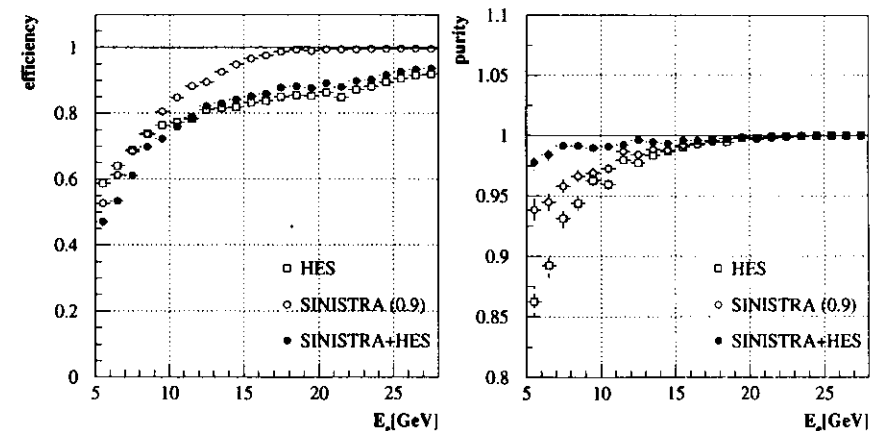


Figure 4.22: Efficiency (left) and purity (right) for SINISTRA (open circles), HES (open squares) and a combined finder of SINISTRA and HES (closed circles). For the combined finder a cut of  $P_{Si} > 0.5$  is used.

Since the combination of the very pure SINISTRA finder ( $P_{Si} > 0.9$ ) and the HES finder

has a very low efficiency in this energy range (roughly  $\epsilon_{\text{SINISTRA}} \cdot \epsilon_{\text{HES}}$ ), the probability of SINISTRA was changed to be greater than 0.5 which gives a higher SINISTRA efficiency but lower purity. An electromagnetic object is then called an electron if it is identified by SINISTRA ( $P_{S_i} > 0.5$ ) and fulfills all the required HES cuts given on page 61. Furthermore it is required that the HES and SINISTRA positions do not differ by more than 4.5 cm either in  $x$  or in  $y$  direction.

The efficiency of this combined finder is shown in figure 4.22. This finder gives an efficiency of more than 50% in the energy range of  $E_e < 10$  GeV. For energies greater than 10 GeV the combination gives a worse efficiency due to the limited coverage of the HES. The combined efficiency is even higher than the HES finder since the position cut is now applied on the SINISTRA candidate and not on the HES candidate. Therefore more HES candidates are accepted. The combination gives a much better purity (figure 4.22) which is most important in the low energy region where most of the photoproduction background shows up. Due to the low efficiency of the combined finder at high electron energies but good purity in the low energy range, the combination will only be used for electrons with  $E_e < 10$  GeV. Higher energetic electrons will be selected by using SINISTRA alone with  $P_{S_i} > 0.9$ .

## Chapter 5

# Determination of the Proton Structure Function $F_2$

### 5.1 MC Validation

Before any structure function can be extracted the resolutions, biases and acceptances have to be known. This can only be done in a Monte Carlo simulation and this simulation has to be validated.

The detector simulation is based on the GEANT [B87] program package whereas neutral current DIS events are generated using the HERACLES program [KSM91] which includes photon and  $Z^0$  exchanges and first order electro weak radiative corrections. The hadronic final state is simulated using the color-dipole model CDMBGF [ADKT85, Gus86, GP88, AGLP89] including all leading order QCD diagrams as implemented in ARIADNE [Lon92, Lon95] for the QCD cascade and JETSET [SB87] for the hadronisation. The ARIADNE model provides the best description of the observed DIS non-diffractive hadronic final state [ZEU93a, ZEU94]. Diffractive events which have been observed in the data [ZEU93c] by the occurrence of a large rapidity gap in the detector are simulated within ARIADNE by assuming that the struck quark belongs to a colorless state having only a small fraction of the proton's momentum. The parameters of the model are adjusted to be consistent with recent ZEUS measurements [ZEU95a]. The MRSA [MRS94] parton density parameterizations, modified at low  $Q^2$  as described in [MRS96] are used. A MC event sample corresponding to an integrated luminosity of  $1.54 \text{ pb}^{-1}$  for  $Q^2 > 1.8 \text{ GeV}^2$  was used.

### Vertex

The vertex is reconstructed from the tracks measured by the tracking detectors. Tracks are obtained from the tracking detectors by fitting individual tracks to the hits in the chambers. The resulting tracks are then fitted to an overall vertex position ( $z_{\text{vtx}}$ ).

The vertex distribution is relatively well reproduced by the MC as seen in figure 5.1 where the data vertex is compared to the MC. For  $z_{\text{vtx}} < -25$  cm an overshoot in the MC distribution is seen. This is probably due to beam gas background events which are included in the minimum bias photoproduction event sample which has been used to obtain the MC input vertex distribution. In the range of  $-25 < z_{\text{vtx}} < 100$  cm the MC and data distribution agree well and a corresponding cut will be used in this analysis. The second interaction point at  $z_{\text{vtx}} = +78$  cm is due to the proton satellite bunches produced by the HERA 208 MHz r.f. system (see section 2.2).

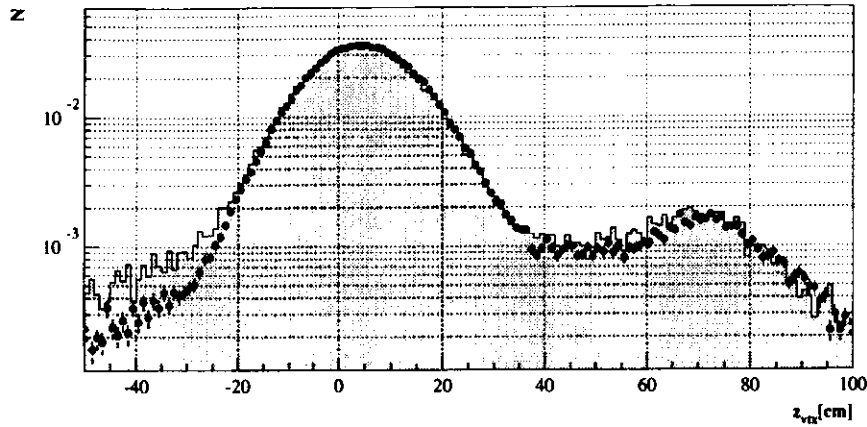


Figure 5.1: The diagram shows the vertex distribution in the MC simulation (shaded histogram) and in the data (closed circles). The distributions are normalized to one.

### Scattered Electron

In figure 5.2 the primary variables from the data sample which are used for the reconstruction of the kinematic variables are compared with the MC simulation.

The primary variables for the hadronic system are given by  $F_h$  and  $\gamma_h$ . The energy of the hadronic final state  $F_h$  is derived from

$$F_h = \frac{(\sum_h P_{x,h})^2 + (\sum_h P_{y,h})^2 + (\sum_h (E - P_z)_h)^2}{2 \cdot (\sum_h (E - P_z)_h)} \quad (5.1)$$

where the sum of the momenta and energies runs over all final state particles  $h$ .

The angle of the hadronic energy flow  $\gamma_h$  is calculated by summing energies and momenta of all final state hadronic particles  $h$  via

$$\cos \gamma_h = \frac{(\sum_h P_{x,h})^2 + (\sum_h P_{y,h})^2 - (\sum_h (E - P_z)_h)^2}{(\sum_h P_{x,h})^2 + (\sum_h P_{y,h})^2 + (\sum_h (E - P_z)_h)^2} \quad (5.2)$$

and can be regarded as the scattering angle of the struck quark in the naive quark parton model.

Both hadronic variables agree reasonably well between the data and the MC simulation as seen in the lower plots of figure 5.2.

The scattered electron is identified by the combination of the SINISTRA and HES electron finders as described in section 1.1.

The electron scattering angle  $\Theta_e$  is determined by using the reconstructed event vertex and the electron position as given by the SRTD. If no SRTD position is found, the position in

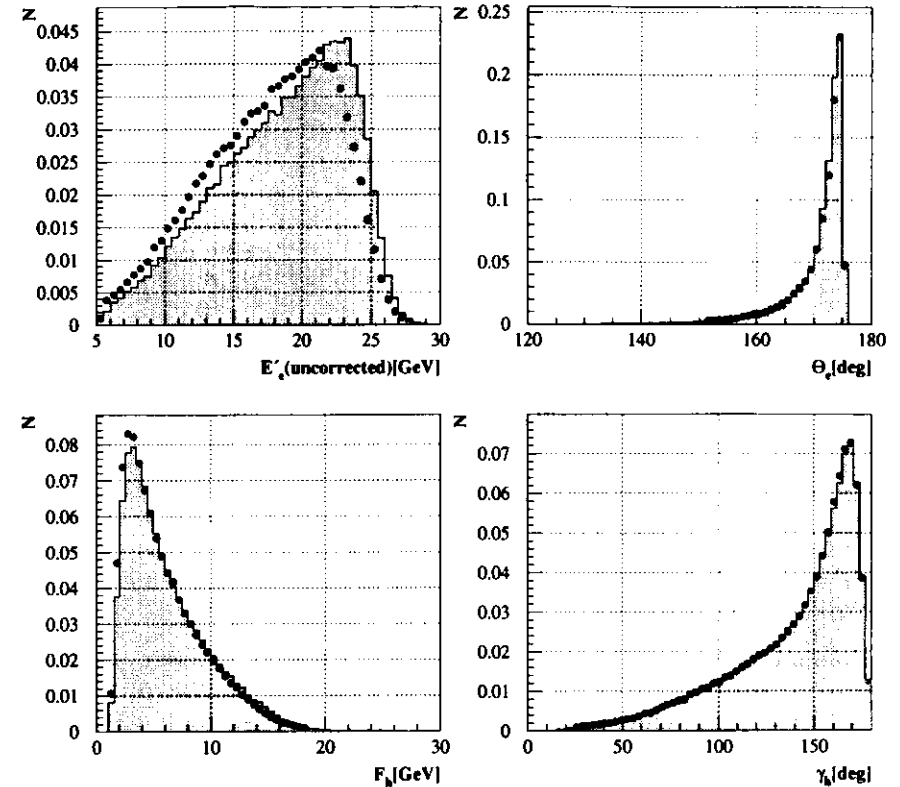


Figure 5.2: The shaded histograms show distributions for the primary variables  $E'_e$ ,  $\Theta_e$ ,  $F_h$  and  $\gamma_h$  (see text) in the MC simulation. The closed circles represent the distributions in the data. All distributions are normalized to one.

the HES is used since its resolution is better than the calorimeter position resolution (refer table 4.3). If no HES position is available the calorimeter position is taken. Furthermore the electron has to be found in the RCAL since the combined HES and SINISTRA finder is only applicable in that area. As seen in the upper right plot of figure 5.2 there is a good agreement between the electron scattering angle in the MC and the data.

This agreement does not hold for the distribution of the scattered electron energy  $E'_e$  seen in the upper left plot of figure 5.2. The shift in the energy distribution is an effect of the inactive material which has to be traversed by the electrons before they enter the ZEUS calorimeter. The MC simulation does not describe the ZEUS detector in all its details as complicated structures

like cable bundles are described by an average amount of inactive material. As a consequence the MC simulation underestimates the energy loss and a correction on the electron energy has to be applied in the further analysis.

The effects from the inactive material can be corrected by using the SRTD as a preshower detector. The integrated signal within the SRTD is proportional to the number of particles in the shower and is in turn related to the preshowering. Using the energy measured in the RCAL ( $E_{CAL}$ ) and the SRTD signal ( $E_{SRTD}$ ) the amount of energy loss can be estimated. By means of the SRTD it is possible to correct for the energy loss on an event by event basis. Assuming a linear Ansatz

$$E_{CAL} = a_0 + a_1 \cdot E_{SRTD} \quad (5.3)$$

with

$$a_i = \alpha_i + \beta_i \cdot E_{CAL}^{corrected} \quad (5.4)$$

yield the following parameterization

$$f(E_{CAL}, E_{SRTD}) = E_{CAL}^{corrected} = \frac{E_{CAL} - \alpha_0 - \alpha_1 \cdot E_{SRTD}}{\beta_0 + \beta_1 \cdot E_{SRTD}} \quad (5.5)$$

where the correction function  $f$  has been established on a sample of kinematic peak events where the energy of the scattered electron is nearly identical to the incident electron beam energy (27.52 GeV). For the energy range below 22 GeV a sample of QED Compton events where the electron and photon energies can be calculated from their respective angles is used. The gap between the kinematic peak and Compton events was filled by diffractive  $\rho$  events in DIS where the energy and position of the scattered electron can accurately be calculated from the two decay pion tracks.

Two sets of parameterizations were obtained on MC and data events. Thus different correction functions are used on DATA and MC where in the MC an energy smearing is added. The SRTD correction is available in the SRTD reconstruction code [NV95] and is applicable for electrons with a corrected energy down to 5 GeV with an uncertainty of 1 - 2% [EZ96].

Outside the SRTD region the calorimeter response is calibrated using kinematic peak positrons. This procedure is explored by H1 [H1 93b, H1 95] and also used by ZEUS [ZEU93b, ZEU95b].

The electron energy distribution obtained after these corrections is shown in figure 5.3 and shows a good agreement.

### Events with Rapidity Gaps

The distribution of the variable  $\eta_{max}$  which is defined as  $\eta_{max} = -\ln(\tan(\Theta/2))$ , where  $\Theta$  is the angle of the particle closest to the FCAL beampipe hole with an energy above a threshold, showed a significant difference in the MC and data distribution in the 1993 ZEUS analysis and led to the discovery of events with a large rapidity gap (LRG) by ZEUS [ZEU93c] and H1 [H1 94]. An event is called LRG event if  $\eta_{max} < 1.5$ . Figure 5.4 shows such an event as seen in the ZEUS detector.

The characteristics of these events is the missing hadronic activity in the forward region of the ZEUS calorimeter. There is however forward energy escaping the beam pipe which can be seen by the detector components installed downstream the proton beam direction. These

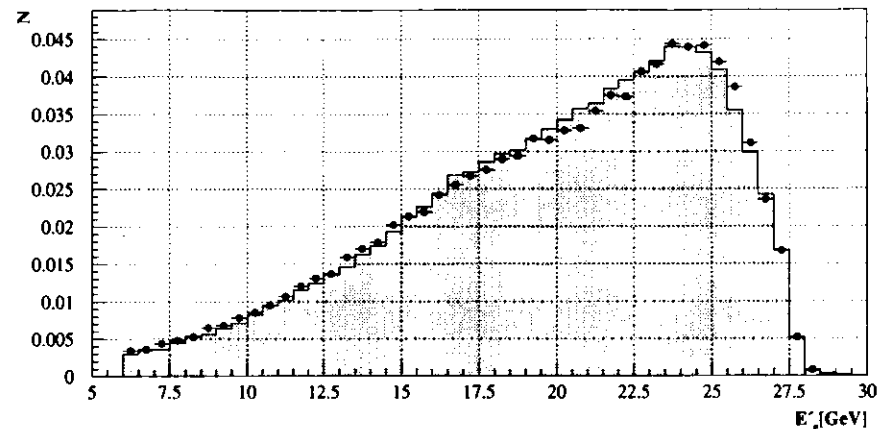


Figure 5.3: The shaded histogram shows the corrected MC electron energy distribution where the closed circles represent the corrected distribution in the data. The MC histogram changes compared to figure 5.2 due to the correction and smearing as described in the text. The distributions are normalized to one.

events are assumed to originate from diffractive dissociative scattering by the exchange of a pomeron carrying the quantum numbers of the vacuum.

Events with a rapidity gap are generated by the 1994 MC simulation as described at the beginning of this section. The  $\eta_{max}$  distribution for MC and data events is shown in figure 5.5 where a reasonably well agreement is seen.

## 5.2 Kinematic Reconstruction

The kinematics of deep inelastic electron proton scattering is described by the negative square of the four momentum transfer  $Q^2$  and the dimensionless variables  $x$  and  $y$  which were already introduced in section 1.2. These three variables are connected via  $Q^2 = sxy$  and thus for a given center of mass energy  $s$  the kinematics of a DIS event is given by two independent invariant variables which can be chosen from  $Q^2$ ,  $x$  and  $y$ . Four quantities are observed (see figure 5.6) in the experiment, the energy  $E_e'$  and deflecting angle  $\Theta_e$  of the scattered electron and the energy  $F_h$  and angle  $\gamma_h$  of the hadronic system. There are several different ways to calculate the two independent kinematic variables from these four quantities, either from the electron alone, from the hadronic system or from a combination of electronic and hadronic variables.

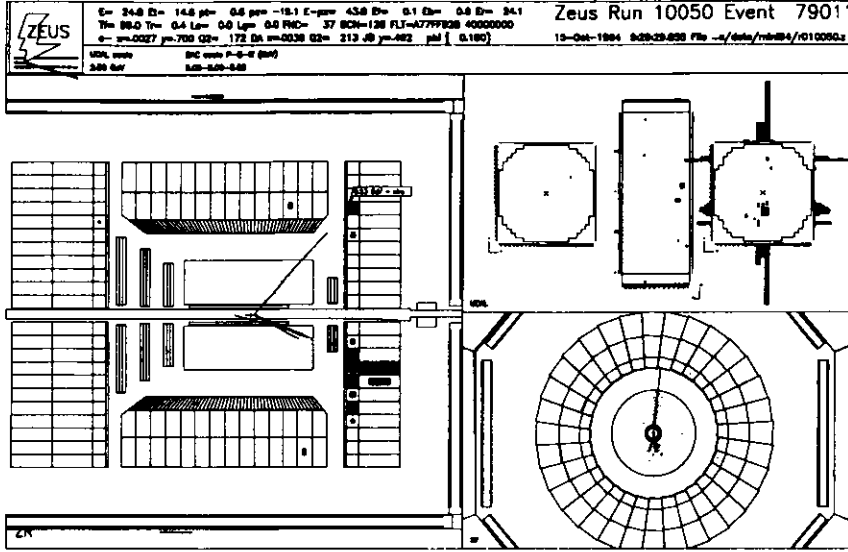


Figure 5.4: An event with a rapidity gap as seen in the ZEUS detector. The characteristic of these events is the missing hadronic activity in the forward region of the ZEUS calorimeter.

### 5.2.1 Electron-Only Method

This method uses the measured quantities of the scattered electron. From the electron beam energy  $E_e$ , the scattering angle  $\Theta_e$ , and the scattered electron energy  $E'_e$  the kinematic variables  $Q^2$  and  $y$  are derived by

$$Q_{el}^2 = 2E_e E'_e (1 + \cos \Theta_e) \quad (5.6)$$

$$y_{el} = 1 - \frac{E'_e}{E_e} (1 - \cos \Theta_e) \quad (5.7)$$

where the Bjorken  $x$  is then calculated to  $x = \frac{Q^2}{ys}$  with  $s \approx 300 \text{ GeV}$ .

### 5.2.2 Hadron-Only Method

Using the Jacquet-Blondel method [JB79] the kinematic variables are calculated by summing the energy  $E$  and projected momenta  $P_x$ ,  $P_y$  and  $P_z$  of all final state hadronic particles  $h$

$$Q_{JB}^2 = \frac{(\sum_h P_{T,h})^2}{1 - y_{JB}} \quad (5.8)$$

$$y_{JB} = \frac{\sum_h (E - P_z)_h}{2E_e} \quad (5.9)$$

where  $(\sum_h P_{T,h})^2 = (\sum_h P_{x,h})^2 + (\sum_h P_{y,h})^2$ .

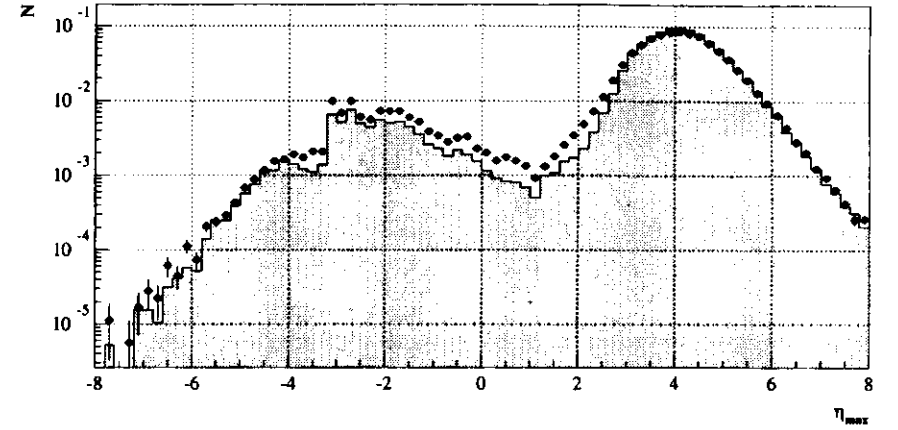


Figure 5.5: The shaded histogram shows the  $\eta_{max}$  distribution in the 1994 MC where the closed circles represent the distribution in the data. The discontinuity at  $\eta_{max} = -3.2$  is due to the beampipe edge in the RCAL. The distributions are normalized to one.

### 5.2.3 Double-Angle Method

This method [BEK91] relies on the angles of the scattered electron and the hadronic system. The angle of the hadronic energy flow  $\gamma_h$  is calculated according to equation 5.2 and the kinematic variables are then given by

$$Q_{DA}^2 = 4E_e^2 \frac{\sin \gamma_h (1 + \cos \Theta_e)}{\sin \gamma_h + \sin \Theta_e - \sin(\gamma_h + \Theta_e)} \quad (5.10)$$

$$y_{DA} = \frac{\sin \Theta_e (1 - \cos \gamma_h)}{\sin \gamma_h + \sin \Theta_e - \sin(\gamma_h + \Theta_e)} \quad (5.11)$$

### 5.2.4 $\Sigma$ -Method

This reconstruction method is used by H1 [BB94] and combines  $y_{el}$  and  $y_{JB}$  to calculate  $y$  and utilizes  $P_{t,e} = E'_e \sin(\Theta_e)$  in the calculation of  $Q^2$ :

$$Q_{\Sigma}^2 = \frac{P_{t,e}^2}{1 - y_{\Sigma}} \quad (5.12)$$

$$y_{\Sigma} = \frac{\sum_h (E - P_z)_h}{1 + y_{JB} - y_{el}} \quad (5.13)$$

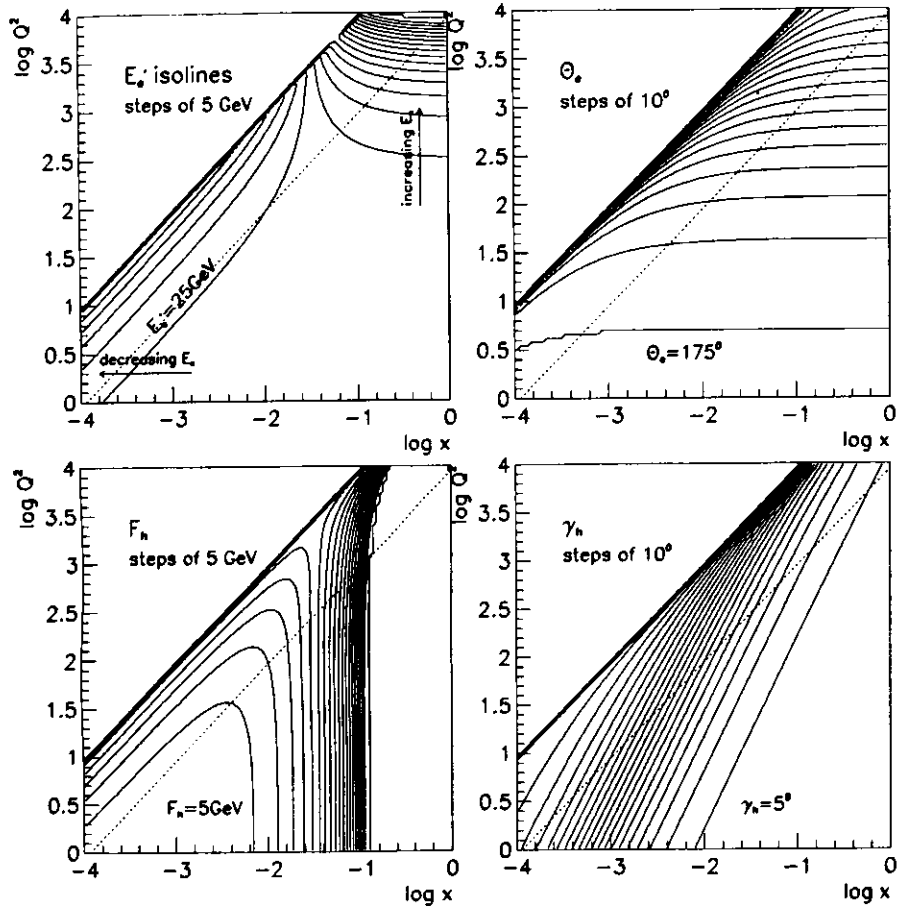


Figure 5.6: Isolines for the primary measured variables.

The accuracy of these four different methods is shown in figure 5.7 where the reconstructed values are plotted versus the true generated values. Each of the methods mentioned above becomes inaccurate in specific regions of the phase space.

The electron method only gives acceptable results at relatively large values of  $y$  where  $E_e'$  differs significantly from  $E_e$ . The relatively poor performance in the low  $y$  region is caused by the finite resolution of the positron energy measurement.

The Jacquet-Blondel method suffers from effects of energy loss, energy resolution and at low values of  $y$  of detector noise.

The Double-Angle method which is rather insensitive to energy losses becomes sensitive to detector noise at low values of  $y$ .

The correction for energy losses in the hadronic systems which is performed by the  $\Sigma$ -method

only holds for relatively large values of  $y$  and gets worse in the very low  $y$  region.

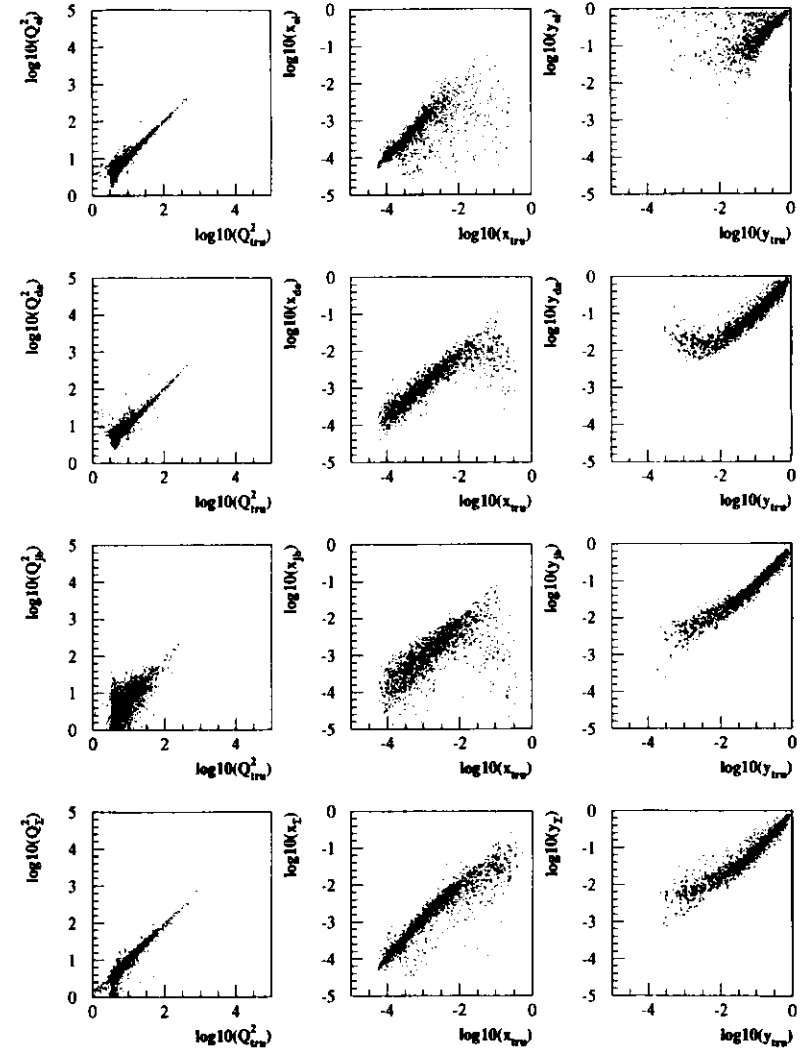


Figure 5.7: The reconstructed kinematic variables  $Q^2$ ,  $x$  and  $y$  versus their generated value for different reconstruction methods.

For this analysis which focuses on low electron energies (resp. high values of  $y$ ) the electron reconstruction method will be used. In figure 5.7 the  $\Sigma$ -method seems to be better than the electron reconstruction method but in the region of low  $x$  resp. high  $y$  which is of most interest in this analysis the electron reconstruction method is superior due to lower migrations as seen in figure 5.11.

### 5.2.5 $P_T$ -Method

A new method employed by the ZEUS collaboration for their recent  $F_2$  analysis [ZEU96a] is called  $P_T$ -method and allows an accurate measurement of the kinematic variables in a wide region of the  $x$ - $Q^2$ -plane. Thus it was possible to extend the ZEUS measurement to the low  $y$  region for an overlap with fixed target experiments. The  $P_T$ -method makes use of the fact that in fully contained DIS events the transverse momentum of the electron and the hadron system should balance and thus can be used to obtain an accurate determination of  $y$ . Using a correction function  $C(\frac{P_{T,h}}{P_{T,e}}, \gamma_h, P_{T,h})$  determined from Monte Carlo simulation,  $y$  is calculated similar to the  $\Sigma$ -method by

$$y_{P_T} = \frac{y_{JB}^{\text{measured}}}{C} \frac{1}{\frac{y_{JB}^{\text{measured}}}{C} + 1 - y_{el}} \quad (5.14)$$

The values of  $y_{P_T}$  and  $P_{T,e}$  are then used to determine a value for  $\gamma_{P_T}$

$$\cos \gamma_{P_T} = \frac{(P_{T,e})^2 - 4E_e^2 y_{P_T}}{(P_{T,e})^2 + 4E_e^2 y_{P_T}} \quad (5.15)$$

and the kinematic variables are determined from equation 5.10 and 5.11 by substituting  $\gamma_{P_T}$  for  $\gamma_h$ .

## 5.3 Event Selection

A typical DIS event is shown in figure 5.8 and several cuts which will be introduced in the following paragraphs have to be applied to identify a DIS event candidate in the data sample.

This analysis extends over the 1994 run range from 9667 to 10200 which corresponds to an integrated luminosity of  $1.54 \text{ pb}^{-1}$ . In a first step the events with DST bit 11 have been selected out of this data sample.

### 5.3.1 Trigger Selection

The DST bit 11 trigger requires the TLT Neutral Current bit and a cut of  $\delta + 2E_\gamma > 25 \text{ GeV}$  where  $E_\gamma$  is the energy seen in the photon calorimeter of the ZEUS luminosity monitor. Furthermore muons are rejected by the offline reconstruction routine ALHALO and sparks are removed by the routine RMSPARK.

The TLT neutral current bit is a logical OR of the SLT trigger bits DIS01, DIS02, DIS05, DIS06 and DIS07 which are set on the following conditions:

- DIS01 (nominal NC DIS filter) requires

$$- E - P_z + 2E_\gamma > 25 \text{ GeV}$$

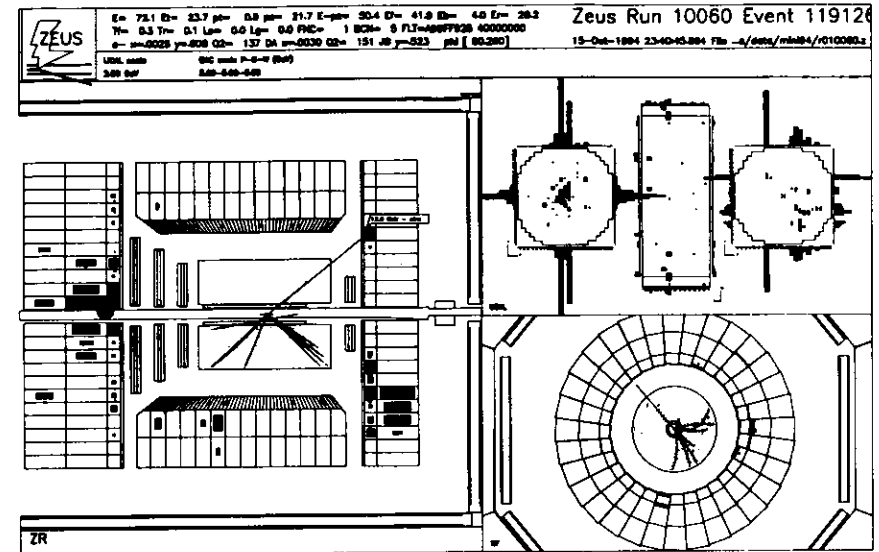


Figure 5.8: A typical DIS event as seen in the ZEUS detector. The electron is scattered into the RCAL and is balanced by the hadronic system G.

- $E_e > 4 \text{ GeV}$
- $E - P_z < 100 \text{ GeV}$
- DISCAL
- FLT-bits

- DIS02 (very high  $Q^2$  NC filter) requires

- $E - P_z > 25 \text{ GeV}$
- $E_e > 40 \text{ GeV}$
- $E - P_z < 100 \text{ GeV}$
- NoMuon
- FLT-bits

- DIS05 (Relaxed NC filter, no electron energy cut) requires

- $E - P_z + 2E_\gamma > 25 \text{ GeV}$
- $E - P_z < 100 \text{ GeV}$
- DISCAL
- FLT-bits

- DIS06 (Relaxed NC filter, no  $E - P_z$  cut) requires

- $E'_e > 4 \text{ GeV}$ .
- $E - P_z < 100 \text{ GeV}$
- DISCAL
- FLT-bits

- DIS07 (NC monitoring filter) requires

- $E - P_z + 2E_\gamma > 20 \text{ GeV}$
- $E - P_z < 100 \text{ GeV}$
- DISCAL
- FLT-bits

The DISCAL flag is set as the energy deposit in the RCAL EMC sections of the towers surrounding the beam pipe exceeds 6 GeV or the energy deposit in either the remaining RCAL EMC sections or the forward or barrel EMC sections is greater than 4 GeV. The main FLT trigger bits are set on the following conditions where further details can be found in [S95]:

- $\text{Remc-th} > 3.75 \text{ GeV}$ : This trigger requires the energy of the entire RCAL EMC region to be bigger than 3.8 GeV.
- $\text{Remc} > 3.4 \text{ GeV}$ : Requires the sum of the RCAL EMC region excluding the towers around the beam pipe to be bigger than 3.4 GeV.
- $\text{IsoE} > 2.5 \text{ GeV}$ : Trigger for energy deposits originating from isolated electrons or muons in the RCAL. Searches for a single or group of up to 4 trigger towers with electromagnetic or minimum ionizing test bits set that are completely surrounded by quite trigger towers. The IsoE condition requires the energy deposit in these isolated cells to be greater than 2.5 GeV and the corresponding HAC energy to be less than 0.95 GeV or no more than one third of the EMC energy.
- $\text{Bemc} > 4.8 \text{ GeV}$ : Requires the sum of the energy deposits in the BCAL EMC section to be bigger than 4.8 GeV.

From MC studies the efficiency of this trigger selection is seen to be close to 100% (figure 5.9). However this has to be checked on real data where two different methods are used.

The trigger efficiency can be calculated by choosing two independent triggers. To study the main trigger for the  $F_2$  analysis which is the IsoE trigger, a logical OR of Remc-th, Remc and Bemc is required. Furthermore all selection cuts of the analysis are applied and the electron has to be located in the RCAL. This event sample yields the denominator of the trigger efficiency. Requiring the addition constraint of the IsoE trigger on this event sample gives the numerator of the trigger efficiency evaluation. The resulting efficiency is shown as the open circles in figure 5.9.

Another independent check for the trigger efficiency is done by the requirement of DST bit 54 and the  $F_2$  selection cuts as the event sample for the denominator. The DST bit 54 is just the requirement of an energy deposit in the RCAL and is fully independent of the DST bit 11

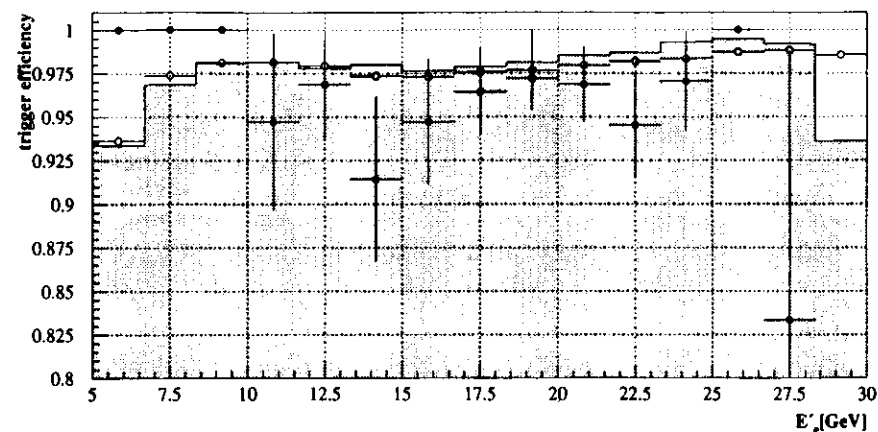


Figure 5.9: Trigger efficiency for DIS events as seen in the MC simulation (shaded histogram) and in the data by two different evaluations (open and closed circles). Further explanations are given in the text. Note that the y-axis ranges from 0.8.

trigger. The numerator is achieved by the addition requirement of DST bit 11. The obtained result is shown as the closed circles in figure 5.9. The low statistics of this trigger is due to its large prescale and allows only a rough estimate of the trigger efficiency.

Both trigger efficiency evaluations are comparable with the MC and agree reasonably well within the percent level. This inaccuracy will be included in the systematic error calculation of  $F_2$ .

### 5.3.2 Offline Selection Cuts

Beside DST bit 11 the event selection of this analysis requires that an electron candidate has to be found by the combination of the HES and SINISTRA electron finders as described in section 4.4 and all events with bad ZEUS running conditions were rejected by EVTAK [Sch]. After these requirements a total number of 464.600 events remained.

On this sample additional cuts have been applied for further background reduction:

- **Vertex cut:** A reconstructed vertex is required with a position of  $-25 < z_{\text{vtx}} < 100 \text{ cm}$ . This cut suppresses beam-gas background.
- **Delta cut:**  $35 \text{ GeV} < E - P_z < 60 \text{ GeV}$  - This cut removes events with large initial state radiation and eliminates most of the photoproduction background.
- **Energy cut:** The corrected energy of the scattered electron has to be greater than 6 GeV.

- **Box cut:** The electron has to be at least 3 cm off the calorimeter edge towards the beam-pipe. Thus scattered positrons within a box of  $26 \times 26 \text{ cm}^2$  around the center of the beam pipe are rejected. This ensures full containment of the electromagnetic shower in the calorimeter.
- **$y_{JB}$ -cut:**  $y_{JB} > 0.04$  - Reduces effects of the calorimeter noise.
- **$y_{el}$ -cut:**  $y_{el} < 0.95$  - This condition removes fake positrons which are found in the large energy deposit from the proton remnant in the FCAL.
- **Cosmic cut:** No cosmic candidate has to be identified by any of the muon finders ComCos, IsItaMu, MuTrig and AlHalo.

The number of events rejected and retained by the event requirements and selection cuts are listed in table 5.1. After these cuts 179.049 events remain for the extraction of  $F_2$  and their distribution in the primary and kinematic variables is shown in figure 5.10.

cut	retained	retained [%]	rejected	rejected [%]
DST bit 11	952.365	-	-	-
EVTAKE	941.643	98.3	10.722	1.1
Electron candidate	464.600	48.8	477.043	50.7
Vertex	344.035	36.1	120.565	26.0
Delta	304.914	32.0	39.121	11.4
Box	269.010	28.2	35.904	11.8
$E_e > 6 \text{ GeV}$	267.043	28.0	1.967	0.7
$y_{JB} > 0.04$	182.365	19.1	84.678	31.7
$y_{el} < 0.95$	180.345	18.9	2.020	1.1
Cosmic	179.049	18.8	1.296	0.7

Table 5.1: Number of events rejected and retained by the event requirements and selection cuts.

## 5.4 Unfolding

### 5.4.1 Migrations and Binning

Due to the limited detector resolution and kinematic reconstruction, migrations occur and the Monte Carlo simulation shows that the events are not reconstructed in the same place in the  $x$ - $Q^2$ -plane where they are originating from (figure 5.11). The observed distribution of the DIS data therefore has to be unfolded to get the underlying event distribution.

As a first step the remaining events after all DIS cuts have to be placed into a certain binning covering the accessible  $x$ - $Q^2$ -range. The bin sizes have to be chosen according to the resolution of the reconstructed kinematic variables shown in figure 5.12 for  $y_{el}$  and  $Q_{el}^2$ .

As the migration effects tend to go along lines of constant  $y$ , a binning in  $y$  and  $Q^2$  will be chosen to minimize the migration effects on the unfolding procedure. The following bin boundaries have been chosen for  $Q^2$  [ $\text{GeV}^2$ ] and  $y$ :

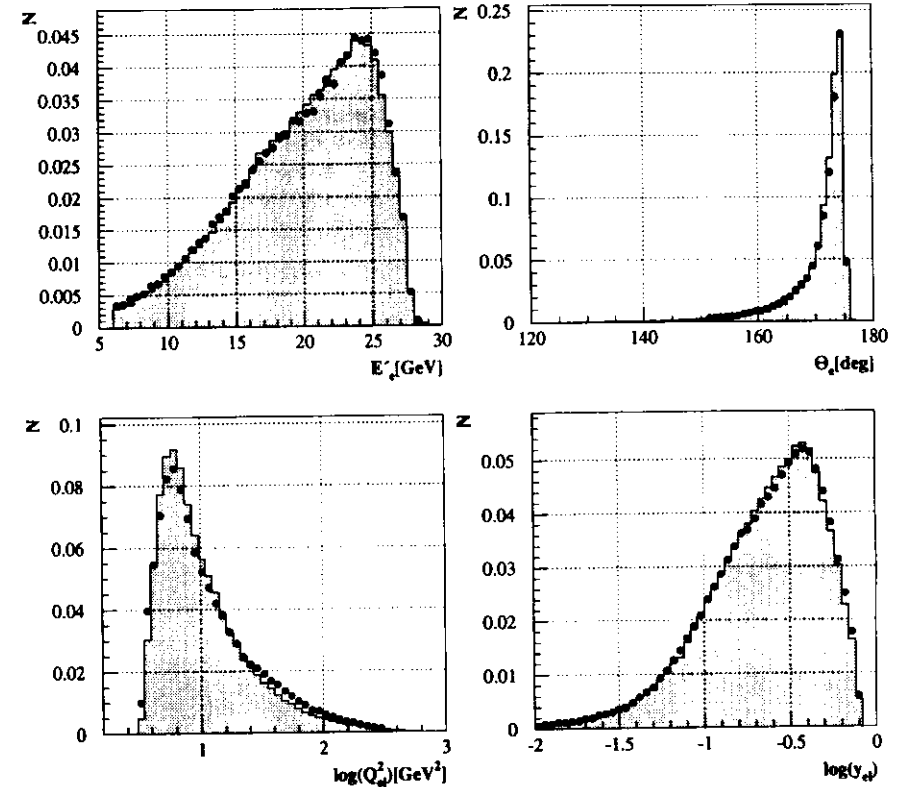


Figure 5.10: Distribution of the primary variables  $E_e'$ ,  $\Theta_e$  and the kinematic variables  $Q_{el}^2$  and  $y_{el}$  in the final data sample after all selection cuts have been applied. The shaded histograms give the distributions in the MC where the closed circles give the data distributions. All distributions are normalized to one.

$$\begin{array}{cccccccccccccccc}
 Q^2: & 2.2 & 3.2 & 4.0 & 5.0 & 7.0 & 9.0 & 11.0 & 13.0 & 16.0 & 20.0 & 25.0 & 32.0 \\
 & 40.0 & 50.0 & 65.0 & 85.0 & 110.0 & 140.0 & 185.0 & 240.0 & 310.0 & 410.0 & 530.0 & 710.0 \\
 y: & 0.0001 & 0.012 & 0.06 & 0.14 & 0.28 & 0.45 & 0.65 & 0.8 & 0.95
 \end{array}$$

and the resulting binning for this analysis is shown in figure 5.13 together with the distribution of a fraction of the final DIS events.

MC studies allow to define criteria for the quality of each bin and only bins fulfilling these criteria are taken into account for the analysis. The criteria are defined as the quantities smearing

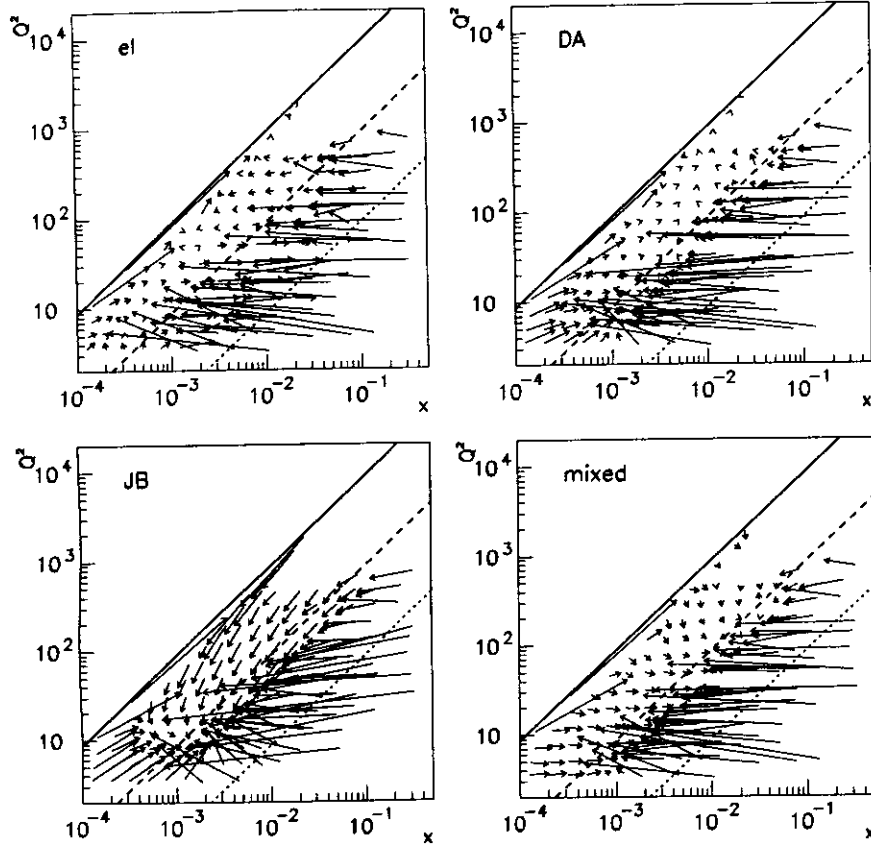


Figure 5.11: Migration effects of the different reconstruction methods due to the detector resolution as seen in MC.

$$S = \frac{\text{events generated and reconstructed in bin}}{\text{events generated in bin}}, \quad (5.16)$$

purity

$$P = \frac{\text{events generated and reconstructed in bin}}{\text{events reconstructed in bin}} \quad (5.17)$$

and the acceptance

$$A = \frac{\text{events generated in bin and reconstructed}}{\text{events generated in bin}}. \quad (5.18)$$

A bin is accepted as good if  $P > 0.25$ ,  $A > 0.2$  and the number of measured events in this

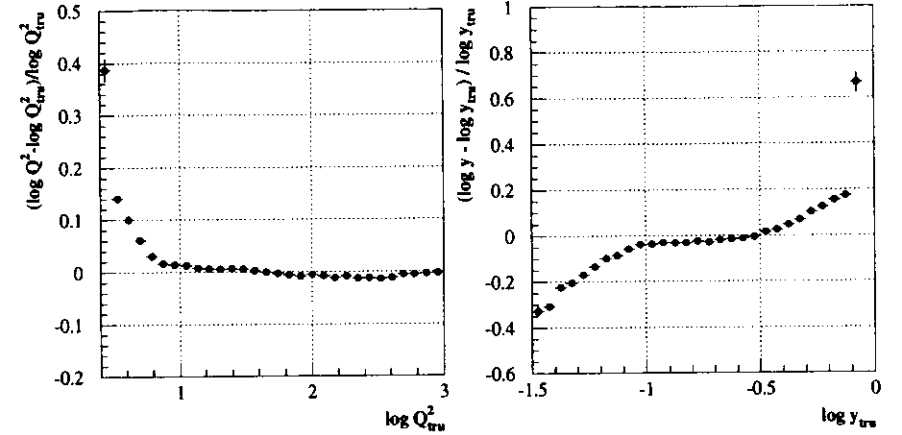


Figure 5.12: Resolution of the reconstructed kinematic variables  $Q^2$  (left) and  $y$  (right) for the electron reconstruction method versus the true generated value of  $Q^2$  and  $y$ .

bin exceeds 10. All events not sitting in these 'good bins' are accumulated in one background bin.

### 5.4.2 Background Subtraction

Before the unfolding procedure starts, the remaining background in the DIS sample has to be removed. This is done by a fit to the  $\delta$ -distribution (see section 4.1) in each bin as shown in figure 5.14. As a first step a fit to the DIS MC  $\delta$ -distribution is done with the following functional form:

$$\Delta^{MC}(\delta) = A e^{-\frac{(\delta - \delta_0^{MC})^2}{2\sigma_{MC}^2}} \quad \text{for } \delta > \delta_0^{MC}$$

$$\Delta^{MC}(\delta) = C + (A - C) e^{-\frac{(\delta - \delta_0^{MC})^2}{2(\sigma_{MC}^2 + \sigma_{rad}^2)}} \quad \text{for } \delta < \delta_0^{MC}.$$

This form is based on the assumption that the photoproduction background is a Gaussian distribution around the central value  $\delta_0^{MC}$  with a width of  $\sigma_{MC}$  due to detector resolution and an additional tail towards the lower values of  $\delta$  due to radiation with an additional width of  $\sigma_{rad}$ . For the data distribution a form

$$\Delta^{data}(\delta) = \Delta_1(\delta) + \Delta_2(\delta)$$

$$\Delta_1(\delta) = B A e^{-\frac{(\delta - \delta_0^{data})^2}{2\sigma_{data}^2}} \quad \text{for } \delta > \delta_0^{data}$$

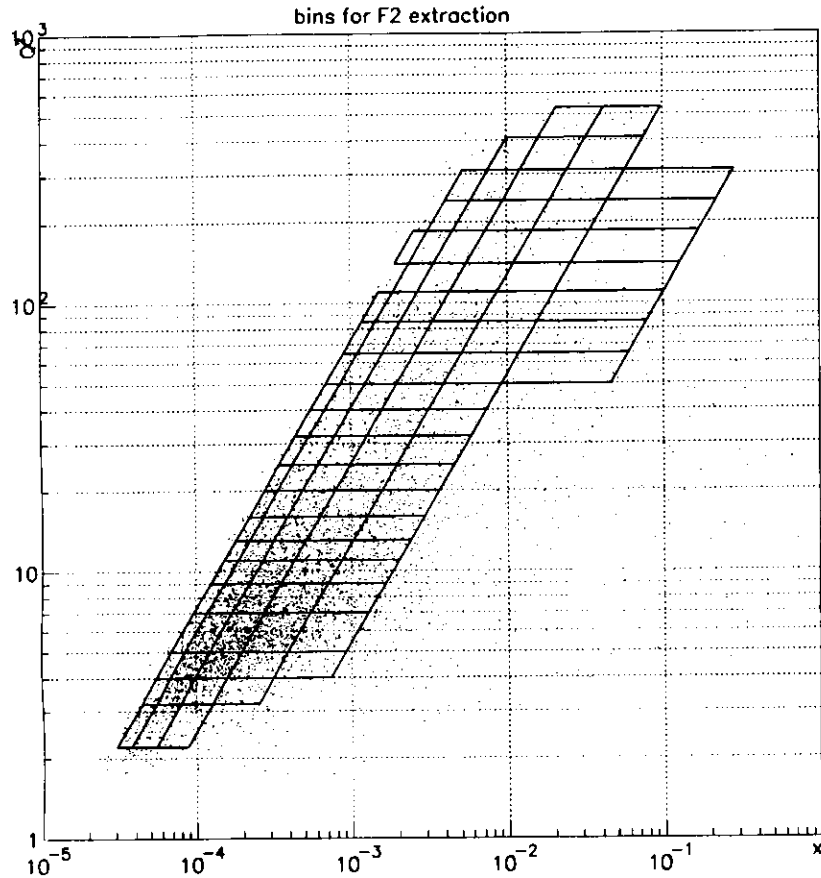


Figure 5.13:  $y$ - $Q^2$ -binning used in this analysis and a fraction of the final DIS events. Only the bins which fulfill the quality criteria of  $P > 0.25$ ,  $A > 0.2$  and  $N > 10$  are shown.

$$\Delta_1(\delta) = BC + B(A - C) e^{-\frac{(\delta - \delta_0^{data})^2}{2(\sigma_{data}^2 + \sigma_{rad}^2)}} \quad \text{for } \delta < \delta_0^{data}$$

$$\Delta_2(\delta) = D e^{-\frac{(\delta - \delta_0^{MC})^2}{2\sigma_{HP}^2}}$$

is used where a function  $\Delta_2(\delta)$  has been added to represent the contribution due to photoproduction. The parameters A, B, C and D are used for normalization purpose. All variables

which appear in the data and the MC functions are fixed in a fit to the MC. The contribution from the photoproduction background is then given by

$$N_{BG} = \int_{\delta_{low}}^{\delta_{high}} \Delta_2(\delta) d\delta \quad (5.19)$$

where  $\delta_{low}$  and  $\delta_{high}$  are given by the upper and lower values of the  $\delta$ -cut in the event selection. The correction for the energy mismatch of the central values of  $\delta_0^{MC}$  and  $\delta_0^{data}$  is given by

$$N_{lost} = \int_{\delta_{lost}}^{\delta_{low}} \Delta_1(\delta) d\delta \quad (5.20)$$

where  $\delta_{lost} = \delta_{low} - (\delta_0^{MC} - \delta_0^{data})$ . The corrected number of events in a particular bin is then given by

$$N_{bin}^{corr} = N_{bin}^{uncorr} + N_{lost} - N_{BG}. \quad (5.21)$$

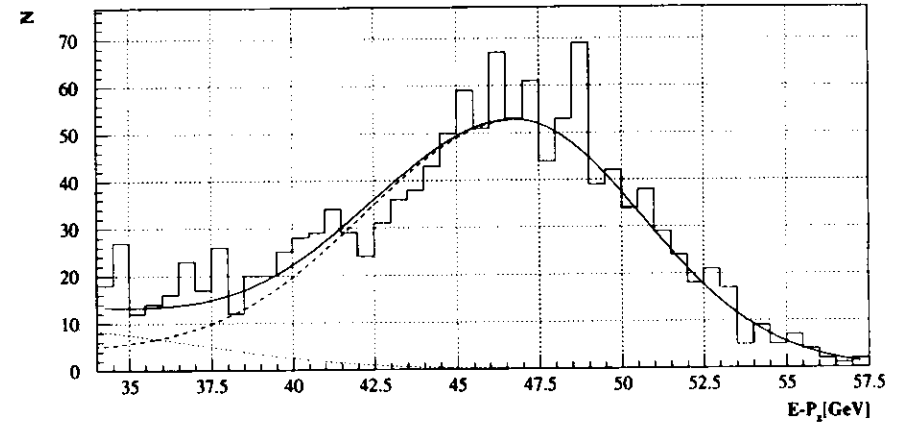


Figure 5.14: Fits to the  $\delta$ -distribution in a certain bin of the final event sample. The solid line represents the fit to the overall shape where the dashed line gives the contribution from DIS events and the dotted line the contribution due to photoproduction events.

Beam gas background is subtracted by looking at events which pass the DIS selection cuts but originate from a single electron (e-gas) or proton (p-gas) bunch. These events are reweighted by their bunch current compared to the current of the colliding bunches and thus give an estimate of the amount of beam gas events. This number is subtracted from the observed number of events in the corresponding bin.

### 5.4.3 Unfolding Procedure

After background subtraction the event distribution can be unfolded by the method described below. The quantities used in the unfolding are listed in table 5.2.

Quantity	Comment
$N(jx, jq)$	Number of events with a generated $x$ and $Q^2$ which lie in the bin $jx, jq$ for the MC simulation
$M(ix, iq)$	Number of events with a measured $x$ and $Q^2$ which lie in the bin $ix, iq$ for the MC simulation
$f(ix, iq, jx, jq)$	Transfer function describing the probability that an event generated in bin $jx, jq$ will be measured in bin $ix, iq$ . This function is determined from a MC simulation
$N^{data}(jx, jq)$	The true distribution of the data events sitting in bin $jx, jq$
$D(ix, iq)$	The measured data events sitting in bin $ix, iq$

Table 5.2: Summary of the quantities used in the unfolding procedure.

The number of MC events with a measured  $x$  and  $Q^2$  in a particular bin  $M(ix, iq)$  is related to the number of generated events in the same and in the surrounding bins  $N(jx, jq)$  by

$$M(ix, iq) = \sum_{jx, jq} N(jx, jq) f(jx, jq, ix, iq). \quad (5.22)$$

The function  $f$  gives the probability that an event with true values  $x$  and  $Q^2$  lying in bin  $jx, jq$  will have a measured  $x$  and  $Q^2$  which lies in bin  $ix, iq$ . This function is determined from the MC simulation and includes the smearing due to the kinematic reconstruction, detector resolution, reconstruction efficiencies and selection cuts.

A similar equation is valid for the events in the data

$$D(ix, iq) = \sum_{jx, jq} N^{data}(jx, jq) f(jx, jq, ix, iq). \quad (5.23)$$

The true event distribution  $N^{data}(jx, jq)$  can in principle be obtained by inverting equation 5.23. However, here an approximative unfolding is carried out in an iterative way suggested by H. Abramowicz and used in the 1993 ZEUS  $F_2$  analysis [ZEU95b].

The number of MC events is first normalized to the number of measured events in the region of 'good bins'. For the well measured bins a prediction for the true distribution is obtained by

$$N_{n+1}(ix, iq) = \frac{D(ix, iq)}{M_n(ix, iq)} N_n(ix, iq). \quad (5.24)$$

All the bins outside the well measurable region are normalized by a factor

$$\alpha = \frac{\sum D(ix, iq)}{\sum M_n(ix, iq)} \quad (5.25)$$

where the summation is extended over all 'good bins'. A new measured distribution  $M_{n+1}(ix, iq)$  is then obtained by the new generated distribution  $N_{n+1}(jx, jq)$  according to

equation 5.22. The new measured distribution is then normalized to the data and for each bin a value  $\chi_{bin}^2$  is calculated via

$$\chi_{bin}^2 = \frac{[D(ix, iq) - M(ix, iq)]^2}{D(ix, iq) + M(ix, iq)}. \quad (5.26)$$

This value is shown for the single bins and each iteration step in figure 5.15. It is seen that the value of  $\chi_{bin}^2$  converges rapidly towards zero in most of the bins in the  $y$ - $Q^2$ -plane. Only in the region of very low  $Q^2$  and low  $y$  the unfolding gets problematic.

An overall  $\chi^2$  is calculated by summing the individual  $\chi_{bin}^2$  of the good bins and the whole procedure is repeated until certain quality criteria are reached and the unfolded data distribution is then given by

$$N^{data}(jx, jq) = N_n(jx, jq). \quad (5.27)$$

The quality criteria for each iteration is given by the overall  $\chi^2$  which decreases with each iteration step and a value of

$$H_n^2 = \sum_i \sum_j \text{neigh}(i, j) [N_n(ix, iq) - N_n(jx, jq)]^2 \quad (5.28)$$

which measures the smoothness of the resulting event distribution and remains roughly constant during the iteration procedure. The function  $\text{neigh}(i, j)$  is equal to one for neighboring bins  $i$  and  $j$ , otherwise it is equal to zero. The iteration is stopped if

$$\chi^2 < 1.1 \quad (5.29)$$

$$\text{or } \Delta\chi^2 < 0 \quad (5.30)$$

$$\text{or } \frac{\Delta H^2}{H^2} < -0.02 \text{ and } \frac{\Delta\chi^2}{\chi^2} < 0.10 \quad (5.31)$$

$$\text{or } \frac{\Delta H^2}{H^2} < -0.10. \quad (5.32)$$

As the error propagation relies on the covariance matrix which is not computed in this unfolding procedure, the statistical error of the unsmearred physical distribution has to be estimated from the statistical errors of the theoretical input distribution  $N$ , the corresponding MC-prediction  $M$  and the experimentally observed distribution  $D$ . Assuming a statistical independence of the three distributions the error on the unsmearred distribution is

$$\delta N_n^{data} = N_n^{data} \cdot \sqrt{\frac{1}{N_n} \frac{1}{M_n} \frac{1}{D}}. \quad (5.33)$$

The data distribution as obtained from equation 5.27 can then be used for the extraction of  $F_2$ .

## 5.5 Determination of the Structure Function $F_2$

For positron-proton scattering the observed differential NC cross section can be written as

$$\sigma =: \frac{d^2\sigma}{dx dQ^2} = \frac{2\pi\alpha^2}{xQ^4} Y_+(F_2 - \frac{y^2}{Y_+} F_L - \frac{Y_-}{Y_+} x F_3) = \sigma(F_2) + \sigma(F_L) + \sigma(F_3) \quad (5.34)$$

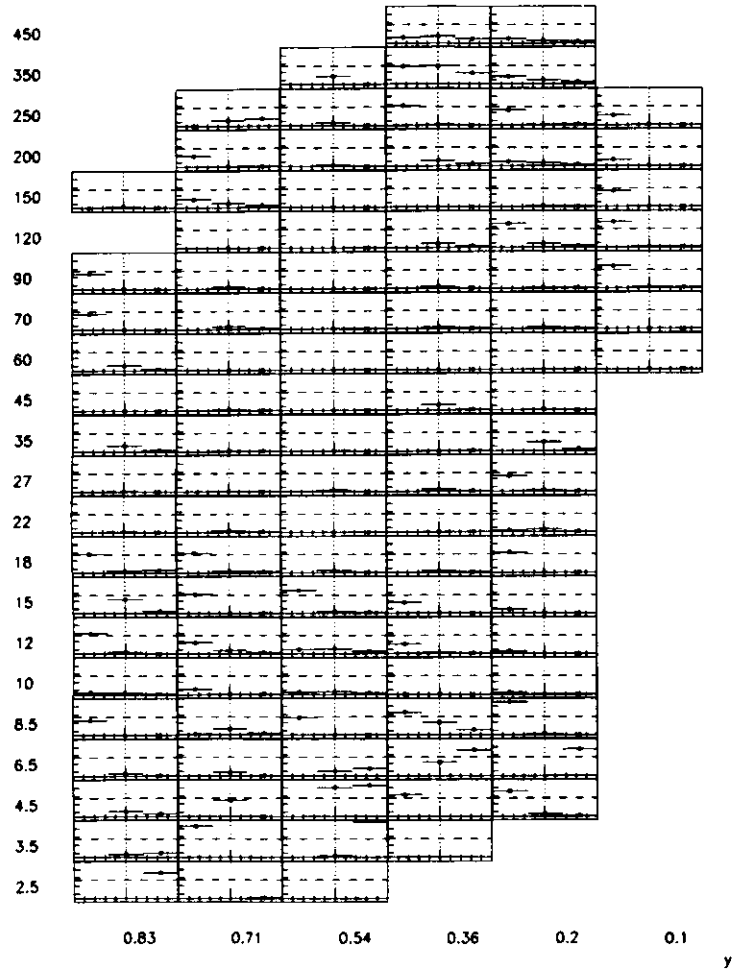
Q<sup>2</sup>

Figure 5.15: The value of  $\chi^2_{\text{bin}}$  is shown for each 'good' bin in the  $y$  and  $Q^2$  range as a function of the number of iteration. The solid lines compare to a value of  $\chi^2_{\text{bin}} = 0$  where the dashed lines compare to  $\chi^2_{\text{bin}} = 5$ .

where the cross section is directly given by the unfolded event distribution  $N^{\text{data}}$  (equation 5.27) and

$$\hat{\sigma} = \frac{N^{\text{data}}}{\mathcal{L}A} \quad (5.35)$$

where  $\mathcal{L}$  is the measured integrated luminosity and  $A$  is the acceptance as defined in equation 5.18.

The 'observed' structure function  $\hat{F}_2$  is then given by

$$\hat{F}_2 = \frac{xQ^4}{2\pi\alpha^2 Y_+} \hat{\sigma} \quad (5.36)$$

and the structure function  $F_2$  is related to  $\hat{F}_2$  via

$$\hat{F}_2 = F_2(1 + \delta_{F_L} + \delta_Z)(1 + \delta_{RC} + \delta_{\text{bin}}) \quad (5.37)$$

where the correction factors originate from  $F_L$  ( $\delta_{F_L}$ ) and  $Z^0$  ( $\delta_Z$ ) contribution as well as from QED radiation ( $\delta_{RC}$ ) and bin centering ( $\delta_{\text{bin}}$ ). The correction factors  $\delta_{F_L}$  and  $\delta_Z$  are obtained from

$$\delta_{F_L} = \frac{\sigma(F_L)}{\sigma(F_2)} \quad (5.38)$$

$$\delta_Z = \frac{\sigma(F_3)}{\sigma(F_2)}. \quad (5.39)$$

The contribution of  $\delta_{F_L}$  is in the order of a few percent in the high  $y$  region and negligible elsewhere. Its contribution in the single bins is explicitly listed in tables A.1-A.4 where the final results on  $F_2$  are summarized.

The single cross sections are given by

$$\sigma(F_2) = \int \int_{\text{bin}} dx dQ^2 \frac{2\pi\alpha^2}{xQ^4} Y_+ F_2(x, Q^2) \quad (5.40)$$

$$\sigma(F_L) = \int \int_{\text{bin}} dx dQ^2 \frac{2\pi\alpha^2}{xQ^4} Y_+ \frac{y^2}{Y_+} F_L(x, Q^2) \quad (5.41)$$

$$\sigma(F_3) = \int \int_{\text{bin}} dx dQ^2 \frac{2\pi\alpha^2}{xQ^4} Y_+ \frac{Y_-}{Y_+} F_3(x, Q^2) \quad (5.42)$$

and  $F_L$  is calculated by

$$F_L^{\text{QCD}} = \frac{4\alpha}{3\pi} x^2 \int_x^1 \frac{d\xi}{\xi^3} F_2(\xi, Q^2) + \frac{2\alpha}{\pi} \sum_f e_f^2 x^2 \int_x^1 \frac{d\xi}{\xi^3} \left(1 - \frac{x}{\xi}\right) \xi g(\xi, Q^2). \quad (5.43)$$

$F_3$  is calculated according to 1.39 and is negligible in all bins since the highest  $Q^2$  bins in this analysis reach up to 450 GeV<sup>2</sup> which is still below the  $Q^2$  range where the  $Z^0$  exchange starts to contribute significantly.

As the MC simulates QED radiation, the radiative corrections  $\delta_{RC}$  can be calculated from the MC via

$$\delta_{RC} = \frac{\hat{\sigma}}{\sigma_{\text{Born}}} - 1 \quad (5.44)$$

The correction contribution  $\delta_{\text{bin}}$  arises since the center of gravity of the data in a bin  $(x_{\text{mcgs}}, Q_{\text{mcgs}}^2)$  differs from the central value of the bin  $(x_{\text{ctr}}, Q_{\text{ctr}}^2)$  at which  $F_2$  is extracted and is calculated via

$$\delta_{\text{bin}} = \frac{\sigma(x_{\text{ctr}}, Q_{\text{ctr}}^2)}{(\sigma(x, Q^2))_{\text{bin}}} - 1 \quad (5.45)$$

## 5.6 Systematic Checks

The following systematic checks are applied

- The cut on the corrected electron energy is changed to 8 GeV (#1) and 10 GeV (#2). This checks the sensitivity to the electron identification at low energies. The changes in  $F_2$  are measured to be close to zero. Only for the highest  $y$  bins substantial deviation are seen which reach up to 12% for the high  $Q^2$  bins.
- The box cut is raised by 2 cm (#3) to check for the sensitivity of the measurement of the electron scattering angle and energy leakage. The changes are close to zero for all bins except the low  $y$  and low  $Q^2$  region where deviations up to 11% with an average of less than 3% are observed.
- The cut on  $y_{JB}$  is raised to 0.05 (#4) and lowered to 0.03 (#5) to check for the sensitivity to the calorimeter noise. The effect is in the order of 5 - 10% in the low  $y$  and low  $Q^2$  region and negligible elsewhere.
- The cut on  $y_{el}$  is lowered to 0.8 (#6). The effect is below 1% in all bins. The only exception is the lowest  $y$ - $Q^2$  bin with an effect of 9%.
- The  $E - P_z$  requirement is changed to  $\delta > 32$  GeV (#7) and  $\delta > 38$  GeV (#8). This checks the sensitivity of the measurement to the simulation of radiative events in the MC and the remaining photoproduction background in the bins. The changes of  $F_2$  are observed to be in the range of 5 - 10% in the highest  $y$  bins and less than 1% in the remaining region.
- The cut on the reconstructed vertex position is raised to  $-25 < z_{\text{vtx}} < 50$  cm (#9). This rejects all events originating from the satellite bunches. The influence is negligible with the exception of the lowest  $Q^2$  bins where 7 - 12% deviations are seen.
- The reconstructed uncorrected electron energy is scaled up (#10) and down by (#11) 1%. This probes the understanding of the electron energy correction method. The largest changes are registered at low  $Q^2$  with values up to 10%. In the remaining bins the effect is less than 4%.
- The electron finding efficiency is assumed to be inaccurate between the MC and the data. The deviation as seen for the SINISTRA finder in figure 4.21 is parameterized to  $1.17 - 0.027 \cdot E'_e + 0.0011 \cdot E'^2_e$  for electron energies below 12 GeV and the data events are reweighted accordingly (#12). The effect is less than 2% in all bins.
- The impact position of the electron is moved by 3 mm in  $y$  (#13) and  $x$  (#14). The influence is seen to be close to zero in all bins. Only the low  $y$ - $Q^2$  bins show a significant deviation.

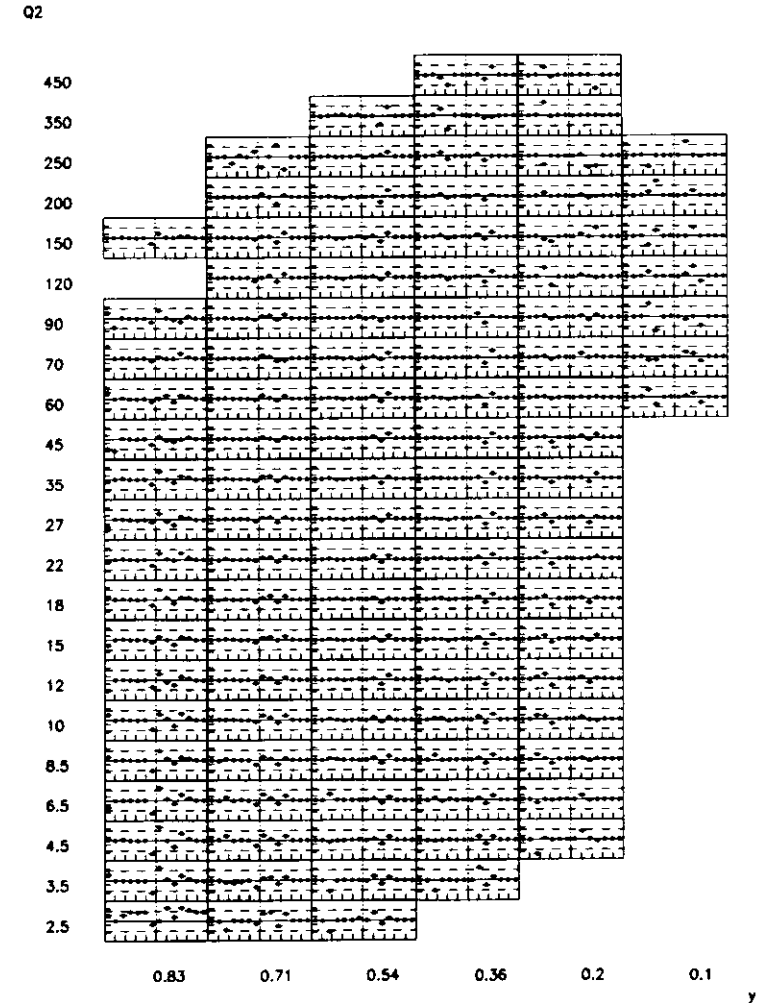


Figure 5.16: Systematics errors on the extraction of  $F_2$ . The relative deviation of  $F_2$  is shown for each bin in  $y$  and  $Q^2$  as a function of the number corresponding to one of the systematic conditions that were examined. The solid line corresponds to a deviation of 0% whereas the dashed line to a deviation of 10%.

The influence of the different systematic errors are summarized in figure 5.16 where the relative deviation of  $F_2$  on the different systematic variations is shown for each bin in the analysis. Additional systematic uncertainties originate from the error on the integrated luminosity which is estimated to be in the order of 1.5% [PZ95] and the uncertainty in the trigger efficiency in the order of 1%. Positive and negative contributions are added in quadrature giving asymmetric systematic errors.

## 5.7 Final Results

The values of  $F_2$  obtained by this analysis are summarized together with their systematic and statistical errors in tables A.1 – A.4 for all  $y$  and  $Q^2$  bins. Furthermore for each bin the number of observed events, estimated background events and the contribution from  $F_L$  are listed.

The final  $F_2$  values of this analysis plotted versus  $x$  for fixed values of  $Q^2$  are shown in figure 5.17 to 5.19 where they are compared to the recent  $F_2$  measurements of ZEUS [ZEU96a] and H1 [H1 96].

The different measurements are seen to be consistent within the statistical and systematic errors. The measurements of the published H1 analysis are obtained from the full 1994 data set including data from a shifted and from the nominal vertex position. Thus the H1 measurement is extended towards lower values of  $Q^2$  compared to the ZEUS measurements which is only shown for the nominal vertex position since the ZEUS low  $Q^2$  analysis [ZEU96b] was performed in slightly different  $Q^2$ -bins.

Due to the restriction to the ZEUS RCAL region the  $F_2$  values from the analysis presented only reach up to  $Q^2 = 450 \text{ GeV}^2$  whereas H1 and ZEUS use their full calorimeter and thus get measurements up to  $Q^2 = 5000 \text{ GeV}^2$ . Using the  $P_1$  method for the kinematic reconstruction the ZEUS measurement extends to lower values of  $y$  compared to this analysis and gives an overlap with fixed target experiments.

As the identification of the scattered electron could be improved in this analysis ( $E'_e > 6 \text{ GeV}$ ) compared to the ZEUS ( $E'_e > 10 \text{ GeV}$ ) measurements, the extraction of the structure function could be extended towards higher values of  $y$  and lower values of  $Q^2$ . Compared to the 1994 ZEUS nominal vertex  $F_2$  analysis where the lowest bin was at  $Q^2 = 3.5 \text{ GeV}^2$  and  $x = 6.5 \cdot 10^{-4}$ , this analysis reaches  $Q^2 = 2.5 \text{ GeV}^2$  and  $x = 4 \cdot 10^{-4}$ . The  $F_2$  values in the lowest  $Q^2$  bin of  $2.5 \text{ GeV}^2$  are seen to be in good agreement with the H1 measurements from the shifted vertex.

In all  $Q^2$  bins the measurements were extended towards very low values of  $x$  resp. high values of  $y$ . These data points confirm the steep rise of  $F_2$  for  $x < 10^{-3}$  which was the striking feature of the first  $F_2$  measurements at HERA.

The strong rise of  $F_2$  at low  $x$  results from the increasing gluon and thus parton density. Due to reasons mentioned in section 1.4 recombination and shadowing effects may occur, leading to a flattening of the  $F_2$  curves. This could not yet be seen in the data.

The data in figure 5.17 to 5.19 is shown together with the NLO prediction of GRV94 and the NLO parameterizations MRSA' and CTEQ3. At large values of  $Q^2$  all parameterizations represent the data well.

The MRSA' parameterization gives a good description of the data also for small values of  $Q^2$  whereas the CTEQ3 parameterization overshoots the data in the region of  $Q^2 < 22 \text{ GeV}^2$  and  $x < 10^{-3}$ .

The GRV94 parton distributions has a very low starting value of  $Q_0^2 = 0.3 \text{ GeV}^2$  for the DGLAP evolution equation and the steep rise in  $F_2$  at low  $x$  is generated dynamically by the

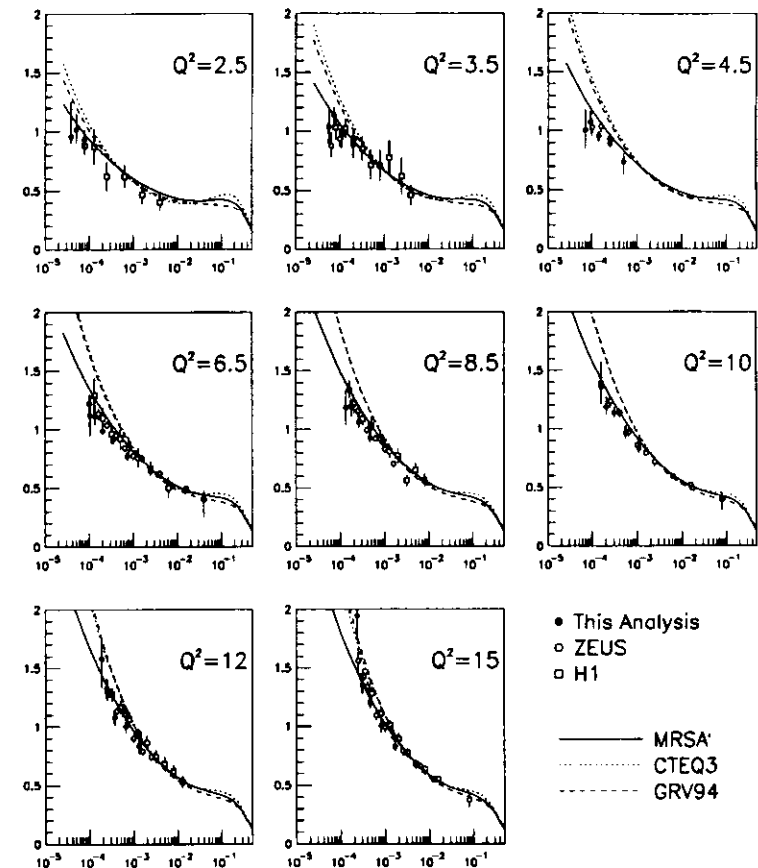


Figure 5.17:  $F_2$  obtained by this analysis as a function of  $x$  for fixed  $Q^2$  in the low  $Q^2$ -bins (closed circles). The recent ZEUS and H1 measurements are shown as the open circles resp. open squares. These data points are only shown if they were extracted at the same central value of  $Q^2$  as in this analysis.

evolution in  $Q^2$ . GRV94 also overshoots the data at the low  $Q^2$  bins.

The HERA and fixed target experiments now cover a large region of the  $x$  and  $Q^2$  phase space, running over five orders of magnitude in  $Q^2$  and four orders of magnitude in  $x$ . All the measured structure functions agree well with each other in the regions of overlap and with

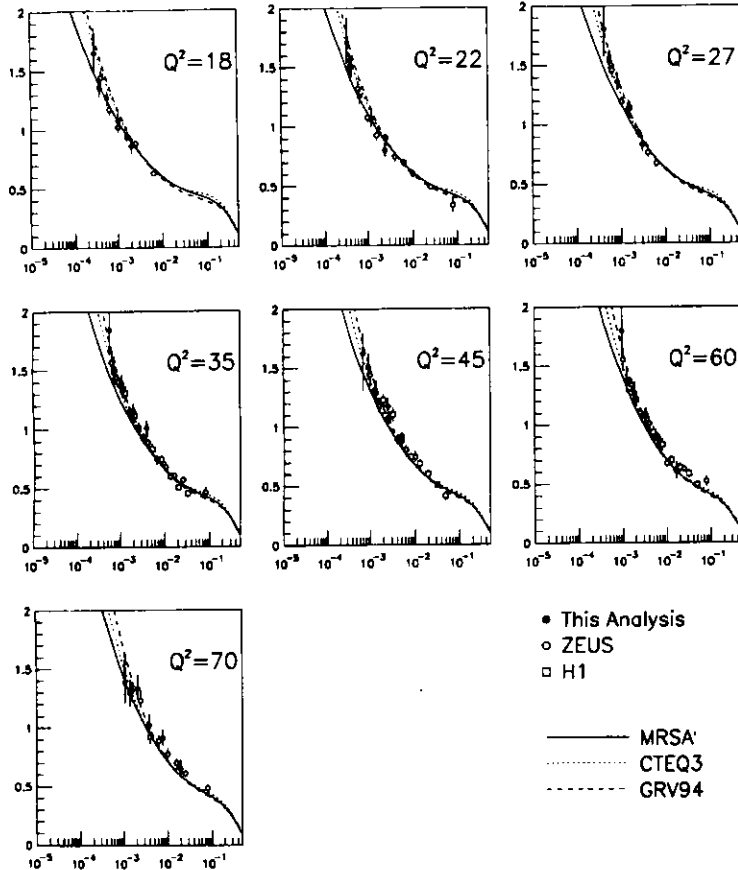


Figure 5.18:  $F_2$  obtained by this analysis as a function of  $x$  for fixed  $Q^2$  in the medium  $Q^2$ -bins (closed circles). The recent ZEUS and H1 measurements are shown as the open circles resp. open squares. These data points are only shown if they were extracted at the same central value of  $Q^2$  as in this analysis.

perturbative QCD predictions [BDR96]. This means that by giving only one input parton parameterization at some reference point  $Q_0^2$  the  $Q^2$ -evolution of the parton densities are calculable over several orders of magnitude by applying conventional leading twist NLO perturbative QCD evolution. This is a great success of QCD and puts tight constraints on the size of novel

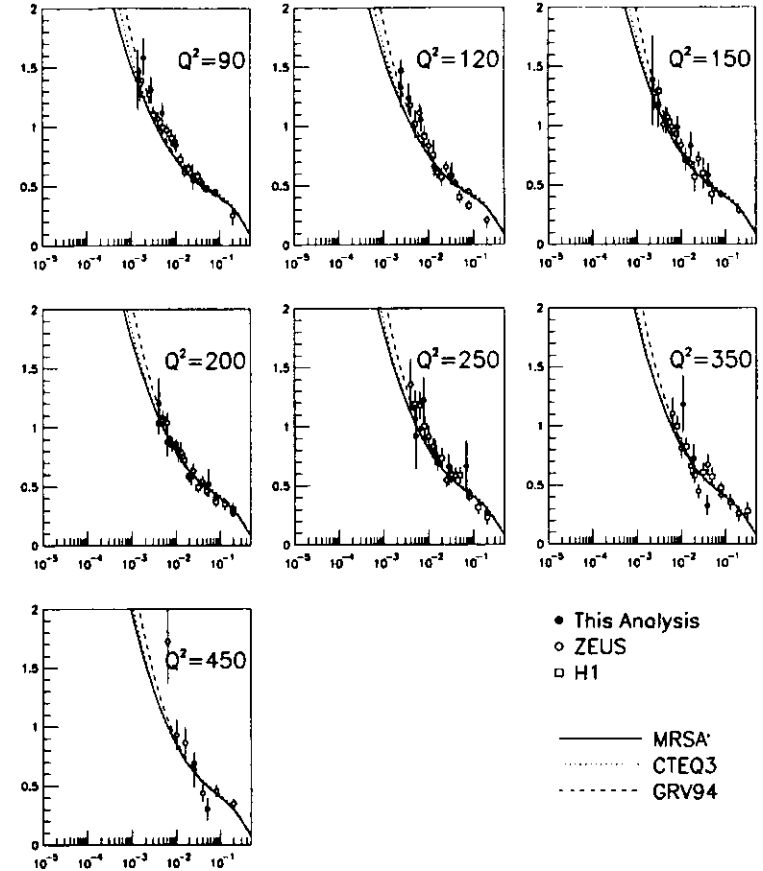


Figure 5.19:  $F_2$  obtained by this analysis as a function of  $x$  for fixed  $Q^2$  in the high  $Q^2$ -bins (closed circles). The recent ZEUS and H1 measurements are shown as the open circles resp. open squares. These data points are only shown if they were extracted at the same central value of  $Q^2$  as in this analysis.

effects such as BFKL logarithms (i.e. leading orders) and parton recombinations (i.e. higher twists).

At small  $x$  conventional perturbation theory is eventually expected to break down due to the large logarithms of  $1/x$ . These contributions may be summed up by the BFKL equation

giving a gluon distribution which rises approximately as  $x^{-0.5}$ . An interesting comparison with the HERA data, which starts doubt on the validity of BFKL in the  $x$ -region investigated so far, has been carried out by [BF94b, BF94a].

The effects of higher twists are estimated by rerunning the perturbative NLO fits to the  $F_2$  data using

$$F_2(x, Q^2) = F_2^{\text{NLO}}(x, Q^2) \cdot (1 + D_2(x)/Q^2) \quad (5.46)$$

and fitting  $D_2(x)$  in various bins in  $x$ .

Recent fits to the HERA data [BF] give  $D_2 \simeq 0.2 \pm 0.2 \text{ GeV}^2$  for  $10^{-4} < x < 10^{-2}$ . It seems that except for large  $x$  values the characteristic scale for higher twists is no more than a few hundred MeV.

## Conclusion

The structure function  $F_2$  has been determined in an independent analysis using the Hadron Electron Separator. It allowed to check and improve the identification of low energy scattered electrons by combining the HES information with the ZEUS neural network electron finder SINISTRA. Using this combination it became possible to identify scattered electrons with a high purity with energies down to 6 GeV.

Using the two electron finder algorithms, the electron identification efficiency and the photoproduction background was checked independent of MC.

Using this improved electron identification the proton structure function was extracted with a focus on the high  $y$  region. No significant difference to the published H1 and ZEUS measurements was observed in the region of overlap and the range of the  $F_2$  measurement could be extended into the region of smaller values of  $x$  ( $4 \cdot 10^{-5}$ ) and  $Q^2$  ( $2.5 \text{ GeV}^2$ ) compared to the nominal vertex ZEUS measurement ( $x = 6.5 \cdot 10^{-5}$  at  $Q^2 = 3.5 \text{ GeV}^2$ ). In all  $Q^2$  bins higher values of  $y$  resp. lower values of  $x$  have been reached. These data point confirm the steep rise of  $F_2$  at fixed  $Q^2$  as  $x$  decreases.

The capability to extend the measurements to small energies of the scattered electron will be important for a measurement of  $F_L$  which has to be extracted at high values of  $y$ .

# Acknowledgment

This thesis was prepared in the environment of the ZEUS collaboration and I would like to thank all its members for fruitful discussions and cooperation. Working in the atmosphere of a large international collaboration has been an invaluable experience. But now to those persons to whom I own special thanks:

First of all I would like to thank my advisor Prof. Dr. E. Lohrmann for giving me the opportunity to work on this thesis within the ZEUS collaboration and his excellent guidance, support and advice during its preparation.

Thanks go to Dr. R. Klanner for valuable comments after reading the draft of this thesis.

Thanks to the members of the ZEUS Expert System group Ulf Behrens, Lars Hagge, Janusz Jurek and Dirk Kahnert. Working together with them on a field not related to high energy physics was fascinating and made it hard to return to physics topics. I highly enjoyed the atmosphere in this group.

Thanks to Johannes Mainusch, Dirk Westphal and once more Lars Hagge and Dirk Kahnert. It has been fun to share the office with them. At this point I would like to thank Lars Hagge for allowing me to reuse some of his programs which prevented me from reinventing the wheel over and over again.

Special thanks to my parents for all they have done for me in my life and their financial support during my physics studies, allowing me to reach the point were I am now.

Finally I am most grateful to my wife Tanja for her patience and support during the last years. She has made even the few darker times bright, my life wonderful and the last years the best years of my life!

# Appendix A

## Tables

$x$	$Q^2$	$F_2$	$\pm\text{stat}$	$\pm\text{syst}$	$N_{\text{obs}}$	$N_{\text{php}}$	$\sigma$	$\pm\text{stat}$	$\delta F_L$ [%]
0.00008	2.5	$0.938 \pm 0.030$	$\pm 0.074$	$\pm 0.112$	1701	0	$27.501 \pm 0.888$		1.8
0.00005	2.5	$1.022 \pm 0.025$	$\pm 0.132$	$\pm 0.115$	3871	134	$19.841 \pm 0.490$		4.7
0.00004	2.5	$0.959 \pm 0.043$	$\pm 0.295$	$\pm 0.035$	1257	269	$12.633 \pm 0.573$		9.0
0.00019	3.5	$0.883 \pm 0.032$	$\pm 0.118$	$\pm 0.102$	1481	0	$19.033 \pm 0.682$		0.4
0.00011	3.5	$0.976 \pm 0.025$	$\pm 0.051$	$\pm 0.111$	3896	0	$11.062 \pm 0.281$		1.6
0.00007	3.5	$1.139 \pm 0.029$	$\pm 0.080$	$\pm 0.094$	4362	58	$8.159 \pm 0.209$		4.3
0.00005	3.5	$1.039 \pm 0.061$	$\pm 0.159$	$\pm 0.133$	737	82	$6.353 \pm 0.374$		8.4
0.00050	4.5	$0.742 \pm 0.028$	$\pm 0.085$	$\pm 0.105$	1449	0	$21.791 \pm 0.829$		0.1
0.00025	4.5	$0.901 \pm 0.021$	$\pm 0.044$	$\pm 0.037$	4671	0	$14.884 \pm 0.344$		0.4
0.00014	4.5	$0.959 \pm 0.020$	$\pm 0.036$	$\pm 0.043$	7428	0	$7.631 \pm 0.155$		1.6
0.00009	4.5	$1.078 \pm 0.029$	$\pm 0.088$	$\pm 0.065$	4017	80	$5.657 \pm 0.151$		4.1
0.00007	4.5	$1.010 \pm 0.062$	$\pm 0.157$	$\pm 0.147$	653	72	$4.304 \pm 0.265$		8.0
0.00072	6.5	$0.770 \pm 0.015$	$\pm 0.030$	$\pm 0.026$	6788	0	$20.570 \pm 0.394$		0.1
0.00036	6.5	$0.920 \pm 0.014$	$\pm 0.045$	$\pm 0.036$	12458	0	$12.247 \pm 0.189$		0.4
0.00020	6.5	$0.990 \pm 0.018$	$\pm 0.066$	$\pm 0.027$	9573	0	$7.421 \pm 0.133$		1.5
0.00013	6.5	$1.111 \pm 0.027$	$\pm 0.083$	$\pm 0.061$	4611	121	$6.283 \pm 0.155$		3.8
0.00010	6.5	$1.123 \pm 0.061$	$\pm 0.157$	$\pm 0.169$	846	92	$4.988 \pm 0.272$		7.3
0.00094	8.5	$0.876 \pm 0.020$	$\pm 0.043$	$\pm 0.040$	5154	0	$7.988 \pm 0.180$		0.1
0.00047	8.5	$0.927 \pm 0.019$	$\pm 0.062$	$\pm 0.036$	7005	0	$5.843 \pm 0.120$		0.4
0.00026	8.5	$1.061 \pm 0.026$	$\pm 0.051$	$\pm 0.034$	4989	29	$4.016 \pm 0.099$		1.4
0.00017	8.5	$1.196 \pm 0.038$	$\pm 0.048$	$\pm 0.075$	2784	64	$3.456 \pm 0.110$		3.7
0.00013	8.5	$1.184 \pm 0.078$	$\pm 0.131$	$\pm 0.133$	607	70	$2.886 \pm 0.190$		7.1
0.00111	10.0	$0.836 \pm 0.024$	$\pm 0.044$	$\pm 0.040$	3090	0	$4.736 \pm 0.137$		0.1
0.00055	10.0	$0.962 \pm 0.025$	$\pm 0.056$	$\pm 0.035$	4286	0	$3.639 \pm 0.095$		0.4
0.00031	10.0	$1.134 \pm 0.034$	$\pm 0.036$	$\pm 0.023$	3233	0	$2.681 \pm 0.081$		1.4
0.00021	10.0	$1.181 \pm 0.048$	$\pm 0.081$	$\pm 0.039$	1728	45	$2.102 \pm 0.085$		3.5
0.00016	10.0	$1.390 \pm 0.103$	$\pm 0.149$	$\pm 0.155$	480	36	$1.903 \pm 0.140$		6.9

Table A.1:  $F_2(x, Q^2)$  as obtained from this analysis where the data was binned in  $y$  and  $Q^2$ , reconstructed using the electron only method, and unfolded via an iterative method.

$x$	$Q^2$	$F_2$	$\pm\text{stat}$	$\pm\text{syst}$	$N_{\text{obs}}$	$N_{\text{php}}$	$\sigma$	$\pm\text{stat}$	$\delta F_L$ [%]
0.00133	12.0	0.837	$\pm 0.029$	$\pm 0.048$	2237	0	3.100	$\pm 0.106$	0.1
0.00066	12.0	1.006	$\pm 0.031$	$\pm 0.053$	3078	0	2.610	$\pm 0.081$	0.4
0.00037	12.0	1.080	$\pm 0.040$	$\pm 0.050$	2153	0	1.799	$\pm 0.066$	1.3
0.00025	12.0	1.326	$\pm 0.062$	$\pm 0.061$	1289	31	1.623	$\pm 0.076$	3.4
0.00019	12.0	1.578	$\pm 0.125$	$\pm 0.114$	418	25	1.368	$\pm 0.108$	6.7
0.00166	15.0	0.829	$\pm 0.028$	$\pm 0.041$	2351	0	3.151	$\pm 0.105$	0.1
0.00083	15.0	1.005	$\pm 0.031$	$\pm 0.049$	3068	0	2.767	$\pm 0.085$	0.3
0.00046	15.0	1.200	$\pm 0.043$	$\pm 0.049$	2282	0	2.010	$\pm 0.072$	1.3
0.00031	15.0	1.348	$\pm 0.060$	$\pm 0.065$	1432	28	1.745	$\pm 0.077$	3.3
0.00023	15.0	1.942	$\pm 0.136$	$\pm 0.085$	520	8	1.977	$\pm 0.139$	6.4
0.00199	18.0	0.859	$\pm 0.031$	$\pm 0.024$	2007	0	2.765	$\pm 0.100$	0.1
0.00100	18.0	1.074	$\pm 0.036$	$\pm 0.057$	2557	0	2.451	$\pm 0.082$	0.3
0.00055	18.0	1.267	$\pm 0.049$	$\pm 0.022$	1937	0	1.932	$\pm 0.074$	1.2
0.00037	18.0	1.355	$\pm 0.063$	$\pm 0.071$	1288	23	1.495	$\pm 0.070$	3.2
0.00028	18.0	1.640	$\pm 0.131$	$\pm 0.176$	469	85	1.139	$\pm 0.091$	6.2
0.00244	22.0	0.801	$\pm 0.034$	$\pm 0.049$	1456	0	2.107	$\pm 0.089$	0.1
0.00122	22.0	1.066	$\pm 0.040$	$\pm 0.048$	2003	0	2.044	$\pm 0.077$	0.3
0.00068	22.0	1.260	$\pm 0.055$	$\pm 0.056$	1531	0	1.465	$\pm 0.064$	1.2
0.00045	22.0	1.508	$\pm 0.076$	$\pm 0.058$	1143	11	1.258	$\pm 0.063$	3.1
0.00034	22.0	1.713	$\pm 0.139$	$\pm 0.160$	405	16	0.926	$\pm 0.075$	6.0
0.00299	27.0	0.831	$\pm 0.036$	$\pm 0.031$	1362	0	2.046	$\pm 0.089$	0.1
0.00150	27.0	1.131	$\pm 0.045$	$\pm 0.058$	1845	0	1.811	$\pm 0.071$	0.3
0.00083	27.0	1.359	$\pm 0.061$	$\pm 0.052$	1463	0	1.347	$\pm 0.060$	1.1
0.00055	27.0	1.536	$\pm 0.082$	$\pm 0.048$	1004	8	1.119	$\pm 0.060$	3.0
0.00042	27.0	1.804	$\pm 0.148$	$\pm 0.115$	397	7	0.799	$\pm 0.065$	5.9

Table A.2:  $F_2(x, Q^2)$  as obtained from this analysis where the data was binned in  $y$  and  $Q^2$ , reconstructed using the electron only method, and unfolded via an iterative method (cont'd).

$x$	$Q^2$	$F_2$	$\pm\text{stat}$	$\pm\text{syst}$	$N_{\text{obs}}$	$N_{\text{php}}$	$\sigma$	$\pm\text{stat}$	$\delta F_L$ [%]
0.00388	35.0	1.008	$\pm 0.049$	$\pm 0.043$	1153	0	1.596	$\pm 0.077$	0.1
0.00194	35.0	1.148	$\pm 0.052$	$\pm 0.053$	1360	0	1.389	$\pm 0.063$	0.3
0.00108	35.0	1.386	$\pm 0.073$	$\pm 0.061$	1062	0	0.968	$\pm 0.051$	1.1
0.00072	35.0	1.501	$\pm 0.096$	$\pm 0.083$	705	12	0.701	$\pm 0.045$	2.9
0.00055	35.0	1.839	$\pm 0.168$	$\pm 0.156$	342	6	0.626	$\pm 0.057$	5.6
0.00499	45.0	0.871	$\pm 0.047$	$\pm 0.044$	929	0	1.217	$\pm 0.065$	0.1
0.00249	45.0	1.175	$\pm 0.058$	$\pm 0.050$	1197	0	1.195	$\pm 0.059$	0.3
0.00138	45.0	1.293	$\pm 0.074$	$\pm 0.085$	877	0	0.841	$\pm 0.048$	1.1
0.00092	45.0	1.510	$\pm 0.104$	$\pm 0.034$	622	7	0.615	$\pm 0.042$	2.8
0.00070	45.0	1.620	$\pm 0.172$	$\pm 0.045$	255	12	0.406	$\pm 0.043$	5.4
0.01662	60.0	0.616	$\pm 0.050$	$\pm 0.056$	327	0	5.387	$\pm 0.438$	0.0
0.00665	60.0	0.873	$\pm 0.049$	$\pm 0.011$	841	0	1.123	$\pm 0.063$	0.1
0.00332	60.0	1.076	$\pm 0.056$	$\pm 0.045$	1082	0	0.978	$\pm 0.051$	0.3
0.00185	60.0	1.270	$\pm 0.077$	$\pm 0.082$	799	0	0.714	$\pm 0.043$	1.0
0.00123	60.0	1.380	$\pm 0.100$	$\pm 0.059$	533	2	0.568	$\pm 0.041$	2.6
0.00094	60.0	1.794	$\pm 0.195$	$\pm 0.140$	242	1	0.398	$\pm 0.043$	5.1
0.01939	70.0	0.650	$\pm 0.065$	$\pm 0.039$	216	0	4.148	$\pm 0.413$	0.0
0.00775	70.0	0.912	$\pm 0.060$	$\pm 0.036$	637	0	0.816	$\pm 0.053$	0.1
0.00388	70.0	1.019	$\pm 0.061$	$\pm 0.072$	804	0	0.695	$\pm 0.042$	0.3
0.00215	70.0	1.333	$\pm 0.091$	$\pm 0.072$	631	0	0.557	$\pm 0.038$	1.0
0.00144	70.0	1.295	$\pm 0.107$	$\pm 0.025$	414	3	0.394	$\pm 0.033$	2.6
0.00109	70.0	1.384	$\pm 0.171$	$\pm 0.046$	173	0	0.320	$\pm 0.040$	5.0
0.02493	90.0	0.589	$\pm 0.070$	$\pm 0.077$	149	0	2.328	$\pm 0.276$	0.0
0.00997	90.0	0.872	$\pm 0.064$	$\pm 0.024$	496	0	0.633	$\pm 0.047$	0.1
0.00499	90.0	1.120	$\pm 0.075$	$\pm 0.044$	677	0	0.549	$\pm 0.037$	0.3
0.00277	90.0	1.317	$\pm 0.106$	$\pm 0.021$	440	0	0.410	$\pm 0.033$	1.0
0.00185	90.0	1.584	$\pm 0.146$	$\pm 0.073$	338	0	0.336	$\pm 0.031$	2.5
0.00140	90.0	1.400	$\pm 0.212$	$\pm 0.137$	122	0	0.205	$\pm 0.031$	4.9

Table A.3:  $F_2(x, Q^2)$  as obtained from this analysis where the data was binned in  $y$  and  $Q^2$ , reconstructed using the electron only method, and unfolded via an iterative method (cont'd).

$x$	$Q^2$	$F_2$	$\pm_{\text{stat}}$	$\pm_{\text{syst}}$	$N_{\text{obs}}$	$N_{\text{php}}$	$\sigma$	$\pm_{\text{stat}}$	$\delta F_L$ [%]
0.03324	120.0	0.590±0.084± <sup>0.068</sup> <sub>0.028</sub>			110	0	1.423±0.202		0.0
0.01329	120.0	0.656±0.062± <sup>0.061</sup> <sub>0.055</sub>			292	0	0.324±0.031		0.1
0.00665	120.0	1.055±0.086± <sup>0.062</sup> <sub>0.053</sub>			462	0	0.377±0.031		0.2
0.00369	120.0	1.233±0.118± <sup>0.047</sup> <sub>0.027</sub>			320	0	0.292±0.028		0.9
0.00246	120.0	1.325±0.154± <sup>0.061</sup> <sub>0.063</sub>			226	0	0.187±0.022		2.4
0.04154	150.0	0.581±0.085± <sup>0.058</sup> <sub>0.052</sub>			99	0	1.282±0.188		0.0
0.01662	150.0	0.833±0.081± <sup>0.077</sup> <sub>0.048</sub>			282	0	0.370±0.036		0.1
0.00831	150.0	0.985±0.087± <sup>0.048</sup> <sub>0.027</sub>			382	0	0.316±0.028		0.2
0.00462	150.0	1.047±0.106± <sup>0.043</sup> <sub>0.049</sub>			283	2	0.256±0.026		0.9
0.00308	150.0	1.157±0.160± <sup>0.055</sup> <sub>0.056</sub>			154	0	0.137±0.019		2.3
0.00234	150.0	1.386±0.375± <sup>0.064</sup> <sub>0.085</sub>			32	0	0.135±0.036		4.5
0.05539	200.0	0.517±0.102± <sup>0.064</sup> <sub>0.001</sub>			56	0	0.614±0.121		0.0
0.02216	200.0	0.581±0.076± <sup>0.021</sup> <sub>0.010</sub>			152	0	0.190±0.025		0.1
0.01108	200.0	0.790±0.084± <sup>0.020</sup> <sub>0.029</sub>			267	0	0.235±0.025		0.2
0.00615	200.0	0.876±0.112± <sup>0.053</sup> <sub>0.049</sub>			189	0	0.176±0.022		0.9
0.00410	200.0	1.202±0.212± <sup>0.043</sup> <sub>0.084</sub>			86	0	0.116±0.020		2.3
0.06924	250.0	0.662±0.195± <sup>0.090</sup> <sub>0.073</sub>			25	0	0.540±0.159		0.0
0.02770	250.0	0.658±0.105± <sup>0.008</sup> <sub>0.118</sub>			101	0	0.138±0.022		0.1
0.01385	250.0	0.780±0.104± <sup>0.032</sup> <sub>0.043</sub>			175	0	0.136±0.018		0.2
0.00769	250.0	1.220±0.184± <sup>0.055</sup> <sub>0.012</sub>			135	0	0.132±0.020		0.8
0.00513	250.0	0.919±0.233± <sup>0.120</sup> <sub>0.161</sub>			39	4	0.121±0.031		2.2
0.03877	350.0	0.323±0.078± <sup>0.043</sup> <sub>0.103</sub>			38	0	0.073±0.018		0.0
0.01939	350.0	0.724±0.112± <sup>0.047</sup> <sub>0.098</sub>			136	0	0.152±0.024		0.2
0.01077	350.0	1.182±0.222± <sup>0.111</sup> <sub>0.111</sub>			84	0	0.167±0.031		0.8
0.04985	450.0	0.302±0.095± <sup>0.024</sup> <sub>0.040</sub>			23	0	0.048±0.015		0.0
0.02493	450.0	0.638±0.136± <sup>0.053</sup> <sub>0.070</sub>			65	0	0.139±0.030		0.2

Table A.4:  $F_2(x, Q^2)$  as obtained from this analysis where the data was binned in  $y$  and  $Q^2$ , reconstructed using the electron only method, and unfolded via an iterative method.

## Bibliography

- [A91a] C. Alvisi et al.: The ZEUS Vertex Detector: Design and Prototype. *Nucl. Inst. Meth. A* 305 (1991) 30 – 38
- [A91b] A. Andresen et al.: Construction and Beam Test of the ZEUS Forward and Rear Calorimeter. *Nucl. Inst. Meth. A* 309 (1991) 101 – 142
- [A92] J. Andruszkow et al.: First Measurement of HERA Luminosity by ZEUS Lumi Monitor. *DESY 92-066* (1992)
- [ACS95] H. Abramowicz, A. Caldwell, and R. Sinkus: Neural Network Based Electron Identification in the ZEUS Calorimeter. *Nucl. Inst. Meth. A* 365 (1995) 508 – 517
- [ADKT85] Ya. I. Azimov, Yu. L. Dokshitser, V. A. Khoze, and S. I. Troian: The String Effect and QCD Coherence. *Phys. Lett. B* 165 (1985) 147 – 150
- [AGLP89] B. Andersson, G. Gustafson, Lonnblad L., and U. Pettersson: Coherence Effects in Deep Inelastic Scattering. *Z. Phys. C* 43 (1989) 625
- [AP77] G. Altarelli and G. Parisi: Asymptotic Freedom in Parton Language. *Nucl. Phys. B* 126 (1977) 298 – 318
- [ASV96] H. Abramowicz, R. Sinkus, and T. Voss: Upgrade of the Neural Network Electron Finder for the '95 Data Taking at ZEUS. Technical report. ZEUS-Note. 1996. (in preparation)
- [B68] W. Bartel et al.: Electroproduction of Pions near the  $\Delta(1236)$  Isobar and the Form Factor  $G_M^*(q^2)$  of the  $(\gamma N\Delta)$ -Vertex. *Phys. Lett. B* 28 (1968) 148 – 151
- [B69a] E. D. Bloom et al.: High-Energy Inelastic e-p Scattering at  $6^\circ$  and  $10^\circ$ . *Phys. Rev. Lett.* 23 (1969) 930 – 934
- [B69b] M. Breidenbach et al.: Observed Behavior of Highly Inelastic Electron-Proton Scattering. *Phys. Rev. Lett.* 23 (1969) 935 – 939
- [B79] A. Bodek et al.: Experimental Studies of the Neutron and Proton Electromagnetic Structure Functions. *Phys. Rev. D* 20 (1979) 1471 – 1552
- [B87] R. Brun et al.: GEANT 3.13. Technical report. CERN DD/EE/841. 1987
- [B92] A. Bodek et al.: Precise Measurements of the Proton and Deuteron Structure Functions from a Global Analysis of the SLAC Deep Inelastic Electron Scattering Cross Sections. *Phys. Lett. B* 282 (1992) 475 – 482

- [B93a] A. Bernstein et al.: Beam Test of the ZEUS Barrel Calorimeter. *Nucl. Inst. Meth. A* 336 (1993) 23 - 52
- [B93b] J. Botts et al.: CTEQ Parton Distributions and Flavor Dependence of Sea Quarks. *Phys. Lett. B* 304 (1993) 159 - 166
- [BB94] U. Bassler and G. Bernardi: On the Kinematic Reconstruction of Deep Inelastic Scattering at HERA: The Sigma Method. *DESY* 94-231 (1994)
- [BCD89] BCDMS Collaboration (A. C. Benvenuti et al.): A High Statistics Measurement of the Proton Structure Functions  $F_2(x, Q^2)$  and  $R$  from Deep Inelastic Muon Scattering at High  $Q^2$ . *Phys. Lett. B* 223 (1989) 485 - 489
- [BDR96] R. D. Ball and A. De Roeck: Structure Functions. *DESY* 96-185 (1996). - (hep-ph/9609309) to be published in the Proceedings of the Workshop on Deep Inelastic Scattering and Related Phenomena, Rome, Italy, April 1996
- [BEK91] S. Bentvelsen, J. Engelen, and P. Kooijman: Reconstruction of  $(x, Q^2)$  and Extraction of Structure Functions in Neutral Current Scattering at HERA. In W. Buchmüller and G. Ingelmann, editors, *Physics at HERA*. volume 1. 23. Proceedings of the Workshop held at DESY, Hamburg. October 29 - 30, 1991
- [BF] R. D. Ball and S. Forte: Double Scaling Violations. (hep-ph/9609309) to be published in the Proceedings of the Workshop on Deep Inelastic Scattering and Related Phenomena, Rome, Italy, April 1996
- [BF94a] R. D. Ball and S. Forte: A Direct Test of Perturbative QCD at Small  $x$ . *Phys. Lett. B* 336 (1994) 77 - 79
- [BF94b] R. D. Ball and S. Forte: Double Asymptotic Scaling at HERA. *Phys. Lett. B* 335 (1994) 77 - 86
- [BFH92] U. Behrens, M. Flasinski, and L. Hagge: ZEXP - Expert System for ZEUS: Problem Analysis, Theoretical Background and First Results. *DESY* 92-141 (1992)
- [BFH96] U. Behrens, M. Flasinski, L. Hagge, J. Jurek, and K. Ohrenberg: Recent Developments of the ZEUS Expert System ZEX. *IEEE Trans. Nuc. Sci.* 43 (1996) 65 - 68
- [BFHO94] U. Behrens, M. Flasinski, L. Hagge, and K. Ohrenberg: ZEX - An Expert System for ZEUS. *IEEE Trans. Nuc. Sci.* 41 (1994) 152 - 156
- [BHV93] U. Behrens, L. Hagge, and W. Vogel: The Eventbuilder of the ZEUS Experiment. *Nucl. Inst. Meth. A* 332 (1993) 253 - 262
- [Bjo69] J. D. Bjorken: Asymptotic Sum Rules at Infinite Momentum. *Phys. Rev.* 179 (1969) 1547 - 1553
- [BL78] Ya. Ya. Balitskii and L. N. Lipatov: The Pomernchuk Singularity in Quantum Chromodynamics. *Sov. J. Nucl. Phys.* 28 (1978) 822 - 829
- [CG69] C. G. Callan and D. J. Gross: High-Energy Electroproduction and the Constitution of the Electric Current. *Phys. Rev. Lett.* 22 (1969) 156 - 159

- [CH56] E. E. Chambers and R. Hofstadter: Structure of the Proton. *Phys. Rev.* 103 (1956) 1454 - 1463
- [CR92] A. Caldwell and J. Repond: EEXOTIC. 1992. Algorithm to find the most likely scattered electron, ZEUS PHANTOM program library
- [D91] M. Derrick et al.: Design and Construction of the ZEUS Barrel Calorimeter. *Nucl. Inst. Meth. A* 309 (1991) 77 - 100
- [Doe95] T. Doeker: ELECPO. 1995. Algorithm to calculate the position of the scattered electron, ZEUS PHANTOM program library
- [Dok77] Yu. L. Dokshitzer: Calculation of Structure Functions of Deep-Inelastic Scattering and  $e^+e^-$  Annihilation by Perturbation Theory in Quantum Chromodynamics. *Sov. Phys. JETP* 46 (1977) 641 - 653
- [DW64] S. D. Drell and J. D. Walecka: Electrodynamic Processes with Nuclear Targets. *Ann. Phys.* 28 (1964) 18 - 33
- [EMC87] EMC Collaboration (J. J. Aubert et al.): Measurements of the Nucleon Structure Functions  $F_2^N$  in Deep Inelastic Muon Scattering from Deuterium and Comparison with those from Hydrogen and Iron. *Nucl. Phys. B* 293 (1987) 740 - 786
- [EZ96] A. Ebel and F. Zetsche: Analysis of Elastic QED Compton Scattering Events using the 1994 ZEUS Data. Technical Report 96-020. ZEUS-Note. 1996
- [F94] B. Foster et al.: The Design and Construction of the ZEUS Central Tracking Detector. *Nucl. Inst. Meth. A* 338 (1994) 254 - 283
- [Fey69] R. P. Feynman: Very High-Energy Collisions of Hadrons. *Phys. Rev. Lett.* 23 (1969) 1415 - 1417
- [FK72] J. I. Friedman and H. W. Kendall: Deep Inelastic Electron Scattering. *Ann. Rev. Nucl. Science* 22 (1972) 203 - 254
- [Fle94] I. Fleck: *Nachweis von Elektronen aus der e-p Streuung mit dem Hadron-Elektron-Separator im ZEUS-Experiment*, University of Hamburg, PhD thesis, 1991. (in German)
- [FO95] I. Fleck and K. Ohrenberg: Electron Identification in the HES and a new way to determine the efficiency of electron finders. Technical report. ZEUS 95-009. 1995
- [Fri91] J. I. Friedman: Deep Inelastic Scattering: Comparison with the Quark Model. *Rev. Mod. Phys.* 63 (1991) 615 - 627. Lecture delivered on the occasion of the presentation of the 1990 Nobel Prize in Physics
- [Fro61] M. Froissart: Asymptotic Behavior and Subtractions in the Mandelstam Representation. *Phys. Rev.* 123 (1961) 1053 - 1057
- [GL72] V. N. Gribov and L. N. Lipatov: Deep Inelastic  $ep$  Scattering in Perturbation Theory. *Sov. J. Nucl. Phys.* 15 (1972) 438 - 450

- [GLR81] L. V. Gribov, E. M. Levin, and M. G. Ryskin: Singlet Structure Function at Small  $x$ : Unitarization of Gluon Ladders. *Nucl. Phys. B* 188 (1981) 555 - 576
- [GM09] H. Geiger and E. Marsden: On a Diffuse Reflection of the  $\alpha$ -Particles. *Proc. Roy. Soc.* 82 (1909) 495 - 500
- [GM64] M. Gell-Mann: A Schematic Model of Baryons and Mesons. *Phys. Lett.* 8 (1964) 214 - 215
- [GP88] G. Gustafson and U. Pettersson: Dipole Formulation of QCD Cascades. *Nucl. Phys. B* 306 (1988) 746
- [GR77] M. Glück and E. Reya: Dynamical Determination of Parton and Gluon Distributions in Quantum Chromodynamics. *Nucl. Phys. B* 130 (1977) 76 - 92
- [GRV90] M. Glück, E. Reya, and A. Vogt: Radiatively Generated Parton Distributions for High Energy Collisions. *Z. Phys. C* 48 (1990) 471 - 482
- [GRV95] M. Glück, E. Reya, and A. Vogt: Dynamical Parton Distributions of the Proton and Small- $x$  Physics. *Z. Phys. C* 67 (1995) 433 - 447
- [Gus86] G. Gustafson: Dual Description of a Confined Color Field. *Phys. Lett. B* 175 (1986) 453
- [H1 93a] H1 Collaboration: The H1 Detector at HERA. *DESY* 93-103 (1993)
- [H1 93b] H1 Collaboration: Measurement of the Proton Structure Function  $F_2(x, Q^2)$  in the Low  $x$  Region at HERA. *Nucl. Phys. B* 407 (1993) 515 - 538
- [H1 94] H1 Collaboration: Deep Inelastic Scattering Events with a Large Rapidity Gap at HERA. *Nucl. Phys. B* 429 (1994) 477 - 502
- [H1 95] H1 Collaboration: A Measurement of the Proton Structure Function  $F_2(x, Q^2)$ . *Nucl. Phys. B* 439 (1995) 471 - 502
- [H1 96] H1 Collaboration: A Measurement and QCD Analysis of the Proton Structure Function  $F_2(X, Q^2)$  at HERA. *Nucl. Phys. B* 470 (1996) 3 - 40
- [Hag95] L. Hagge: *A Measurement of the Proton Structure Function  $F_2$  with the ZEUS Detector at HERA*, University of Hamburg, PhD thesis, 1995
- [Han63] L. N. Hand: Experimental Investigation of Pion Electroproduction. *Phys. Rev.* 129 (1963) 1834 - 1846
- [HER93] HERMES Collaboration: Technical Design Report. *DESY PRC* 93/06 (1993)
- [HER94] HERA-B Collaboration: HERA-B, An Experiment to Study CP Violation at the HERA Proton Ring Using An Internal Target. *Nucl. Inst. Meth. A* 351 (1994) 111 - 131
- [HFM53] R. Hofstadter, H. R. Fechter, and J. A. McIntyre: Scattering of High-Energy Electrons and the Method of Nuclear Recoil. *Phys. Rev.* 91 (1953) 422,423

- [HM55] R. Hofstadter and R. W. McAllister: Electron Scattering from the Proton. *Phys. Rev.* 98 (1955) 217,218
- [HIM84] F. Halzen and A. Martin. *Quarks and Leptons* John Wiley and Sons, Inc. 1984
- [JB79] F. Jacquet and A. Blondel: Proceedings of the study of an  $ep$  facility for Europe. *DESY* 79/48 (1979) 381
- [Ken91] H. W. Kendall: Deep Inelastic Scattering: Experiments on the Proton and the Observation of Scaling. *Rev. Mod. Phys.* 63 (1991) 597 - 614. - Lecture delivered on the occasion of the presentation of the 1990 Nobel Prize in Physics
- [KLF77] É. A. Kuraev, L. N. Lipatov, and V. S. Fadin: The Pomernichuk Singularity in Nonabelian Gauge Theories. *Sov. Phys. JETP* 45 (1977) 199 - 204
- [KSM91] K. Kwiatkowski, H. Spiesberger, and H.-J. Möhring: HERACLES. An Event Generator for  $ep$  Interactions at HERA Including Radiative Processes. In W. Buchmüller and G. Ingelmann, editors, *Physics at HERA*. volume 3. 1294. Proceedings of the Workshop held at DESY, Hamburg. October 29 - 30, 1991
- [L95] H. L. Lai et al.: Global QCD Analysis and the CTEQ Parton Distributions. *Phys. Rev. D* 51 (1995) 4763 - 4782
- [Lon92] L. Lonnblad: ARIADNE Version 4: A Program for Simulation of QCD Cascades Implementing the Color Dipole Model. *Comput. Phys. Commun.* 71 (1992) 15 - 31
- [Lon95] L. Lonnblad: Rapidity Gaps and other Final State Properties in the Color Dipole Model for Deep Inelastic Scattering. *Z. Phys. C* 65 (1995) 285 - 292
- [M 72] G. Miller et al.: Inelastic Electron-Proton Scattering at Large Momentum Transfers and the Inelastic Structure Functions of the Proton. *Phys. Rev. D* 5 (1972) 528 - 544
- [Mar93] A. D. Martin: Structure Functions and Small  $x$  Physics. *Spanish Fund. Phys.* (1993) 250 - 292. - Lectures given at the XXI International Meeting on Fundamental Physics, Miafiores de la Sierra, Madrid, May 9 - 15, 1993
- [Mot29] N. F. Mott: The Scattering of Fast Electrons by Atomic Nuclei. *Proc. Roy. Soc.* 124 (1929) 425 - 442
- [MRS93] A. D. Martin, R. G. Roberts, and W. J. Stirling: Parton Distributions Updated. *Phys. Lett. B* 306 (1993) 145 - 150
- [MRS94] A. D. Martin, R. G. Roberts, and W. J. Stirling: Parton Distributions of the Proton. *Phys. Rev. D* 50 (1994) 6734 - 6752
- [MRS96] A. D. Martin, R. G. Roberts, and W. J. Stirling: Parton Distributions for low  $Q^2$ . *Phys. Rev. D* 51 (1996) 4756 - 4762
- [NMC92] NMC Collaboration (P. Amaudruz et al.): Proton and Deuteron  $F_2$  Structure Functions in Deep Inelastic Muon Scattering. *Phys. Lett. B* 295 (1992) 159 - 168

- [NV95] J. Ng and W Verkerke: An Overview of SRTD Analysis. Technical report. ZEUS 95-037. 1995
- [Ohr93] K. Ohrenberg: Entwicklung des Prototypen eines Echtzeit-Expertensystems zur Diagnose von Fehlern in der ZEUS-Datennahme. University of Hamburg, Diplomarbeit. July 1993
- [Per87] D. H. Perkins. *Introduction to High Energy Physics* Addison-Wesley Publishing Company, Inc. third edition. 1987
- [PZ95] K. Piotrkowski and M. Zachara: Determination of the ZEUS Luminosity in 1994. Technical report. ZEUS 95-138. 1995
- [Rep92] J. Repond: ELEC5. 1992. Algorithm to find the most likely scattered electron, ZEUS PHANTOM program library
- [Ros50] M. N. Rosenbluth: High Energy Elastic Scattering of Electrons on Protons. *Phys. Rev.* 79 (1950) 615 - 619
- [Rut11] E. Rutherford: The Scattering of  $\alpha$  and  $\beta$  Particles by Matter and the Structure of the Atom. *Phil. Mag.* 21 (1911) 669 - 688
- [S 95] W. Smith et al.: The ZEUS Calorimeter First Level Trigger. *Nucl. Inst. Meth.* A 355 (1995) 278 - 294
- [SB87] T. Sjostrand and M. Bengtsson: The Lund Monte Carlo for Jet Fragmentation and  $e^+e^-$  Physics: JETSET VERSION 6.3: An Update. *Comput. Phys. Commun.* 43 (1987) 367
- [Sch] S. Schlenstedt: EVTAK. Routine to reject events with bad ZEUS running conditions, ZEUS PHANTOM program library
- [Sch92] Thorsten Schlichting: Überwachung und Auswertung des Datenflusses im ZEUS Eventbuilder. University of Hamburg, Diplomarbeit. April 1992
- [Tay91] R. E. Taylor: Deep Inelastic Scattering: The Early Years. *Rev. Mod. Phys.* 63 (1991) 573 - 595. - Lecture delivered on the occasion of the presentation of the 1990 Nobel Prize in Physics
- [Wai93] L. Wai: ISLANDS. 1993. Algorithm to assign calorimeter cell to islands, ZEUS PHANTOM program library
- [Wii91] B. H. Wiik: HERA Status. In W. Buchmüller and G. Ingelmann, editors, *Physics at HERA*. volume 1. 1. Proceedings of the Workshop held at DESY, Hamburg. October 29 - 30, 1991
- [ZEU93a] ZEUS Collaboration: Hadronic Energy Distributions in Deep-Inelastic Electron-Proton Scattering. *Z. Phys.* C 59 (1993) 231 - 242
- [ZEU93b] ZEUS Collaboration: Measurement of the Proton Structure function  $F_2$  in  $ep$  Scattering at HERA. *Phys. Lett.* B 316 (1993) 412 - 426

- [ZEU93c] ZEUS Collaboration: Observation of Events with a Large Rapidity Gap in Deep Inelastic Scattering at HERA. *Phys. Lett.* B 315 (1993) 481 - 493
- [ZEU93d] ZEUS Collaboration: The ZEUS Detector, Status Report 1993. Technical report. DESY. February 1993
- [ZEU94] ZEUS Collaboration: Comparison of Energy Flows in Deep Inelastic Scattering Events with and without a Large Rapidity Gap. *Phys. Lett.* B 338 (1994) 483 - 496
- [ZEU95a] ZEUS Collaboration: Measurement of the Diffractive Structure Function in Deep Inelastic Scattering at HERA. *Z. Phys.* C 68 (1995) 569 - 584
- [ZEU95b] ZEUS Collaboration: Measurement of the Proton Structure Function  $F_2$  from the 1993 HERA Data. *Z. Phys.* C 65 (1995) 379 - 398
- [ZEU96a] ZEUS Collaboration: Measurement of the  $F_2$  Structure Function in Deep Inelastic Scattering Using 1994 Data from the ZEUS Detector at HERA. *DESY* 96-076 (1996). - accepted by *Zeitschrift f. Physik*
- [ZEU96b] ZEUS Collaboration: Measurement of the Proton Structure Function  $F_2$  at Low  $x$  and Low  $Q^2$  at HERA. *Z. Phys.* C 69 (1996) 607 - 620
- [Zwe64] G. Zweig: An  $SU_3$  Model for Strong Interaction Symmetry and its Breaking. *CERN* 8419/TH.412 (1964)